FREQUENCY STEERABLE ACOUSTIC TRANSDUCERS

A Thesis
Presented to
The Academic Faculty

by

Matteo Senesi

In Partial Fulfillment
of the Requirements for the Degree
Doctor of Philosophy in the
School of Aerospace Engineering

Georgia Institute of Technology
August 2012

FREQUENCY STEERABLE ACOUSTIC TRANSDUCERS

Approved by:

Professor Massimo Ruzzene, Advisor
School of Aerospace Engineering
Georgia Institute of Technology

Professor Krish Ahuja
School of Aerospace Engineering
Georgia Institute of Technology

Professor Levent Degertekin
School of Mechanical Engineering
Georgia Institute of Technology

Professor Tim Lieuwen
School of Aerospace Engineering
Georgia Institute of Technology

Professor Jennifer Michaels
School of Electrical and Computer Engineering
Georgia Institute of Technology

Date Approved: 19 June 2012

To my family

ACKNOWLEDGEMENTS

I would like to express my gratitude to my advisor, Dr. Massimo Ruzzene, for the trust in my capabilities and his sage and fair guidance.

I owe my parents, Marcella and Franco, my sister and her husband, Danila and Fulvio, and my all family, a debt of gratitude for their unceasing support and for letting me find my way even if it was far from them. A special thought to nonna Tina, who gave goodbye two years ago but her love is never gone.

Thanks to the great friends I have made in Atlanta: Raj for his lunch conversations, Andrea for his terrific humor, Buli for his sage-like wisdom and great brew, Luca for the campus walks breaks, Philipp for his unforgettable running partnership, Paolo for the socio–economical debates, Matteo for the high–level sport anecdotes and Trang for the talks precision.

Thanks to my labmates Maria and Filippo, and in particular Buli and Emanuele for their precious research inputs and contributions.

Finally, I am grateful to all the Thesis committee members Dr. Krish Ahuja, Dr. Levent Degertekin, Dr. Tim Lieuwen and Dr. Jennifer Michaels for their time and insightful suggestions which were invaluable for the completion of this thesis.

TABLE OF CONTENTS

LIST OF TABLES

LIST OF FIGURES

LIST OF SYMBOLS OR ABBREVIATIONS

AFC	Active Fiber Composite.
BW	Bandwidth.
DOA	Direction of Arrival.
EMAT	Electromagnetic Acoustic Transducer.
FE	Finite Element.
FFT	Fast Fourier Transform.
FSAT	Frequency Steerable Acoustic Transducer.
FT	Fourier Transform.
GW	Guided Wave.
IDT	Interdigitated Transducer.
MFC	Macro Fiber Composite.
NDE	Nondestructive Evaluation.
PCB	Printed Circuit Board.
PVDF	Polyvinylidene Fluoride.
PZT	Lead Zirconate Titanate.
RMS	Root Mean Square.
SAFE	Semi–Analytical Finite Element.
SAW	Surface Acoustic Wave.
SHM	Structural Health Monitoring.
SLDV	Scanning Laser Doppler Vibrometer.
STFT	Short Time Fourier Transform.
TOF	Time of Flight.
WFT	Warped Frequency Transform.
WS–FSAT	Wavenumber Spiral FSAT.

SUMMARY

Structural health monitoring (SHM) is an active research area devoted to the assessment of the structural integrity of critical components of aerospace, civil and mechanical systems. Guided wave methods have been proposed for SHM of plate-like structures using permanently attached piezoelectric transducers, which generate and sense waves to evaluate the presence of damage. Effective interrogation of structural health is often facilitated by sensors and actuators with the ability to perform electronic, i.e. phased array, scanning.

The objective of this research is to design an innovative directional piezoelectric transducer to be employed for the localization of broadband acoustic events, or for the generation of Lamb waves for active interrogation of structural health. The proposed Frequency Steerable Acoustic Transducers (FSATs) are characterized by a spatial arrangement of active material which leads to directional characteristics varying with frequency. Thus FSATs can be employed both for directional sensing and generation of guided waves without relying on phasing and control of a large number of channels. The analytical expression of the shape of the FSATs is obtained through a theoretical formulation for continuously distributed active material as part of a shaped piezoelectric device. The FSAT configurations analyzed in this work are a quadrilateral array and a geometry which corresponds to a spiral in the wavenumber domain. The quadrilateral array is experimentally validated, confirming the concept of frequency-dependent directionality. Its limited directivity is improved by the Wavenumber Spiral FSAT (WS–FSAT), which, instead, is characterized by a continuous frequency dependent directionality.

Preliminary validations of the WS–FSAT, using a laser doppler vibrometer, are

followed by the implementation of the WS–FSAT as a properly shaped piezo transducer. The prototype is first used for localization of acoustic broadband sources. Signal processing algorithms and related imaging techniques for damage location are also presented. Finally, the WS–FSAT has also been experimentally validated in generation.

CHAPTER I

INTRODUCTION

1.1 Overview

The research investigates the design of directional piezoelectric transducers for guided waves sensing and generation. The proposed devices find applications in the area of Structural Health Monitoring (SHM). The following section first gives a background on SHM, guided waves and piezoelectric transducers, focusing on the techniques for guided waves inspections. Then, the motivations for the present study are detailed. Research objectives and the contributions of this work to the existing knowledge on directional transducers are highlighted. Finally, the chapter concludes with the organization of the research.

1.2 Background

1.2.1 Structural Health Monitoring

In recent years, there has been an increasing awareness of the importance of damage detection systems in civil, mechanical and aerospace structures (Figure 1). It is foreseen that such systems in a structure would be able to provide information regarding the health of the structure, warn about any incipient damage, and provide an estimate of the remaining useful life of the structure. The potential benefits that would follow from such a technology are enormous. Maintenance procedures for structures with such systems could change from being schedule–driven to condition–based, thereby cutting down on the time for which structures are off–line and correspondingly resulting in huge cost savings. Most significantly, the confidence levels in operating structures would increase sharply as a result of the safeguards against unpredictable

Figure 1: Example of structures with embedded SHM systems.

structural system degradation, particularly so for ageing structures. Most importantly, the safety of the users is better ensured.

Structural health monitoring is a key component of damage prognosis systems. SHM is the component that examines the structure for damage and provides information about any damage that is detected. An SHM system typically consists of an onboard network of sensors for data acquisition and some central data processor. It may utilize stored knowledge of structural materials, operational parameters, and health criteria. The schemes available for SHM can be broadly classified as active or passive depending on whether or not they involve the use of actuators, respectively. Examples of passive schemes are acoustic emission and strain/load monitoring, which have been demonstrated with some success [64, 45, 22, 39, 12]. However, these suffer from the drawback of requiring high sensor densities on the structure. Unlike passive methods, active schemes are capable of exciting the structure in a prescribed manner, and have the potentials to examine it for damage when required.

1.2.2 Guided waves

Guided wave (GW) testing has emerged as a very prominent option among active schemes. GW also may be suitable for SHM applications, having an onboard, preferably built-in, sensor and actuator network to assess the state of a structure during operation. GWs are stress waves forced to follow a path defined by structural boundaries. For example, when a beam is excited at high frequency, stress waves travel in the beam along its axis away from the excitation source, i.e. the beam guides the waves along its axis. Similarly, in a plate, the two free surfaces of the plate guide the waves within its confines. There are several application areas for guided elastic waves in solids, such as seismology, inspection, material characterization, delay lines, etc., and consequently these have been a subject of much study [1, 6, 27].

A very important class among GWs is that of Lamb waves, which can propagate in a thin plate (or shell) with free surfaces. Because of the abundance of plate and shell-like structural configurations, and because of GW's ability to be transmitted over long distances over the surface as well as through the thickness of a structure with little attenuation, Lamb waves have been the subject of much scrutiny. Due to their relevance, the term "Lamb wave" and "guided wave" are often used interchangeably in the literature.

Lamb waves are dispersive (the propagation velocities are dependent on frequency) and propagate according to several modes which are either symmetric or anti–symmetric with respect to mid thickness. Different GW modes present sensitivity to a variety of structural defects. For instance, the fundamental symmetric (S_0) Lamb mode is sensitive to through-the-thickness damage due to its dominant in-plane components. Therefore is well suited for the detection of, for example, full- or part-depth holes. Similarly, the A_0 mode is better suited for surface damage (e.g., surface cracks) due to

its dominant out-of-plane component. The potential damage types that a Lamb wave-based inspection can provide are summarized by Rose [71]. In general, a Lamb wave-based damage detection approach features (1) the ability to inspect large structures while retaining coating and insulation, e.g. a pipe system under water; (2) the ability to inspect the entire cross sectional area of a structure (100% coverage over a fairly long length); (3) the lack of need for complicated and expensive insertion/rotation devices, and for device motion during inspection; (4) excellent sensitivity to multiple defects with high precision of identification; and (5) low energy consumption and great cost-effectiveness. At a sophisticated level, a Lamb wave-based identification should hierarchically perform, with increasing levels of difficulty, (1) qualitative indication of the occurrence of damage; (2) quantitative assessment of the position of damage; (3) quantitative estimation of the severity of damage; and (4) prediction of structural safety, e.g. residual service life [87].

1.2.3 Schemes of operation

In GW SHM, an actuator generating GWs is excited by a prescribed signal (typically a modulated sinusoidal tone burst of some limited number of cycles, and central frequency). In general, when a GW field is incident on a structural discontinuity (which has a size comparable to the GW wavelength), it scatters GWs in all directions. The structural discontinuity could be damage in the structure, such as a crack or delamination, a structural feature (such as a stiffener or a structural boundary). Therefore, to be able to distinguish between damage and structural features, prior information may be required about the structure in its undamaged state. This is typically in the form of a baseline signal obtained for the "healthy state" to use as reference for comparison with the test case. There are two approaches commonly used in GW SHM: pulse–echo and pitch–catch. In the former, after exciting the structure with a narrow bandwidth pulse, a sensor collocated with the actuator is

used to "listen" for echoes of the pulse coming from discontinuities. Because the boundaries and the wave speed for a given center actuation frequency of the tone burst are known, the signals from the boundaries can be filtered out (or alternatively the test signal can be subtracted from the baseline signal). Then, signals from the defects are left (if present). From these signals, defects can be located using the wavespeed. In the pitch-catch approach, a pulse signal is sent across the specimen under interrogation and a sensor at the other end of the specimen receives the signal. From various characteristics of the received signal, such as delay in time of transit, amplitude, frequency content, etc., information about the damage can be obtained.

In either approach, damage-sensitive features are extracted from the signal using some signal-processing algorithm, and then a pattern recognition technique is required to classify the damage and estimate its severity (Figure 2).

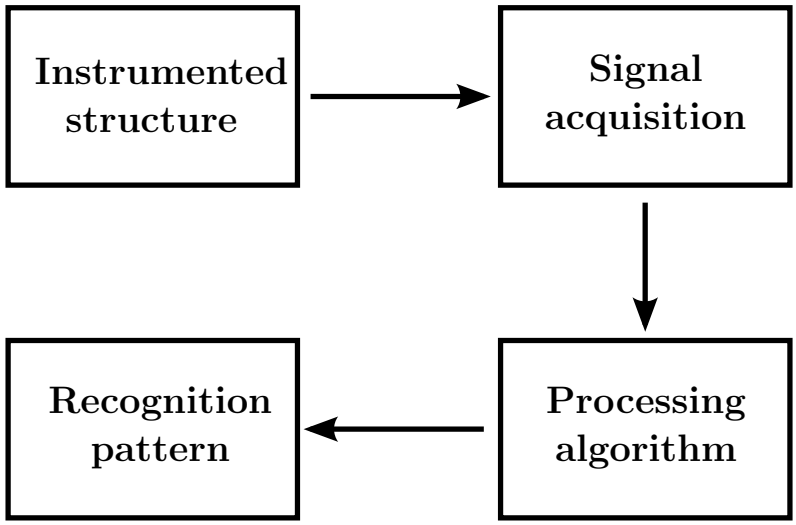

Figure 2: GW SHM steps.

The actuator-sensor pair in GW testing can have a large coverage area, resulting in fewer units distributed over the structure. For this reason, damage detection through guided wave in plate-like structures has attracted the attention of a large number of researchers in recent years [4, 5, 69, 16, 15, 48, 51, 29].

1.2.4 Piezoelectric transducers

The critical elements of GW SHM are the transducers, the arrangement of the transducer network to scan the structure, and the overall SHM architecture (i.e. issues related to supporting electronics, robustness and packaging). The most commonly used transducers for NDE are angled piezoelectric wedge transducers [92, 82], comb transducers [59] and electromagnetic acoustic transducers (EMATs) [3]. Other options that have been explored in recent years for NDE are Hertzian contact transducers [18] and lasers [60]. However, while these types of transducers function well for maintenance checks when the structure is offline for service, they are not compact enough to be permanently onboard the structure during its operation. This is particularly true in aerospace structures, where mass and space penalties associated with the additional transducers on the structure should be minimal.

The most commonly used transducers for SHM are embedded or surface-bonded piezoelectric wafer transducers (hereafter referred to as piezos). Piezos are inexpensive, and are available in very fine thicknesses (0.1 mm for ceramics and 9 μm for polymer film), making them very unobtrusive and conducive for integration into structures. Piezos operate on the piezoelectric and inverse piezoelectric principles that couple the electrical and mechanical behavior of the material. An electric charge is collected on the surface of the piezoelectric material when it is strained. The converse effect also occurs, that is, the generation of mechanical strain in response to an applied electric field. Hence, they can be used both as actuators and sensors. The most commonly available materials are lead zirconium titanate ceramics (known as PZT) [75, 36] and polyvinylidene fluoride (PVDF), which is a polymer film. Both of these are usually poled through the thickness, which is also the direction in which the voltage is applied or sensed. When used as an actuator, the high-frequency voltage signal causes waves to be excited in the structure. In the sensor configuration, the strain over the sensor area causes a voltage signal across the piezo. Piezoceramics

are quite brittle and need to be handled with care. In contrast, polymer films are very flexible and easy to handle. Monkhouse et al. in [52, 53] designed PVDF films with copper backing layers to improve its response characteristics. An interdigitated electrode pattern was deposited using printed circuit board (PCB) techniques for modal selectivity, and the transducers were able to detect simulated defects. However, because of their weaker inverse piezoelectric properties and high compliance, the performance of PVDF based transducers as actuators and sensors is poorer. In addition, PVDF films cannot be embedded into composite structures because of the loss of piezoelectric properties under typical composite curing conditions. Therefore, PZT is the more popular choice for the transducer material among GW SHM researchers (for example, [35, 57, 34]).

1.2.5 Directional transducers

GW SHM approaches potentially benefit from the use of transducers with controllable directional characteristics, so that scanning of a surface can be performed to locate damage, impacts or cracks.

Wave steering through phased arrays [76] is a well-established technique, widely used in radar, sonar, seismology, oceanology, and medical imaging such us echocardiography and ultrasonography [79]. A phased array consists of a group of sensors located at distinct spatial locations in which the relative phases of the sensor signals are varied in such a way that the effective propagation pattern of the resulting signal is reinforced in a desired direction and suppressed in undesired directions. The phased array principles have allowed the development of radar and sonar systems that can scan the horizon electronically without actually doing any mechanical motion.

Phased array concepts are adopted extensively also in ultrasonic imaging for NDE applications [38, 47], because of its multiple advantages [41, 68, 2], such as high inspection speed, flexible data processing capability, improved resolution, and the

capability of scanning without requiring mechanical movement, i.e., dynamic beam steering and focusing [86]. Rose *et al.* in [70] describe a high-frequency guided-wave phased-array focusing method for performing nondestructive pipe inspection with conventional phased-array transducers. Deutsch *et al.* in [20] demonstrated a phased array for the Lamb wave inspection of thin plates utilizing wedge-coupled conventional ultrasonic transducers and elaborated electronics. Fromme *et al.* in [23] designed and built a permanently attached guided ultrasonic wave array prototype to be used in the long-term monitoring of structural integrity.

However, one of the major limitations in the path of transitioning Lamb-wave NDE techniques into SHM methodologies has been the size and cost of the conventional NDE transducers, which are rather bulky and expensive. The permanent installation of conventional NDE transducers onto a structure is not feasible, especially when weight and cost are at a premium such as in the aerospace applications. Guided wave-based phased arrays for SHM have been pursued for example by [44], where a phased comb transducer is proposed for the inspection of pipes, and in [25] where a virtual beam steering concept uses permanently attached piezoelectric PZT transducer arrays. A circular array integrated with a deconvolution algorithm for better imaging quality is presented in [80], while [90, 91] illustrate the study of linear and two-dimensional (2D) square arrays capable of virtual beam steering in a 360° range. Other researchers have investigated the use of spatially sparse arrays, consisting of various sensors distributed over a large area, as an effective approach to image damage inside and outside the area enclosed by the arrays [77, 32, 49, 50].

Passive sensing of acoustic events often relies on the triangulation of time-of-flight information provided by multiple sensors. Time-of-flight triangulation of guided waves is however complicated by the dispersive and multi-modal nature of wave propagation, which makes the estimation of arrival times challenging. To overcome such difficulties, rosette configurations have been proposed which exploit the inherent directional

nature of macro fiber composite (MFC) transducers [42]. Another interesting application of MFCs for array design is presented in [72], where guided wave steering relies on the actuation in sequence of multiple sections of wedge-shaped transducers arranged in a circular ring pattern.

Patterning of the sensing material lay-out and of the electrodes provides significant opportunities to provide transducers with inherent frequency and directional sensitivity. This basic idea has been widely exploited for the design of interdigitated transducers (IDTs) used as part of surface acoustic wave (SAW) devices [31]. While linear IDT configurations are commonly employed for selective generation and detection of surface waves, other alternative configurations, such as the slanted IDT described for example in [88], and the annular IDTs proposed in [43], have been proposed to achieve novel functionalities such as wide-band operation and acoustic wave focusing. Wilcox [81] proposed the idea of a circular array of six PVDF curved finger IDTs, so that each element would generate a divergent beam, which enables the inspection of a pie-slice shaped area of the plate. Thus, the six IDTs together would have a 360 field of vision about themselves.

An ultrasonic radiator with frequency beam steering capabilities is presented in [40]. The radiator consists of a cantilever plate, placed in water, on which a pair of piezoelectric ceramics are mounted. Direction of propagation of ultrasound in water is solely steered by frequency of the applied signal. Meander antenna whose main lobe is steerable by variation of the feed frequency is studied in [13, 73] for radar applications.

1.3 Motivations

The GW based damage detection techniques using structurally integrated transducers for SHM is still in its formative years. All the promising results mentioned above not only demonstrate the potential benefits of beam steering for guided waves generation

and sensing, but also underline some limitations. One of such limitations consists in the array basic principle of operation, i.e., the delay-and-sum algorithm [26], which requires wiring and multiplexing of individual array elements. In fact, most ultrasonic phased array technologies require electronic beam steering devices and corresponding hardware complexity, which makes their implementation as embedded devices problematic [47, 91]. Limitations on current approaches and the needing of novel devices to effectively asses the challenges of SHM through guided wave inspections are the motivations of the present research.

1.4 Objectives

Given the motivations above, the objectives of the thesis are:

- To study the equations that govern sensing and actuation of guided waves (Lamb waves) through surface mounted piezoelectric sensors and to formulate a strategy for the design of sensors and actuators with inherent directional and beam steering properties.

- To develop a novel class of Frequency Steerable Acoustic Transducers (FSATs) for directional generation/sensing of guided waves. Proposed FSAT transducers direct energy in specified directions without the need for individual element control. The FSATs are characterized by a spatial arrangement of the piezoelectric material which leads to frequency-dependent directionality. The resulting FSATs can be employed both for directional sensing and generation of guided waves, without relying on phasing and control of a large number of channels.

- To validate the concept of frequency-dependent directionality both numerically and experimentally, through FSATs prototyping and testing.

To accomplish these objectives, the work first employs numerical methods to confirm the directional properties of the proposed FSATs. Next, prototyping of the

FSATs allows an experimental analysis that validates the analytical and numerical predictions.

1.5 Contributions

The accomplishment of the objectives mentioned above allow the achievement of the following contributions:

1. the definition of geometric directivity for piezoelectric transducers, valid for both guided waves sensing and actuation, which is the fundament of the illustrated frequency beam steering concept;

2. the experimental validation of the FSATs directional capabilities in both sensing and actuation;

3. the Wavenumber Spiral FSAT (WS–FSAT) geometry, characterized by an excellent directionality, allowing location detection of acoustic broadband sources;

4. the implementation of a working imaging technique to enrich further the capabilities of the WS–FSAT, providing a graphical and an immediate visualization of the acoustic event.

1.6 Organization of the work

The work is organized in 7 chapters including this introduction. Chapter 2 presents the theoretical developments in support of the evaluation of the directional properties of arbitrarily shaped piezoelectric transducers. Chapter 3 is devoted to the analysis of a quadrilateral periodic array FSAT with numerical and experimental validation. This transducer configuration is given as an introductive example and confirms the concept of frequency-dependent directionality. Chapter 4 describes a WS–FSAT with a numerical and a preliminary experimental validation. Chapter 5 illustrates PVDF

prototyping and testing of the WS–FSAT in sensing, providing the conclusive validation of the device. The development and the application of an imaging technique to enhance the capabilities of the WS–FSAT is also presented. Chapter 6 considers a preliminary WS–FSAT experimental testing in actuation and discusses an alternative fabrication design adopting MFC substrate. Finally Chapter 7 outlines some conclusions, the contributions brought by the research and future work.

CHAPTER II

SHAPING OF PIEZO PATCHES FOR DIRECTIONAL SENSING AND GENERATION OF LAMB WAVES

2.1 Overview

The chapter provides the theoretical background to sensing and actuation by piezo patches of arbitrary shapes. An expression of frequency directivity valid for both cases is outlined. Eventually, a set of simple transducers geometries is provided as a starting point for frequency directivity analysis and implementation.

2.2 Sensing

This section presents the equations that govern sensing of Lamb waves through surface mounted sensors. The case of a piezoelectric patch of arbitrary shape is illustrated as a general framework for the subsequent illustration of the principles of directional sensing through proper sensor shaping.

2.2.1 Plate configuration and piezoelectric constitutive relations

The system under consideration is illustrated in Fig. 3. The domain of interest consists of a mechanical structure (thin plate) on an open domain Ω and of a piezoelectric domain Ω_p of thickness t_P. The reference system used for the analysis is located at the mid-surface of the structure, with coordinates x_1, x_2 defining the plane of the structure. The constitutive equations for the piezoelectric domain are expressed as:

$$\begin{aligned} \boldsymbol{\sigma} &= \boldsymbol{C}^E \boldsymbol{\varepsilon} - \boldsymbol{e}^T \boldsymbol{E} \\ \boldsymbol{D} &= \boldsymbol{e}\,\boldsymbol{\varepsilon} + \boldsymbol{\epsilon}^{\varepsilon} \boldsymbol{E} \end{aligned} \tag{1}$$

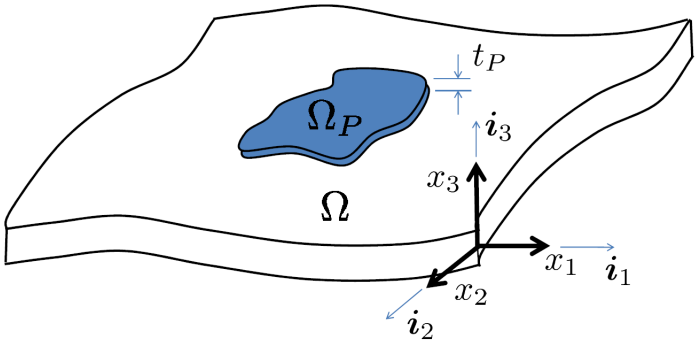

Figure 3: Plate with arbitrarily shaped piezoelectric sensor bonded on the top surface, and considered coordinate system.

where $\boldsymbol{\sigma} = \{ \ \sigma_{11} \quad \sigma_{22} \quad \sigma_{33} \quad \tau_{13} \quad \tau_{23} \quad \tau_{12} \ \}^T$ and $\boldsymbol{\varepsilon} = \{ \ \varepsilon_{11} \quad \varepsilon_{22} \quad \varepsilon_{33} \quad \gamma_{13} \quad \gamma_{23} \quad \gamma_{12} \ \}^T$ respectively are the mechanical stress and strain vectors, $\boldsymbol{D} = \{ \ D_1 \quad D_2 \quad D_3 \ \}^T$ is the electric charge vector, and $\boldsymbol{E} = \{ \ E_1 \quad E_2 \quad E_3 \ \}^T$ is the electric field vector. Also, $\boldsymbol{C}^E$ is the stiffness matrix of the material at constant electric field, $\boldsymbol{e}$ is the piezoelectric coupling matrix evaluated at constant stress, while $\boldsymbol{\epsilon}^\varepsilon$ denotes the permittivity matrix at constant strain. Equation (1) holds over the domain of the structure covered by the piezoelectric patch, defined by $\boldsymbol{x} \in \Omega_P$, where $\boldsymbol{x} = x_1\boldsymbol{i}_1 + x_2\boldsymbol{i}_2$ denotes a position vector on the plane of the structure. The piezoelectric patch is assumed to be decoupled from the underlying mechanical structure [46], i.e. it does not interfere with the dynamics of the elastic medium.

It is convenient to extend the validity of the piezoelectric constitutive relations to the entire domain Ω by introducing a functional $\phi(\boldsymbol{x})$ defined as:

$$\phi(\boldsymbol{x}) = \begin{cases} 1, & \boldsymbol{x} \in \Omega_P \\ 0, & \boldsymbol{x} \in \Omega - \Omega_P \end{cases} \tag{2}$$

which describes the shape of the patch. A second functional $\psi(\boldsymbol{x})$ is introduced to allow for different polarizations to be present within the piezoelectric domain. For simplicity, and in light of practicality, the case of alternating polarizations over specified sub-regions of Ω_P is considered, so that $\psi(\boldsymbol{x}) = \pm 1$, $\boldsymbol{x} \in \Omega_P$. Accordingly,

Eq. (1) can be rewritten as:

$$\left\{ \begin{array}{c} \boldsymbol{\sigma} \\ \boldsymbol{D} \end{array} \right\} = \phi(\boldsymbol{x}) \left[\begin{array}{cc} \boldsymbol{C}^E & -\psi(\boldsymbol{x})\boldsymbol{e}^T \\ \psi(\boldsymbol{x})\boldsymbol{e} & \boldsymbol{\epsilon}^\varepsilon \end{array} \right] \left\{ \begin{array}{c} \boldsymbol{\varepsilon} \\ \boldsymbol{E} \end{array} \right\}, \boldsymbol{x} \in \Omega \tag{3}$$

For sensing, the second of Eq.s (3) is of particular importance and will be analyzed in detail. The following assumptions are introduced to simplify the analysis. First, the piezoelectric material is considered as polarized across its thickness direction x_3, so that two of the components of the electric displacement vector are zero ($D_1 = D_2 = 0$). Then, the sensor is assumed in a state of plane stress, i.e. $\sigma_{33} \approx \sigma_{13} \approx \sigma_{23} \approx 0$, and the strain component in the sensor result to be $\boldsymbol{\varepsilon} = \{ \ \varepsilon_{11} \quad \varepsilon_{22} \quad \gamma_{12} \ \}^T$. The second of Eq.s (3) therefore reduces to:

$$D_3 = \phi(\boldsymbol{x})\boldsymbol{b}^T\boldsymbol{D} = \phi(\boldsymbol{x})\boldsymbol{b}^T(\psi(\boldsymbol{x})\boldsymbol{e}\boldsymbol{\varepsilon} + \boldsymbol{\epsilon}^\varepsilon\boldsymbol{E}), \boldsymbol{x} \in \Omega \tag{4}$$

where $\boldsymbol{b} = [0, \ 0, \ 1]^T$. Considering the strain-charge form of the piezoelectric constitutive equations, Eq. (4) can be rewritten as follows:

$$D_3 = \phi(\boldsymbol{x})\boldsymbol{b}^T[\psi(\boldsymbol{x})\boldsymbol{d}^\sigma\boldsymbol{C}^E\boldsymbol{\varepsilon} + (\boldsymbol{\epsilon}^\sigma - \boldsymbol{d}^\sigma\boldsymbol{C}^E\boldsymbol{d}^{\sigma^T})\boldsymbol{E}], \quad \boldsymbol{x} \in \Omega \tag{5}$$

where $\boldsymbol{d}^\sigma, \boldsymbol{\epsilon}^\sigma$ respectively denote the matrix of the piezoelectric strain constants and of the permittivity constants evaluated at constant stress.

2.2.2 Voltage generated by the patch

In sensing mode, the total charge developed over the piezoelectric area is $\int_{\Omega_P} D_3 d\boldsymbol{x} = \int_\Omega \phi(\boldsymbol{x}) D_3 d\boldsymbol{x} \approx 0$. Integration of both sides of Eq. (5) therefore gives:

$$\boldsymbol{b}^T\boldsymbol{d}^\sigma\boldsymbol{C}^E \int_\Omega \boldsymbol{\varepsilon}\phi(\boldsymbol{x})\psi(\boldsymbol{x})d\boldsymbol{x} = \boldsymbol{b}^T(\boldsymbol{d}^\sigma\boldsymbol{C}^E\boldsymbol{d}^{\sigma^T} - \boldsymbol{\epsilon}^\sigma) \int_\Omega \phi(\boldsymbol{x})\boldsymbol{E}d\boldsymbol{x} \tag{6}$$

where it is assumed that all properties of the patch are constant over the area Ω_P. Equation (6) can be simplified by imposing that $E_1 = E_2 = 0$, and that the voltage

varies linearly across the thickness of the piezo t_P, i.e. $E_3 = \frac{V}{t_P}$, with V denoting the voltage measured at the electrodes. Accordingly, the electric field in Eq. (6) can be expressed as:

$$\boldsymbol{E} = \frac{V}{t_P}\boldsymbol{b} \tag{7}$$

Substituting in Eq. (6), and solving for the measured voltage V gives:

$$V = \frac{t_P}{A_P[\boldsymbol{b}^T(\boldsymbol{d}^\sigma \boldsymbol{C}^E \boldsymbol{d}^{\sigma^T} - \boldsymbol{\epsilon}^\sigma)\boldsymbol{b}]}\boldsymbol{b}^T\boldsymbol{d}^\sigma\boldsymbol{C}^E\int_\Omega \boldsymbol{\varepsilon} f(\boldsymbol{x})d\boldsymbol{x} \tag{8}$$

where $A_P = \int_\Omega \phi(\boldsymbol{x})d\boldsymbol{x}$ is the area occupied by the piezoelectric patch, and where $f(\boldsymbol{x}) = \phi(\boldsymbol{x})\psi(\boldsymbol{x})$ is introduced to simplify the notation.

2.2.3 Material and shape related directivities

The sensing voltage expressed in Eq. (8) can be evaluated in the presence of a plane wave propagating in the plane of the structure at frequency ω. The surface displacement can in general be expressed as:

$$\boldsymbol{u}(\boldsymbol{x},\omega) = \boldsymbol{U}_0(\omega)e^{-j\boldsymbol{k}_0(\omega)\cdot\boldsymbol{x}} \tag{9}$$

where $\boldsymbol{U}_0$ defines the amplitude and the polarization of the wave at the considered frequency, and $\boldsymbol{k}_0(\omega) = k_0(\omega)\boldsymbol{i}'_1 = k_0(\omega)(\cos\theta\boldsymbol{i}_1 + \sin\theta\boldsymbol{i}_2)$ is the considered wave vector defining plane wave propagation at an angle θ (Fig. 4). Assuming that the considered wave is characterized by a displacement field such that:

$$\boldsymbol{u}(\boldsymbol{x},\omega)\cdot\boldsymbol{i}'_2 = 0 \tag{10}$$

the only strain component relevant to the surface mounted sensor is given by:

$$\varepsilon_{1'1'} = \frac{\partial u'_1}{\partial x'_1} = jU_{1'_0}(\omega)k_0(\omega)e^{-jk_0(\omega)x'_1} \tag{11}$$

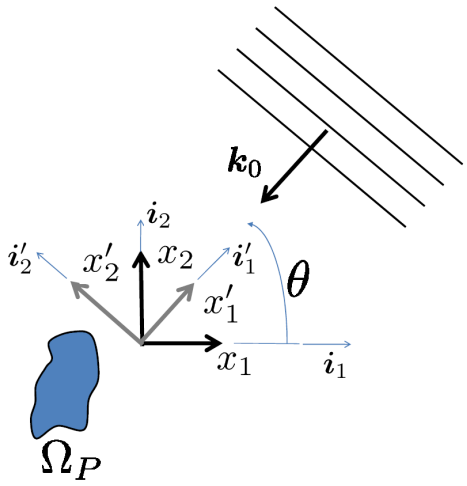

Figure 4: Schematic of plane wave propagating at angle θ on the plane of the structure $\boldsymbol{x}$.

while $\varepsilon_{2'2'} = \gamma_{1'2'} = 0$ [46]. In this case, the plane strain field in Eq. (8) can be written as:

$$\boldsymbol{\varepsilon} = \varepsilon_{1'1'}\boldsymbol{r}(\theta) \tag{12}$$

where $\boldsymbol{r}(\theta) = [\ \cos(\theta)^2,\ \ \sin(\theta)^2,\ \ 0\ ]^T$. Substituting Eq. (12) into Eq. (8) gives:

$$V(\omega) = jU_{1_0'}(\omega)k_0(\omega)\mathcal{H}(\theta)\mathcal{D}(\omega,\theta) \tag{13}$$

where:

$$\mathcal{H}(\theta) = \frac{t_P}{A_P}\frac{\boldsymbol{b}^T\boldsymbol{d}^\sigma\boldsymbol{C}^E\boldsymbol{r}(\theta)}{[\boldsymbol{b}^T(\boldsymbol{d}^\sigma\boldsymbol{C}^E\boldsymbol{d}^{\sigma^T} - \boldsymbol{\epsilon}^\sigma)\boldsymbol{b}]} \tag{14}$$

and

$$\mathcal{D}(\omega,\theta) = \int_\Omega e^{-jk_0(\omega)(x_1\cos\theta + x_2\sin\theta)}f(\boldsymbol{x})d\boldsymbol{x} \tag{15}$$

define two separate contributions to the measured voltage. The first quantity $\mathcal{H}$ contains the material properties of the piezo-structure system, and leads to a directional

component in case of non-isotropic properties of the patch [46, 37]. For the case of a monolithic PZT 5H patch for example, whose properties are listed in Table 1, the quantity $\mathcal{H}$ is constant with respect to the angle of wave propagation θ, and therefore no directionality is introduced. In contrast, the parameter $\mathcal{D}$ describes the effect of the distribution of material as defined by the function $f(\boldsymbol{x})$. Specifically, the definition of $\mathcal{D}$ provides the opportunity to select specific material and polarization distributions to tune the sensor to specific wavelengths and associated wave modes, and to achieve desired directionality properties. $\mathcal{D}$ can be seen as the directivity of the transducer characterized by the piezoelectric distribution $f(\boldsymbol{x})$.

Table 1: PZT 5H Piezoelectric material characteristics

$c_{11}^E = 1.2710^{11}$ Pa	$c_{22}^E = 1.2710^{11}$ Pa	$c_{33}^E = 1.1710^{11}$ Pa
$c_{12}^E = 8.0210^{10}$ Pa	$c_{13}^E = 8.4610^{10}$ Pa	$c_{23}^E = 8.4610^{10}$ Pa
$c_{44}^E = 2.3010^{10}$ Pa	$c_{55}^E = 2.3010^{10}$ Pa	$c_{66}^E = 2.3410^{10}$ Pa
$\epsilon_0 = 8854 \times 10^{-12}$ F/m	$d_{15} = 741 \times 10^{-12}$ C/N	$d_{24} = 741 \times 10^{-12}$ C/N
$d_{31} = -274 \times 10^{-12}$ C/N	$d_{32} = -274 \times 10^{-12}$ C/N	$d_{33} = 593 \times 10^{-12}$ C/N
$\varepsilon_{11}^\sigma = 3130\epsilon_0$	$\varepsilon_{22}^\sigma = 3130\epsilon_0$	$\varepsilon_{33}^\sigma = 3400\epsilon_0$

Of interest, is the further development of Eq. (15), which can be rewritten as follows:

$$\mathcal{D}(\omega, \theta) = \int_{-\infty}^{+\infty} e^{-j\boldsymbol{k}_0(\omega)\cdot\boldsymbol{x}} f(\boldsymbol{x}) d\boldsymbol{x} \tag{16}$$

which exploits the limited support of the function $f(\boldsymbol{x})$ so that the integration limits can be extended to infinity without affecting the value of the integral. Equation (16) can be easily recognized as the spatial Fourier Transform (FT) of the function $f(\boldsymbol{x})$. Its frequency dependence is based on the dispersion relation $\boldsymbol{k}_0 = \boldsymbol{k}_0(\omega)$, where $\boldsymbol{k}_0(\omega) = k_0(\omega)(\cos\theta \boldsymbol{i}_1 + \sin\theta \boldsymbol{i}_2)$. Equation 16 allows the convenient estimation of the directivity patterns associated with various sensor shapes and polarizations through the estimation of the FT pairs:

$$\mathcal{D}(\boldsymbol{k}_0(\omega), \theta) = \mathcal{F}[f(\boldsymbol{x})] \tag{17}$$

where $\mathcal{F}[\cdot]$ denotes the FT. Specifically, Eq. (17) suggests the possibility of evaluating the sensor directivity through FFT algorithms in the case of complex material distributions. At the same time, given a desired directivity, it is possible to obtain the correspondent sensor geometry by inverting Eq. (17), i.e.:

$$f(\boldsymbol{x}) = \mathcal{F}^{-1}[\mathcal{D}(\boldsymbol{k}_0(\omega), \theta)] \tag{18}$$

where $\mathcal{F}^{-1}[\cdot]$ denotes the inverse FT.

2.3 Generation

In the following, a general approach to obtain the directivity for an arbitrary shaped transducer in actuation mode is presented. Similarly to the system described in Section 2.2.1, consider the piezoelectric domain Ω_P placed on the free surface of an elastic space (thin plate) shown in Fig. 5. The piezoelectric patch is assumed to provide external inputs to the elastic medium without interfering with its dynamic behavior [63]. Collet *et al.* in [14] considered the fully coupled actuator/substrate system, providing a coupled FE–analytical solution. They noticed a slight frequency shift in the tuning curves, which is, however, mitigated at high frequencies.

Each infinitesimal element, $d\Omega = dx_1 dx_2$ of Ω_P is considered as a point source, which generates a harmonic signal in the time domain, $g(t) = g_0(\omega)e^{-j\omega t}$, where g_0 has the dimension of unit per area and it is directly related to the voltage applied to the piezo patch.

The elastic space is assumed homogeneous, isotropic and to sustain the propagation of a wave of phase speed $c(\omega)$. Dependence of c to ω is due to the dispersive properties of the medium. The analysis considers far-field radiation, so that each piezoelectric element generates a wave which can be considered as plane at the point

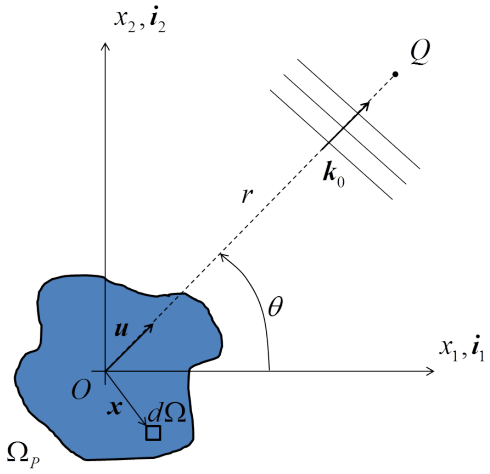

Figure 5: Plate with arbitrarily shaped piezoelectric actuator bonded on the top surface, and considered coordinate system.

of interest.

The infinitesimal response at point Q, with position vector $\boldsymbol{r} = r\boldsymbol{u}$, due to an harmonic excitation of an hypothetical element $d\Omega$ placed in the origin O, with position vector $\boldsymbol{x}_O$, can be expressed, dropping the harmonic term $e^{-j\omega t}$, as:

$$dw(\boldsymbol{r}, \boldsymbol{x}_O, \omega) = g_0(\omega)\mathcal{G}(\boldsymbol{r}, \boldsymbol{x}_O, \omega)d\Omega \tag{19}$$

where $\mathcal{G}(\boldsymbol{r}, \boldsymbol{x}_O, \omega)$ is an appropriate Green's function [27] defining the response in Q to a unit point source placed in O and, in its simpler version, can be expressed by the contribution of a geometric loss factor and of a phase shift due to the wave traveled distance:

$$\mathcal{G}(\boldsymbol{r}, \boldsymbol{x}_O, \omega) = \frac{1}{\sqrt{|\boldsymbol{r} - \boldsymbol{x}_0|}} e^{j\omega\tau_O} \tag{20}$$

with τ_O denoting the propagation time from the source at O to Q. Under the assumption that a single mode is propagating dispersively at speed $c(\omega)$, the propagation time can be expressed as:

$$\tau_0 = \frac{r}{c(\omega)} \tag{21}$$

The infinitesimal response at Q due to the generic source $d\Omega$, placed at $\boldsymbol{x}$, can be written as:

$$dw(\boldsymbol{r}, \boldsymbol{x}, \omega) = g_0(\omega) f(\boldsymbol{x}) \mathcal{G}(\boldsymbol{r}, \boldsymbol{x}, \omega) d\Omega \tag{22}$$

where $f(\boldsymbol{x})$ defines the distribution of active material as introduced in Section 2.2.2, and, similarly as in Eq. (20), $\mathcal{G}(\boldsymbol{r}, \boldsymbol{x}, \omega)$ is expressed as:

$$\mathcal{G}(\boldsymbol{r}, \boldsymbol{x}, \omega) = \frac{1}{\sqrt{|\boldsymbol{r} - \boldsymbol{x}|}} e^{j\omega\tau_{\boldsymbol{x}}} \tag{23}$$

with $\tau_{\boldsymbol{x}}$ the corresponding propagation time.

Within the far field assumption, $\tau_{\boldsymbol{x}}$ can be expressed in terms of τ_O through a set of simple geometric considerations, which are based on the schematic configuration shown in Fig. 6. The far field assumptions assume that the waves generated by an actuator in O and another one in a generic $\boldsymbol{x}$ position have essentially parallel wavefronts, and that the propagation distance only differs by a quantity which is related to the spacing between the two actuators. Hence the relation between $\tau_{\boldsymbol{x}}$ and τ_O can be approximated as:

$$\tau_{\boldsymbol{x}} \approx \frac{r - \boldsymbol{u} \cdot \boldsymbol{x}}{c(\omega)} \approx \tau_O - \frac{\boldsymbol{u} \cdot \boldsymbol{x}}{c(\omega)} \tag{24}$$

where $\boldsymbol{u} = \boldsymbol{u}(\theta) = [\ \cos(\theta),\ \ \sin(\theta)\ ]^T$ is the direction cosines of vector $\boldsymbol{r}$, and $\boldsymbol{x}$ is the position of the generic piezoelectric element (see Fig. 6). Still under the far field assumption, $\frac{1}{\sqrt{|\boldsymbol{r}-\boldsymbol{x}|}} \approx \frac{1}{\sqrt{|\boldsymbol{r}-\boldsymbol{x}_0|}}$, and, therefore, $\mathcal{G}(\boldsymbol{r}, \boldsymbol{x}, \omega)$ can be approximated as:

$$\mathcal{G}(\boldsymbol{r}, \boldsymbol{x}, \omega) \approx \mathcal{G}(\boldsymbol{r}, \boldsymbol{x}_0, \omega) e^{-j\frac{\omega}{c(\omega)}\boldsymbol{u}\cdot\boldsymbol{x}} \tag{25}$$

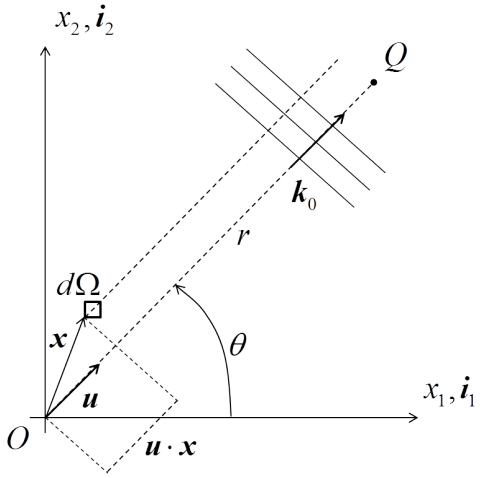

Figure 6: Far field approximation.

Based on the derivations and simplifying assumptions described above, the response due to the entire piezo-patch can be easily expressed as the superposition of the contributions from the various elements. This gives:

$$\begin{aligned} w(\boldsymbol{r},\omega) &= \int dw(\boldsymbol{r},\boldsymbol{x},\omega) \\ &= \int_{\Omega_P} g_0(\omega) f(\boldsymbol{x}) \mathcal{G}(\boldsymbol{r},\boldsymbol{x}_O,\omega) e^{-j\frac{\omega}{c(\omega)}\boldsymbol{u}\cdot\boldsymbol{x}} d\Omega \\ &= g_0(\omega)\mathcal{G}(\boldsymbol{r},\boldsymbol{x}_O,\omega)\mathcal{D}(\omega,\theta) \end{aligned} \tag{26}$$

where

$$\mathcal{D}(\omega,\theta) = \int_{\Omega_P} f(\boldsymbol{x}) e^{-j\frac{\omega}{c(\omega)}\boldsymbol{u}\cdot\boldsymbol{x}} d\Omega \tag{27}$$

contains the directionality contribution due to the distribution of the piezoelectric material. Considering that $\boldsymbol{k}_0(\omega) = \frac{\omega}{c(\omega)}\boldsymbol{u}$ by definition of the dispersion relation and exploiting the limited support of $f(\boldsymbol{x})$, Eq. (27) can be re-written as:

$$\mathcal{D}(\omega,\theta) = \int_{-\infty}^{+\infty} f(\boldsymbol{x}) e^{-j\boldsymbol{k}_0(\omega)\cdot\boldsymbol{x}} d\Omega \tag{28}$$

Equation (28) can be recognized as the spatial FT of the function $f(\boldsymbol{x})$, obtaining the same result found for the transducer directivity in sensing mode in Eq. (17). This

result shows the duality of sensing and actuation, as expected by acoustic reciprocity principles. In sensing, maxima in directivity provide the dominant frequency components depending on direction of incoming waves, instead, in actuation, they give the excitation frequencies to generate waves along the associated directions.

2.4 Examples of directivities for simple geometries

The directivities of a circular patch, of a monolithic rectangular patch and of a rectangular array are illustrated as simple introductive examples.

2.4.1 Circular patch

The case of a circular piezo transducer can be modeled through the following expression for the function $f(\boldsymbol{x})$:

$$f(\boldsymbol{x}) = \text{rect}\left(\frac{|\boldsymbol{x}|}{a}\right) \tag{29}$$

where the function rect is defined as follows:

$$\text{rect}(\xi) = \begin{cases} 1, & |\xi| \leq 1 \\ 0, & |\xi| > 1 \end{cases} \tag{30}$$

and where a defines the radius of the disc. Figure 7 shows a configuration of the disc, where the black domain identifies the location of the piezoelectric material. The corresponding directivity is given by:

$$\mathcal{D}(\boldsymbol{k}_0(\omega), \theta) = a\frac{J_1(a|\boldsymbol{k}_0|)}{a|\boldsymbol{k}_0|} \tag{31}$$

where $J_1(x)$ is the first order Bessel function.

The directivity function clearly shows the absence of any particular direction, and indicates that preferential tuning occurs for wave modes corresponding to local maxima of the Bessel function. Such maxima can be found at $k_0 a = (2n-1)\frac{\pi}{2}$, where $n = 1, 2, ...$ is an integer. The directivity function in the wavenumber domain, as well

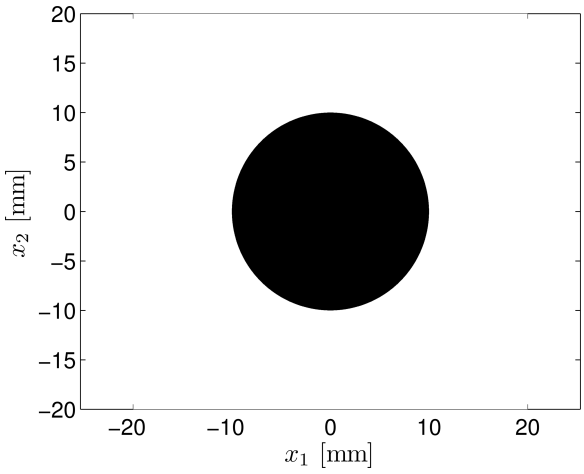

Figure 7: Circular piezo disc of radius $a = 10$ mm.

as the directivity curve for $k_0 = \frac{\pi}{2a}$ is presented in Fig. 8 to confirm the absence of any preferential direction.

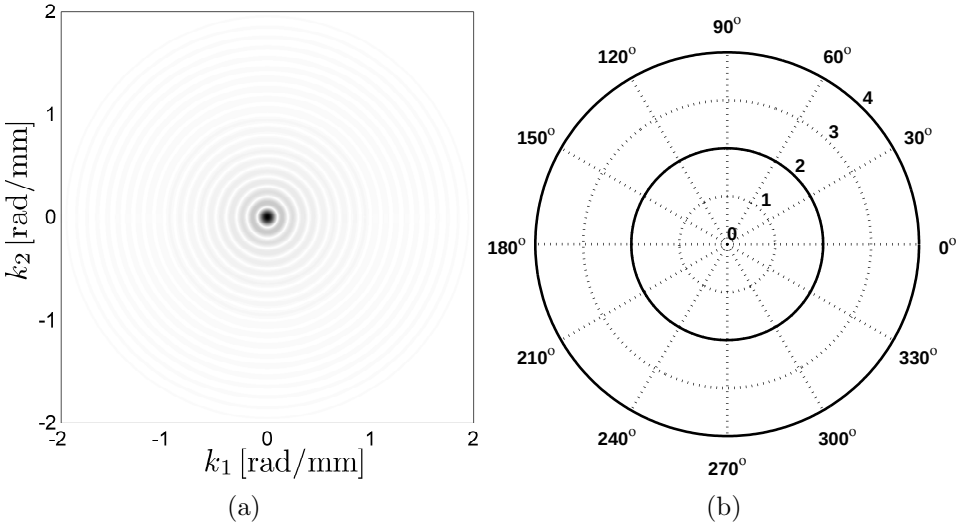

Figure 8: Wavenumber representation of the directivity function of the piezo disc of radius $a = 10$ mm (a), and directivity curve at $k_0 = \frac{\pi}{2a}$ (b).

2.4.2 Monolithic rectangular patch

The analysis above can be applied to the simple case of a monolithic rectangular patch, whose geometry is described by the following function:

$$f(\boldsymbol{x}) = \text{rect}\left(\frac{x_1}{a_1}\right)\text{rect}\left(\frac{x_2}{a_2}\right) \tag{32}$$

Here $2a_1, 2a_2$ define the dimensions of the patch along the x_1 and x_2 direction, assumed aligned with the principle directions of the rectangle.

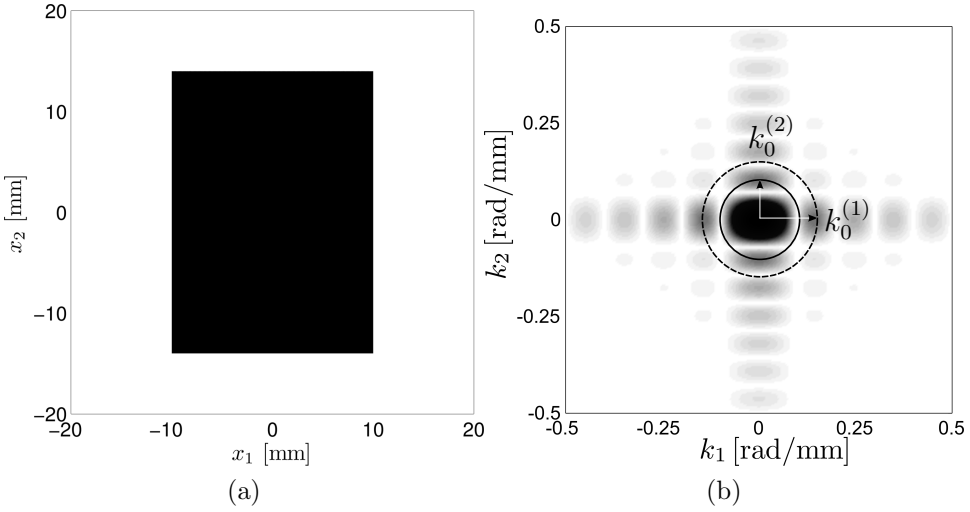

Figure 9: Rectangular piezo disc of dimensions $a_1 = 10$ mm, $a_2 = 14$ mm (a), and wavenumber representation of the directivity function (b).

The transducer's directivity, given by:

$$\mathcal{D}(\boldsymbol{k}_0(\omega), \theta) = a_1 a_2 \text{sinc}(a_1 k_0 \cos\theta)\text{sinc}(a_2 k_0 \sin\theta) \tag{33}$$

indicates that preferential directions of sensitivity/generation are aligned with the main dimensions of the rectangle, along which tuning occurs for wavenumber values which maximize the two sinc functions in Eq. (33). Figure 9(a) shows a patch of dimensions $a_1 = 10$ mm, $a_2 = 14$ mm, while the variation of the directivity in the wavenumber domain is presented in Fig. 9(b). Specifically, for a traveling wave at $\theta = 0$, maximum directivity occurs for wavenumbers $k_0^{(1)} = (2n_1 - 1)\frac{\pi}{2a_1}$, while for

waves propagating along the direction $\theta = \pi/2$, the transducer is tuned for $k_0^{(2)} = (2n_2 - 1)\frac{\pi}{2a_2}$, where n_1, n_2 are integers. The two tuning conditions are represented in Fig. 9(b) by dash and solid line circles of radius respectively equal to $k_0^{(1)}$ and $k_0^{(2)}$. The two circles intersect directivity maxima at locations k_1, k_2 which identify wave vector components of maximum directivity, i.e. $\boldsymbol{k}_0^{(1)} = k_0^{(1)}\boldsymbol{i}_1$ and $\boldsymbol{k}_0^{(2)} = k_0^{(2)}\boldsymbol{i}_2$. Wavenumber information can be directly related to frequency upon knowledge of the dispersion properties of the underlying medium. In particular, in sensing, one could consider situations where the transducer is able to discriminate between the two directions of maximum sensitivity ($\theta = 0$ and $\theta = \pi/2$), based on the frequency value (and corresponding wavenumber) recorded. In other words, the rectangular sensor acts as a spatial filter which is tuned to the $\theta = 0$ or $\theta = \pi/2$ direction depending on the frequency it receives. Similarly, in actuation, the transducer can generate waves in the two directions of maximum sensitivity ($\theta = 0$ and $\theta = \pi/2$), based on the frequency value of the voltage with which it is excited. The polar directivity curves of Fig. 10 illustrate the different directional patterns with strong lobes at $\theta = 0, \pi$ and at $\theta = \pm\pi/2$ wavenumbers $\boldsymbol{k}_0^{(1)}, \boldsymbol{k}_0^{(2)}$ (Fig. 10).

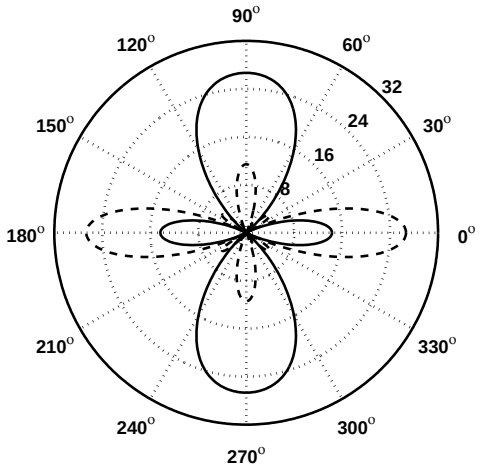

Figure 10: Rectangular piezo disc of dimensions $a_1 = 10$ mm, $a_2 = 14$ mm: directivity curves at $k_0^{(1)} = \frac{\pi}{2a_1}$ (dashed line), and at $k_0^{(2)} = \frac{\pi}{2a_2}$ (solid line).

2.4.3 Rectangular periodic array

Another simple case is a rectangular periodic array of point sources, whose geometry is described by the following function:

$$f(\boldsymbol{x}) = \sum_{n_1} \sum_{n_2} \delta(x_1 - x_{1n_1}) \delta(x_2 - x_{2n_2}) \tag{34}$$

where $\delta(\xi)$ is the Dirac delta function, defined as:

$$\delta(\xi) = \begin{cases} +\infty, & \xi = 0 \\ 0, & \xi \neq 0 \end{cases} \tag{35}$$

while $\boldsymbol{x}_{n_1,n_2} = [x_{1n_1},\ x_{2n_2}]$ defines the location of the point array element n_1, n_2, where the integers $-\frac{1}{2}(N_i - 1) \leq n_i \leq \frac{1}{2}(N_i - 1)$, while N_i defines the number of elements of the array in the i-th direction. Such location can be expressed as:

$$\boldsymbol{x}_{n_1,n_2} = n_1 d_1 \boldsymbol{i}_1 + n_2 d_2 \boldsymbol{i}_2 \tag{36}$$

where d_1, d_2 define the spacing of the array elements along the array directions, $\boldsymbol{i}_1,\ \boldsymbol{i}_2$. An example of a rectangular periodic array configuration is presented in Fig. 11.

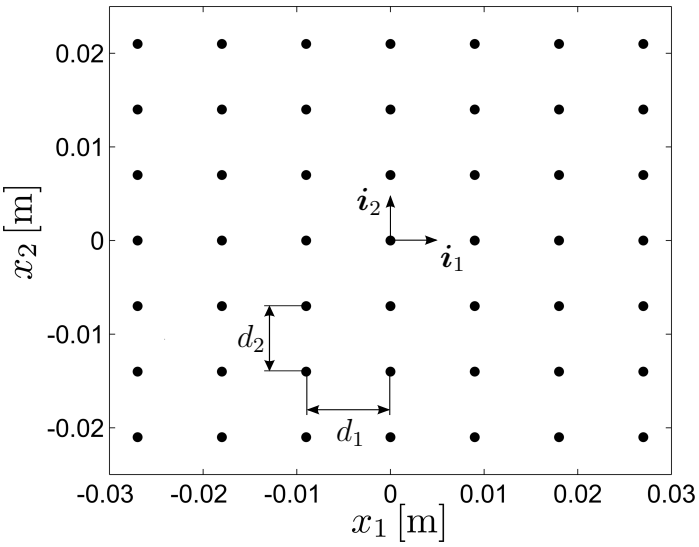

Figure 11: Periodic rectangular array.

The corresponding directivity can be evaluated through the spatial FT of the material distribution function in Eq. (34), which is given by:

$$\begin{aligned}\mathcal{D}(\boldsymbol{k}_0(\omega),\theta) &= \sum_{n_1}\sum_{n_2} e^{-i\boldsymbol{k}_0\cdot\boldsymbol{x}_{n_1,n_2}} \\ &= \sum_{n_1}\sum_{n_2} e^{-i(n_1 d_1 \boldsymbol{i}_1\cdot\boldsymbol{k}_0 + n_2 d_2 \boldsymbol{i}_2\cdot\boldsymbol{k}_0)}\end{aligned} \tag{37}$$

Upon manipulation, Eq. (37) can be conveniently rewritten as:

$$\mathcal{D}(\boldsymbol{k}_0(\omega),\theta) = \frac{\sin(\frac{N_1}{2} d_1 \boldsymbol{i}_1\cdot\boldsymbol{k}_0)}{\sin(\frac{1}{2} d_1 \boldsymbol{i}_1\cdot\boldsymbol{k}_0)} \frac{\sin(\frac{N_2}{2} d_2 \boldsymbol{i}_2\cdot\boldsymbol{k}_0)}{\sin(\frac{1}{2} d_2 \boldsymbol{i}_2\cdot\boldsymbol{k}_0)} \tag{38}$$

The variation of the directivity, obtained for $N_1 = 7,\ N_2 = 7$, $d_1 = 9$ mm, $d_2 = 7$ mm, in terms of the wave vector components is shown in Fig. 12.

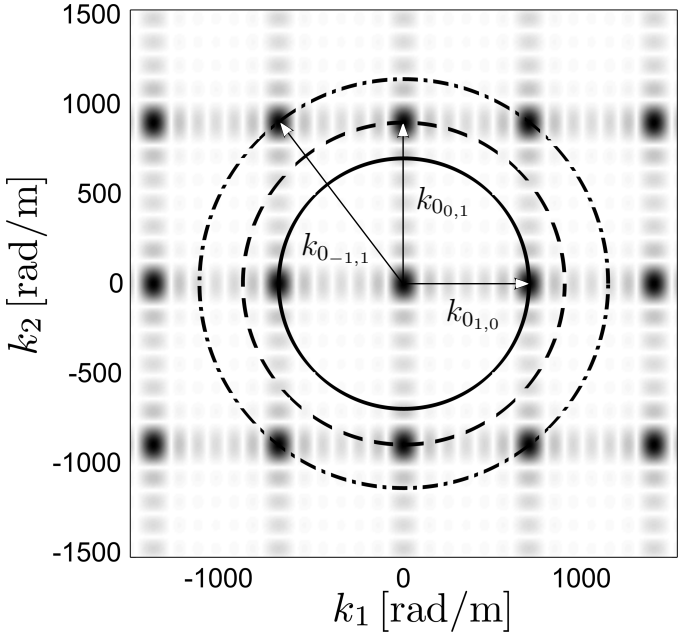

Figure 12: Rectangular array directivity function. Visualization of $k_{0_{p,q}}$ for $[p,q] = [0,1]$, $[1,0]$ and $[-1,0]$.

The wavenumber values which maximize Eq. (38) are obtained as solutions of the following system of equations for a given pair of integers p, q:

$$\begin{aligned} d_1 \boldsymbol{i}_1\cdot\boldsymbol{k}_{0_{p,q}} &= 2p\pi \\ d_2 \boldsymbol{i}_2\cdot\boldsymbol{k}_{0_{p,q}} &= 2q\pi \end{aligned} \tag{39}$$

The solution of Eq. (39) is associated with a wave vector $\boldsymbol{k}_{0_{p,q}}$ whose direction is given by:

$$\theta_{p,q} = \arctan\left(\frac{k_{02_{p,q}}}{k_{01_{p,q}}}\right) \tag{40}$$

The selection of a particular peak in the directivity distribution can be performed by determining the wavenumber corresponding to the radius of a circle intersecting the peak of interest. Directivity curves for various combinations of the integer pairs p, q are shown in Fig. 13. In particular strong lobes at $\theta = 0, \pi$ occur for $k_{0_{1,0}} = 2\pi/d_1$ (Fig. 13(a)) and at $\theta = \pm\pi/2$ for $k_{0_{0,1}} = 2\pi/d_2$ (Fig. 13(b)). In the case of a square periodic array, i.e. $d_1 = d_2$, it would be $k_{0_{1,0}} = k_{0_{0,1}}$ and both the horizontal and vertical direction would be associated to the same wavenumber. Looking at the case $p = -1, q = 1$ (Fig. 13(c)), the polar plot of the directivity shows the coupling between two directions. The three polar plots of Fig. 13 illustrates the directional capabilities of the rectangular array; only the horizontal and the vertical directions can be picked singularly, in all the other cases there is the coupling of at least two directions.

2.5 Conclusions

In this chapter, the equations for sensing and actuation of Lamb waves by piezo patches of arbitrary shapes have been provided. Under the main assumptions of thin piezo patches, propagating plane waves and through the thickness polarization, an expression of the transducers directivity has been formulated based on spatial distribution of active material, valid for both wave sensing and actuation, in agreement with acoustic reciprocity principles. Directivities for simple transducers configurations, i.e. circular patch, rectangular patch, and rectangular array of point sources, have been evaluated as introductory examples, giving the basic tools for the further transducer design analysis. In the next chapter, a generalization of the array configuration is considered, and after the theoretical analysis, the concept of frequency based beam steering is validated experimentally.

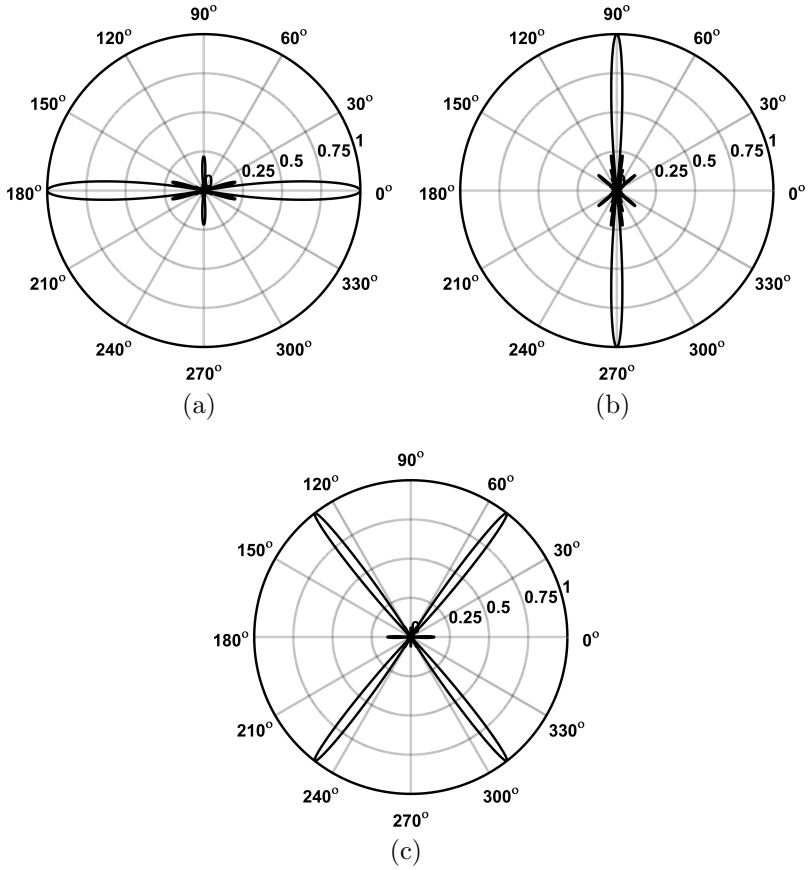

Figure 13: Array directivity curves for various values of the p, q pair: $p = 1, q = 0$ (a), $p = 0, q = 1$ (b), $p = -1, q = 1$ (c).

CHAPTER III

FREQUENCY STEERING THROUGH A QUADRILATERAL PERIODIC ARRAY

3.1 Overview

In this chapter, an FSAT with a quadrilateral periodic array configuration is analyzed. This is a generalization of the rectangular periodic array presented in Section 2.4.3. After illustrating the array geometry, its directional performance is evaluated based on the procedure outlined in Section 2.4.2. Numerical and experimental validations are presented. At the end of the chapter, the array is numerically tested on a composite plate, showing that FSATs can be applied also on non-isotropic substrates.

Even if the directionality of the array is still too limited to perform SHM operations, the periodic array discussed herein is a valuable demonstration of the concept of frequency-dependent directionality.

3.2 Configuration

In Section 2.4.3, each element of the rectangular array was considered as a point source. Here, the array elements are realistically modeled as discs. Thus, the array is defined by a material distribution function $f(\boldsymbol{x})$ expressed as:

$$f(\boldsymbol{x}) = \sum_{n_1} \sum_{n_2} \text{rect}\left(\frac{|\boldsymbol{x} - \boldsymbol{x}_{n_1,n_2}|}{a}\right) \tag{41}$$

where a is the radius of each disc, while $\boldsymbol{x}_{n_1,n_2}$ defines the location of the center of the disc n_1, n_2, where the integers $-\frac{1}{2}(N_i - 1) \leq n_i \leq \frac{1}{2}(N_i - 1)$, while N_i defines the number of elements of the array in the i-th direction. The position of each member can be expressed as:

$$\boldsymbol{x}_{n_1,n_2} = n_1\boldsymbol{e}_1 + n_2\boldsymbol{e}_2 \tag{42}$$

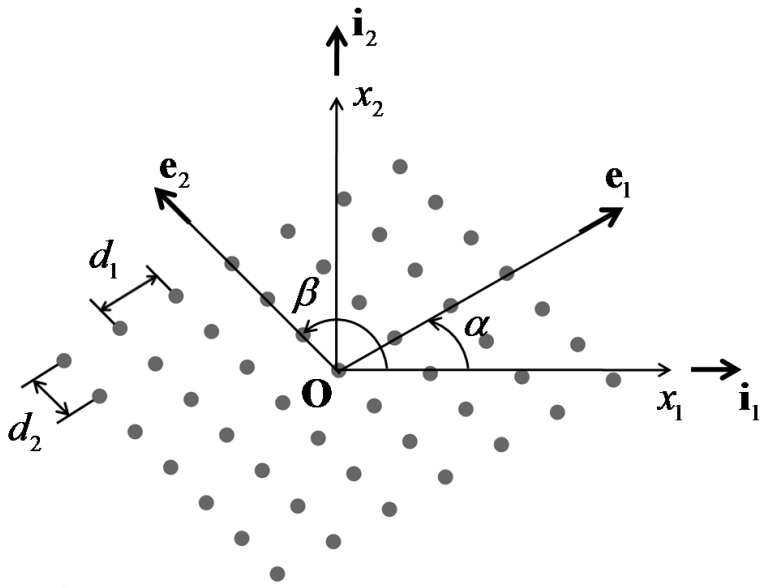

Figure 14: Periodic piezo array.

In Eq. (42), $\boldsymbol{e}_1$, $\boldsymbol{e}_2$ are two vectors defining the periodicity of the array, that according to the configuration presented in Fig. 14, can be generally written as:

$$\begin{aligned} \boldsymbol{e}_1 &= d_1 \cos\alpha \boldsymbol{i}_1 + d_1 \sin\alpha \boldsymbol{i}_2 \\ \boldsymbol{e}_2 &= d_2 \cos\beta \boldsymbol{i}_1 + d_2 \sin\beta \boldsymbol{i}_2 \end{aligned} \tag{43}$$

where d_1, d_2 define the spacing of the array elements along the array directions, while α, β are the angles formed by $\boldsymbol{e}_1$ and $\boldsymbol{e}_2$ with respect to $\boldsymbol{i}_1$ respectively. For $\beta - \alpha = \pi/2$, the case of the rectangular array is recovered.

3.3 Directivity

The directivity of the array can be evaluated through the spatial FT of the material distribution function in Eq. (41), which is given by:

$$\begin{aligned} \mathcal{D}(\boldsymbol{k}_0(\omega), \theta) &= a \, \frac{J_1(a|\boldsymbol{k}_0|)}{a|\boldsymbol{k}_0|} \sum_{n_1} \sum_{n_2} e^{-i\boldsymbol{k}_0 \cdot \boldsymbol{x}_{n_1,n_2}} \\ &= a \, \frac{J_1(a|\boldsymbol{k}_0|)}{a|\boldsymbol{k}_0|} \sum_{n_1} \sum_{n_2} e^{-i(n_1 \boldsymbol{e}_1 \cdot \boldsymbol{k}_0 + n_2 \boldsymbol{e}_2 \cdot \boldsymbol{k}_0)} \end{aligned} \tag{44}$$

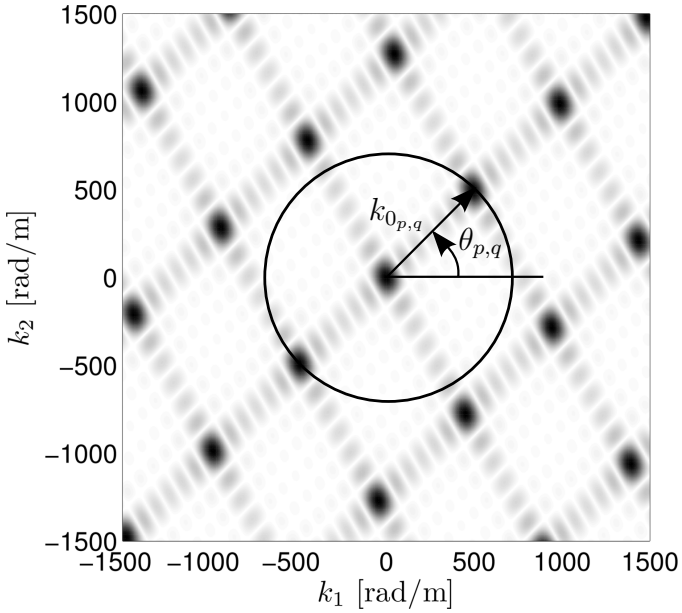

Figure 15: Quadrilateral array directivity function. Visualization of $k_{0_{p,q}}$ and associated direction $\theta_{p,q}$ for $p = 1$ and $q = 0$.

Upon manipulation, Eq. (44) can be conveniently rewritten as:

$$\mathcal{D}(\boldsymbol{k}_0(\omega), \theta) = a \ \frac{J_1(a|\boldsymbol{k}_0|)}{a|\boldsymbol{k}_0|} \frac{\sin(\frac{N_1}{2}\boldsymbol{e}_1 \cdot \boldsymbol{k}_0)}{\sin(\frac{1}{2}\boldsymbol{e}_1 \cdot \boldsymbol{k}_0)} \frac{\sin(\frac{N_2}{2}\boldsymbol{e}_2 \cdot \boldsymbol{k}_0)}{\sin(\frac{1}{2}\boldsymbol{e}_2 \cdot \boldsymbol{k}_0)} \tag{45}$$

The variation of the directivity, obtained for $a = 5$ mm, $N_1 = 7$, $N_2 = 7$, $d_1 = 9.9$ mm, $d_2 = 7.6$ mm, $\alpha = 30\pi/180$, $\beta = 135\pi/180$, in terms of the wave vector components is shown in Fig. 15. The choice of the parameters values has been determined by a trial and error approach, to obtain a directivity in 4 distinct directions. The wavenumber values which maximize Eq. (45) are obtained as solutions of the following system of equations for a given pair of integers p, q:

$$\begin{aligned} \boldsymbol{e}_1 \cdot \boldsymbol{k}_{0_{p,q}} &= 2p\pi \\ \boldsymbol{e}_2 \cdot \boldsymbol{k}_{0_{p,q}} &= 2q\pi \end{aligned} \tag{46}$$

The solution of Eq. (46) is associated with a wave vector $\boldsymbol{k}_{0_{p,q}}$ whose direction is given by:

$$\theta_{p,q} = \arctan\left(\frac{k_{02_{p,q}}}{k_{01_{p,q}}}\right) \tag{47}$$

Graphically, the wavevectors $\boldsymbol{k}_{0_{p,q}}$ of maximum directivity, can be obtained by selecting a particular peak in the directivity distribution, which is equivalent in choosing a pair of p, q, and determining the wavenumber corresponding to the radius of a circle intersecting the peak of interest. In this way, $\boldsymbol{k}_{0_{p,q}}$ is determined and its associated direction is defined by the angle $\theta_{p,q}$ between a center starting line connecting the selected peak and the horizontal axis k_1 (Fig. 15). Directivity curves for various combinations of the integer pairs p, q are shown in Fig. 16. Compared to the results obtained for the rectangular array in Fig. 9, the improvement is evident; the quadrilateral array shows four directions fully decoupled, instead of the only two of the previous case. This is due to the choice of $\beta - \alpha \neq \pi/2$. In fact, breaking the symmetry of the array geometry, i.e. $d_1 \neq d_2$ and $\beta - \alpha \neq \pi/2$, results in a directivity function with at least four pairs of peaks associated to four distinct wavevectors $\boldsymbol{k}_{0_{p,q}}$.

Directional sensing/actuation at the considered 4 directions corresponding to the main lobes in Fig. 16 occurs at the values of frequencies which satisfy the following relation:

$$\mathcal{D}(\boldsymbol{k}_{0_{p,q}}, \omega) = 0 \tag{48}$$

which defines the dispersion relation of the considered medium, whose solution provides the value of frequency $\omega_{p,q}$ at which the array radiates at the angle $\theta_{p,q}$.

In the following sections of this chapter, the periodic array is considered for generation of Lamb waves in isotropic aluminum plates. First, considerations about guided wave mode tuning are given. Next, numerical evaluation of the array directional capabilities is provided. Then, an array prototype is realized and an experimental validation is carried. Finally, the array application to anisotropic composite plates is simulated numerically.

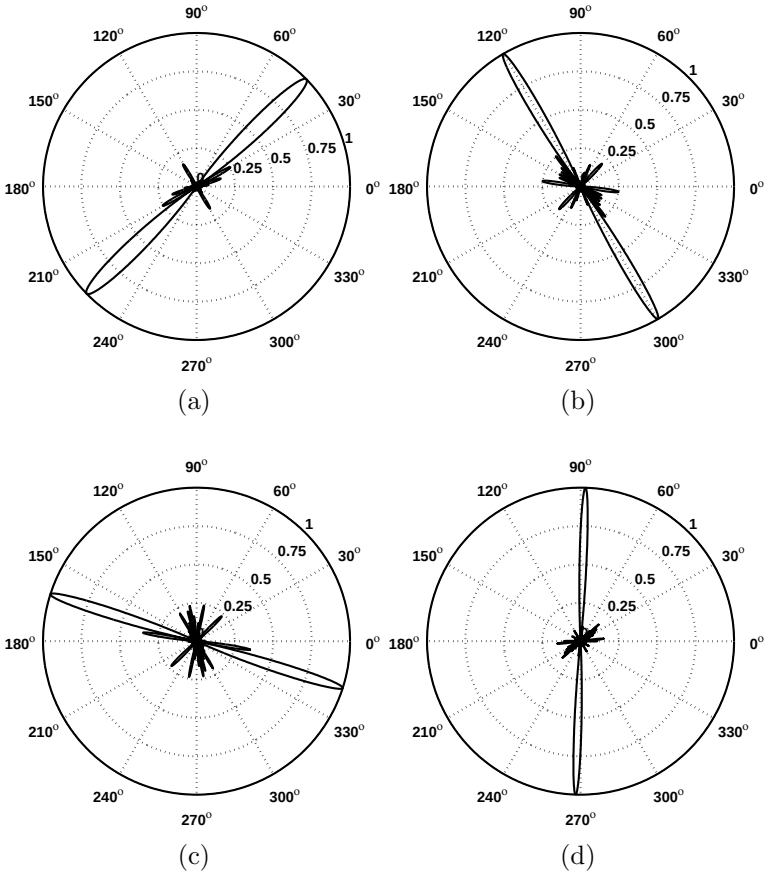

Figure 16: Array directivity curves for various values of the p, q pair: $p = 1, q = 0$ (a), $p = 0, q = 1$ (b), $p = -1, q = 1$ (c), $p = 1, q = 1$ (d).

3.4 Wave Mode Tuning

The considered array configuration essentially operates as a spatial filter, which generates waves at a wavenumber defined by the periodicity of the array. The selection of the wavenumber is driven by the excitation frequency, which determines the intersection between the dispersion surface and the peak of the excitation distribution in the wavenumber domain. In the case of multimodal wave propagation, as in the case of GWs, a wavenumber is associated with multiple frequencies corresponding to the various modes of propagation, as it is illustrated in Fig. 17 for the case of Lamb waves in a 1 mm thick aluminum plate.

The ability to select the excited wavenumber through frequency selection allows

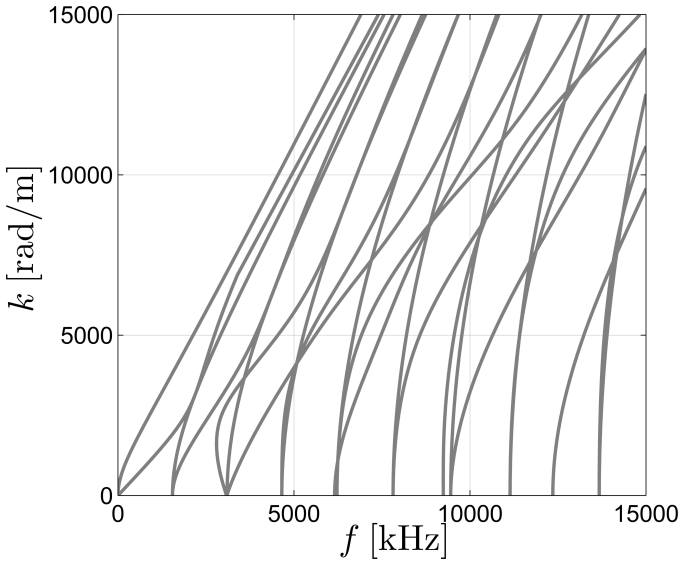

Figure 17: Lamb waves dispersion curves for a 1 mm thick aluminum plate.

the choice of a specific wave mode to be generated. From this perspective, the considered array also allows wave mode tuning, in addition to the beam steering properties discussed above. To avoid a mode multiplicity bigger than two, the frequency of interest is considered in a range below the cut-off for the A_1 mode, so that only A_0 and S_0 modes are supported. In this way, the dispersion curves for the considered 1 mm thick aluminum plate reduce from those presented in Fig. 17 and result simply in those depicted in Fig. 18, which also shows how the wavenumber $k_{0_{p,q}}$ can be generated by excitation at two frequencies $f_{A_{0p,q}}$ and $f_{S_{0p,q}}$. The choice of the excitation frequency between $f_{A_{0p,q}}$ and $f_{S_{0p,q}}$ defines the excited mode A_0 or S_0 as well as a direction of radiation defined by the integer pair p, q and corresponding radiation angle $\theta_{p,q}$. Assuming to tune the array on the A_0 mode, it is worth noting that exciting the array at $f_{A_{0p,q}}$, not only enables an A_0 wave, characterized by $k_{0_{p,q}}$, but also potentially generates an S_0 wave, characterized by $k'_{0_{p,q}}$, at the same time. To avoid the activation of an additional steering direction, due to S_0, it is necessary that no peaks associated to $k'_{0_{p,q}}$ are present in the array directivity function (Fig. 15).

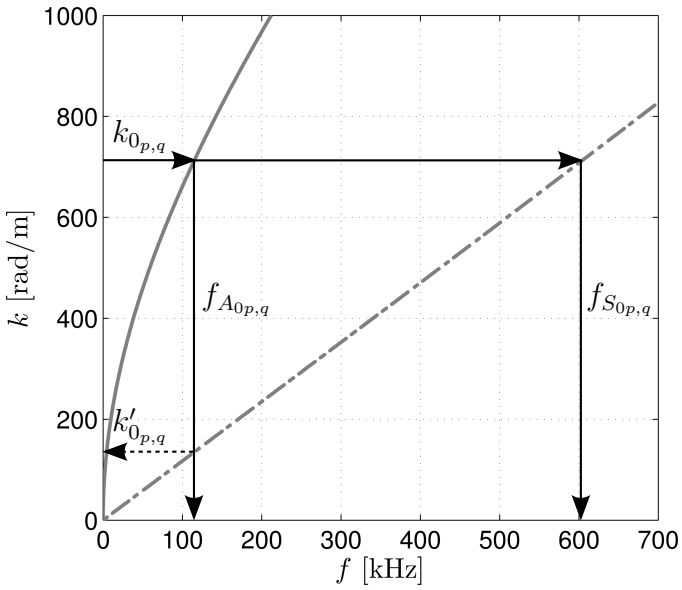

Figure 18: A_0 mode steering frequency determination of the array on a 1 mm aluminum plate. A_0 mode solid line; S_0 mode dashed–dotted line.

3.5 Numerical Evaluation of the Array Performance

The performance of an array for the directional generation of guided waves is evaluated numerically in support of the experimental validation of the concept presented in the following section. The array consists of surface-mounted piezoelectric discs operating in shear mode and applying a periodic distribution of surface traction. The adopted numerical procedure is briefly outlined in Section 3.5.1 and the obtained numerical results are presented in Section 3.5.2.

3.5.1 Array model

The developed numerical model follows the approach described in detail in [67], where the array design is based on the point source approximation to locate the maxima of the surface traction distribution. The plate response is computed as a superposition of the contributions of the individual circular discs following the semi-analytical procedure presented in [63].

The governing equation of the plate is the 3D equation of elasticity for isotropic

plates in the absence of body forces:

$$\mu\nabla^2\mathbf{u} + (\lambda+\mu)\nabla\nabla\cdot\mathbf{u} = \rho\ddot{\mathbf{u}} \tag{49}$$

where λ and μ are the Lamé constants, and where $\mathbf{u} = \{u_1, u_2, u_3\}^T$ is the displacement vector of a material point. The analytical solution of Eq. (49) for the case of a plate excited by a single piezo disc has been presented by Raghavan in [63] and is summarized in Romanoni *et al.* in [67] as:

$$u_{Di} = u_{Di}(r, \theta, h, \omega), \qquad i = 1, 2, 3 \tag{50}$$

where r, θ are polar coordinates with origin at the center of the piezo, as shown in Fig. 19, and h is the thickness of the plate. The sub–script D emphasizes that the displacements field obtained is for a single disc.

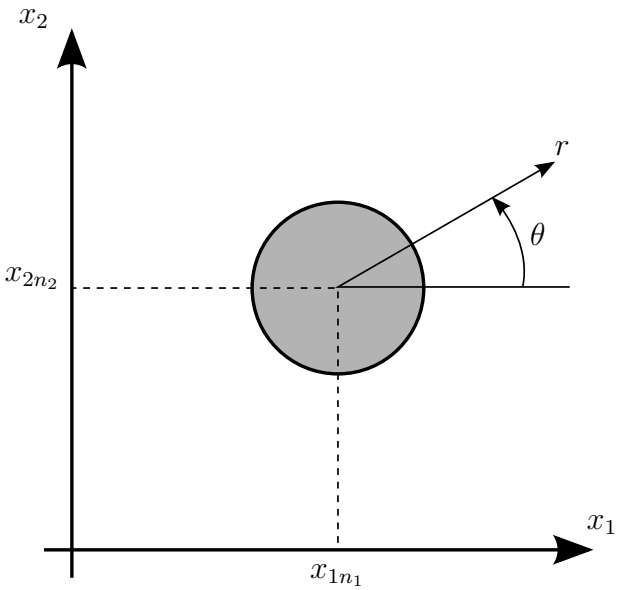

Figure 19: Local polar reference system r, θ with origin at the center of the piezo disc.

To compute the response of the entire piezo disc array, it is better to express the contribution of each actuator in the global x_1, x_2 cartesian reference system, which

Table 2: 2D quadrilateral array beam steering directions, wavenumbers and corresponding A_0 mode frequencies

$k_{0_{p,q}}$ [rad/m]	$\theta_{p,q}[^\circ]$	$f_{A_{0p,q}}$ [kHz]
658	45	95
851	120	150
931	-17	200
1203	88	280

means to perform a coordinate transformation of the displacement solution of Eq. (50), converting the local pair r, θ to the global pair $x_1 - x_{1n_1}, x_2 - x_{2n_2}$. The response of a piezo disc array, u_i, can now be computed through linear superposition:

$$u_i(x_1, x_2, \omega) = \sum_{n1} \sum_{n2} u_{Di}(x_1 - x_{1n_1}, x_2 - x_{2n_2}, \omega) \tag{51}$$

Note that u_i is obtained as the combination of the symmetric (S_0) and anti-symmetric (A_0) mode contributions and that no higher modes are excited in the interested range of frequency.

3.5.2 Results

The analysis is conducted considering an aluminum plate (Young's modulus $E = 69$ GPa, Poisson's ratio $\nu = 0.33$, density $\rho = 2700\,\mathrm{kg/m^3}$, thickness $h = 1$ mm) on which a 7×7 array of 5 mm diameter piezo discs are bonded resulting in a configuration presented in Fig. 20. Specifically, the array parameters are the same as those used to generate Figs. 15 and 16, and for simplicity are reminded here: $d_1 = 9.9$ mm, $d_2 = 7.6$ mm, $\alpha = 30^\circ$ and $\beta = 135^\circ$. The first four lowest steering wavenumbers, with the corresponding radiation angles and excitation frequencies for the A_0 mode are listed in Table 2.

The dispersion circles at the frequencies listed in Table 2 for the considered array are shown in Fig. 21, to illustrate the directional properties of the array at the considered excitation frequencies.

The array is driven by a 7–cycles burst sine shown in Fig. 22, for the case of

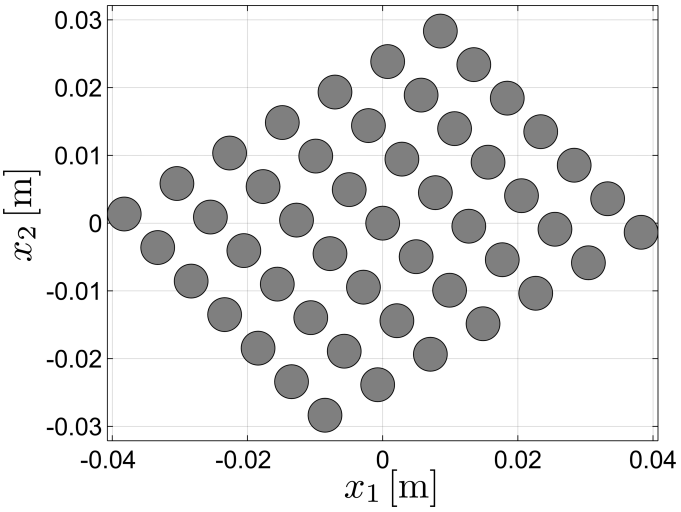

Figure 20: Quadrilateral array configuration.

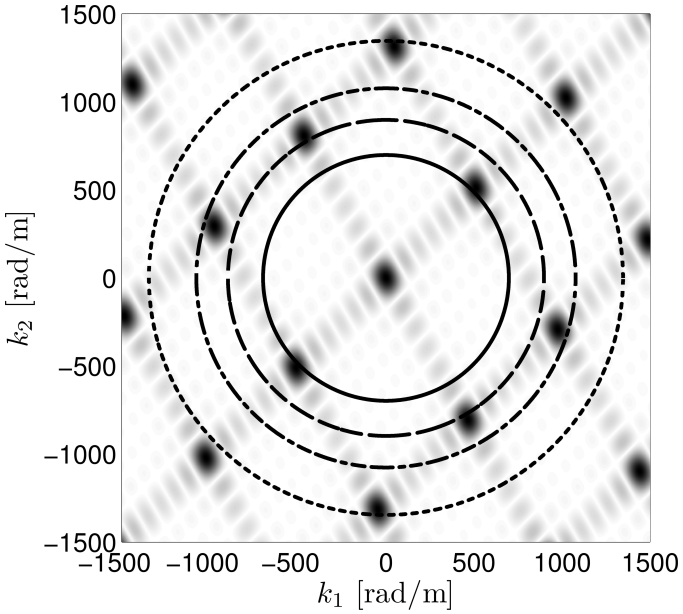

Figure 21: Location of array directivity maxima in the wavenumber domain, and intersection with dispersion relation at frequency $f_{A_{0p,q}}$: 95 kHz (solid line), 150 kHz (dashed line), 200 kHz (dash-dotted line), 280 kHz (dotted line)

95 kHz center frequency. The frequency range included in the 3–dB limits can be considered the relevant frequency bandwidth of the signal. As seen is Section 3.4, an exciting frequency, through the medium dispersion relation, generates a wave with a determined wavenumber. Therefore, because the sine burst is characterized by a frequency bandwidth, it generates a wave packet characterized by a bandwidth in the wave number domain, which is represented schematically in Fig. 23, with solid circles corresponding to the center frequency and the dashed circles defining the 3–dB limits. The region enclosed by the 3–dB limits crosses only a pair of array directivity peaks, preserving the directionality of the array.

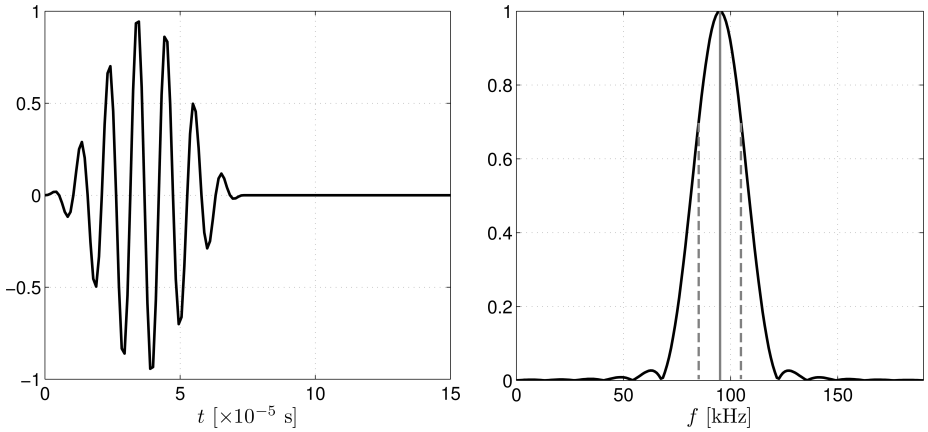

Figure 22: Tone burst 7–cycles centered at 95 kHz: time domain (a); spectrum (solid line: center frequency, dashed line: 3-dB bandwidth limits) (b).

Figure 24 shows the plate out-of-plane response for burst excitations centered at the frequencies listed in Table 2. The plots, which represent the magnitude of the response evaluated at the center frequency, clearly show the directional characteristics of radiation, and confirm the radiation directions predicted through the directivity analysis summarized in Fig. 16. The presence of low magnitude responses in radiation angles other than the predicted ones is caused by the intersections of the dispersion circles (Fig. 21) with the secondary and much lower directivity peaks which activate

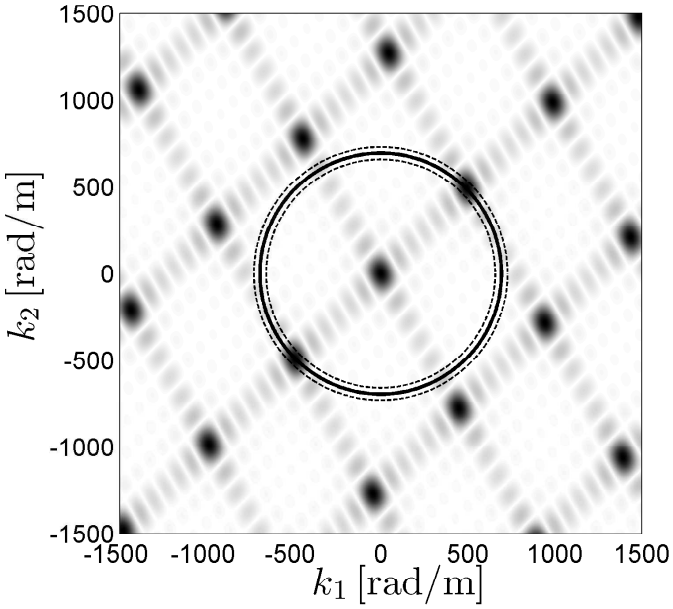

Figure 23: Wavenumber content of a tone burst excitation (solid line: center frequency, dashed line: 3-dB bandwidth limits).

secondary lobes in the radiation pattern.

3.6 Experimental Evaluation of the Array Performance

This section presents the experimental characterization of the quadrilateral array considered in this study. A first step towards the validation of the numerical predictions of steering frequencies requires the experimental evaluation of the dispersion curves for the plate under consideration and their correlation with the analytical ones used for the array design. This is achieved by exciting the considered plate with a single piezo disc mounted at its center, by recording full wavefield data over the plate surface, and by post-processing the response to evaluate its wavenumber content at various frequencies. The array is subsequently mounted on the plate and its directivity is evaluated through a two-step process. The steering frequencies are first found through the analysis of the broadband response of the plate. Narrow-band excitation at the steering frequencies is then used to evaluate the directivity of the array and compare it with the numerical predictions.

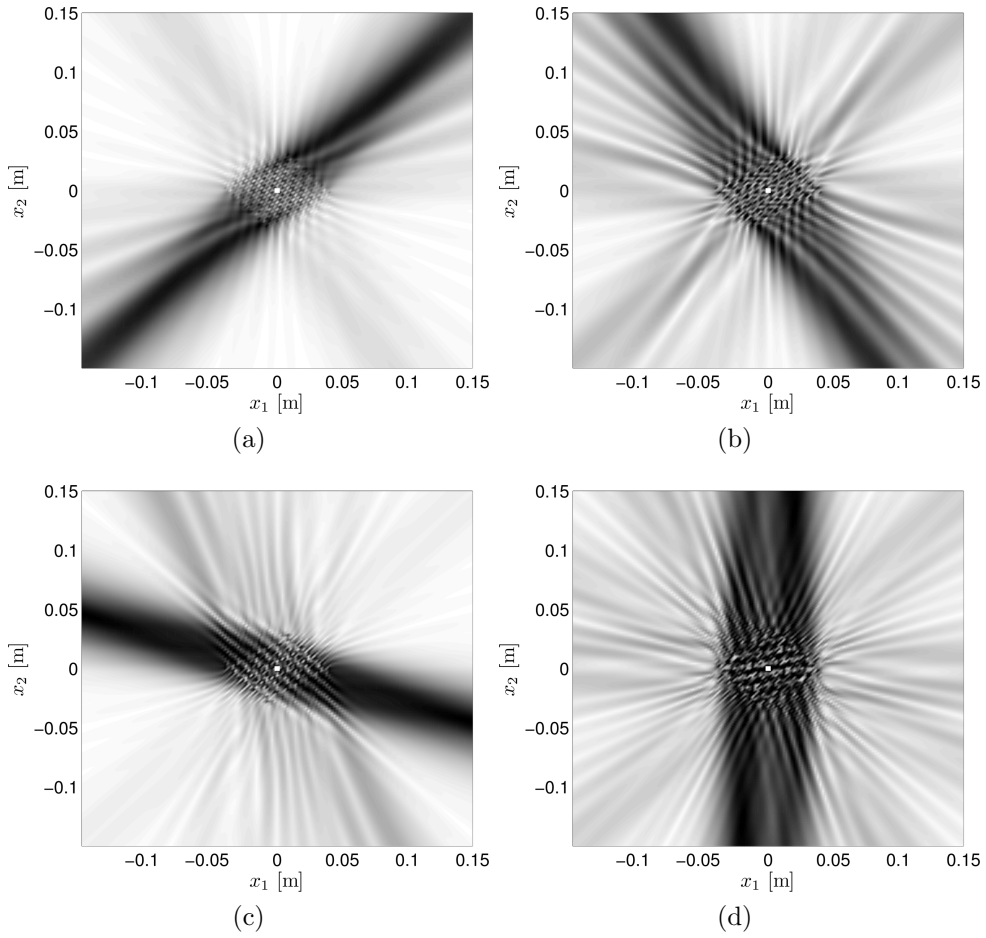

Figure 24: Simulation of plate response for burst excitation centered at the directional frequencies of Table 2: (a) 45° @ 95 kHz; (b) 120° @ 150 kHz; (c) −17° @ 200 kHz; (d) 88° @ 280 kHz.

3.6.1 Dispersion Curve Correlation

Experimental estimation of the dispersion properties is conducted by instrumenting the plate with a single 5 mm diameter PZT transducer driven by a broadband pulse. The plate response is recorded by a SLDV which scans a square region of dimensions 220 mm $\times$ 220 mm. The spatial resolution of the measurements corresponds to a grid with horizontal and vertical spacing respectively equal to $\Delta x_1 = \Delta x_2 = 2.2$ mm. These scan region dimension and grid spacings allow to perform the following wavenumber analysis avoiding spatial aliasing up to 1428 rad/m and with a wavenumber resolution, $\Delta k = 29$ rad/m, values considered sufficient to assure an accurate analysis.

The captured wavefield $u_3(x_1, x_2, t)$ is transformed to the frequency/wavenumber domain to obtain $\hat{u}_3(k_1, k_2, \omega)$ using a 3D FT, which is defined as:

$$\hat{u}_3(k_1, k_2, \omega) = \int_{-\infty}^{+\infty}\int_{-\infty}^{+\infty}\int_{-\infty}^{+\infty} u_3(x_1, x_2, t) e^{-jk_1x_1} e^{-jk_2x_2} e^{-j\omega t} dx_1 dx_2 dt \tag{52}$$

where k_1, k_2 are the wave vector components along the horizontal and vertical axis, respectively.

The obtained values of $\hat{u}_3(k_1, k_2, \omega)$ are stored in a 3D matrix, which can be graphically represented as a succession of wavenumbers cross–sections referred at different frequencies, as it is portrayed in Fig. 25. In this way, each bi–dimensional wavenumbers cross–section contains the transformed displacement $\hat{u}_3(k_1, k_2, \omega)$ at a particular frequency.

Contour plots of a wavenumber cross–section at a specific frequency ω_0, which gives $\hat{u}_3(k_1, k_2, \omega = \omega_0)$, show the wavenumber content of the plate response at the considered frequency ω_0 as illustrated in Fig. 26. The omni–directional excitation

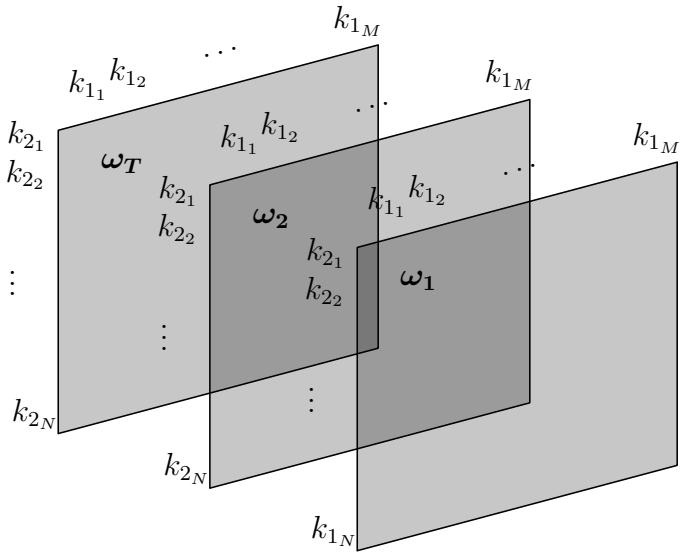

Figure 25: Schematic visualization of $\hat{u}_3(k_1, k_2, \omega)$ 3D data structure. Transformed displacement $\hat{u}_3(k_1, k_2, \omega)$ is stored in a succession of bi–dimensional matrices (gray squares) spanning the wavenumber domain at each frequency, forming a 3D matrix.

provided by the single piezo disc is illustrated by the contour circles found for various excitation frequencies (105 kHz, 150 kHz, 200 kHz and 280 kHz). The analytical A_0 dispersion circles, obtained using a Semi–Analytical Finite Element (SAFE) method [55, 10], are the superimposed dashed curves and show an excellent agreement with the experimental dispersion circles, which indicates that accurate knowledge of the properties of the plate can be used for the actuator design and correlation between numerical and experimental performance. It is interesting to note that for the shown frequencies a single circle is observed from the analysis of the experimental data, corresponding to the A_0 mode. The S_0 mode can be seldom visualized given it predominant in–plane polarization. For this reason, S_0 is hard to be recorded through an SLDV, which detects out–of–plane displacements. On the contrary, A_0 is mainly an out–of–plane mode, and, in a SLDV acquisition, it results to be the dominant mode, as confirmed by the obtained contour plots.

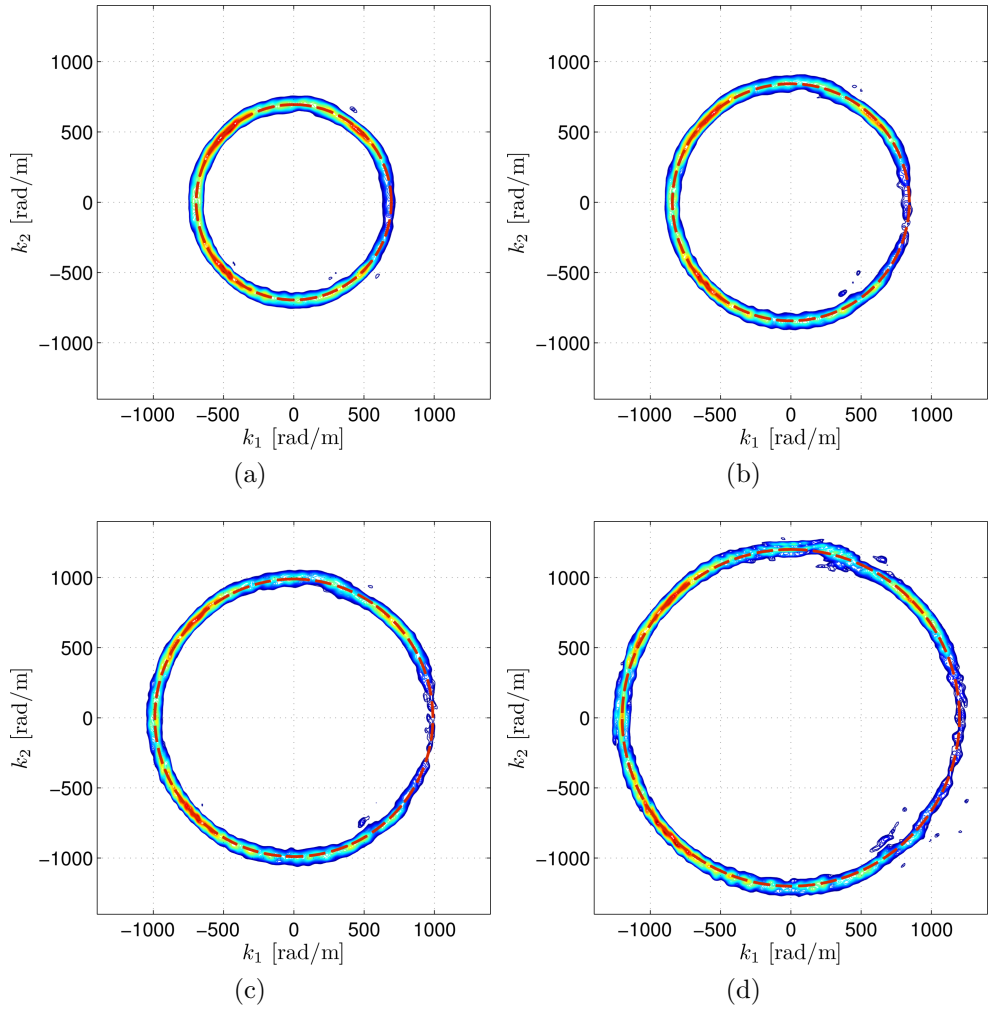

Figure 26: Analytical (dashed line) and experimental (contour plot) A_0 mode dispersion circles of a 1 mm 6061 aluminum plate at frequency (linear scale): (a) 105 kHz; (b) 150 kHz; (c) 200 kHz; (d) 280 kHz

3.6.2 Array Configuration

A 7×7 2D periodic array, as described in Section 4.4, was implemented on a 6061 aluminum plate of dimension 957 mm × 890 mm × 1 mm. The array uses 5 mm diameter PZT disc transducers with spacing of 7.6 mm and 9.9 mm (Fig. 27). The transducers are bonded to the plate with electrically conductive epoxy so that the entire plate can be used as the ground. Also, top electrodes of the transducers are connected together with copper tape serving as the positive terminal. Thus, all the transducers in the array can be excited simultaneously by only two wires. For the

purpose of insulation, stripes of electrical tape were placed in between the transducers.

The discs are driven first by a broadband pulse from a Panametrics-NDT 5058PR pulser to find the experimental steering frequencies of the array and, then, by amplified 7-count tone bursts, provided by an Agilent 33220A function generator, to evaluate array directivity. At 900 volts level, the pulser has the $10\% - 90\%$ rise time $t_{rise} \leq 40$ ns. The bandwidth of the pulse can be estimated as BW $= 0.35/t_{rise} =$ 8.75 MHz [30], which is wide enough to excite the bandwidth of interest (< 300 kHz). When excited by the pulser, the SLDV was set to filter out unwanted frequency components by using a bandpass filter ranging from 10kHz to 500kHz. When excited by tone bursts, the bandpass filter was set to ± 10 kHz around the tone burst central frequency.

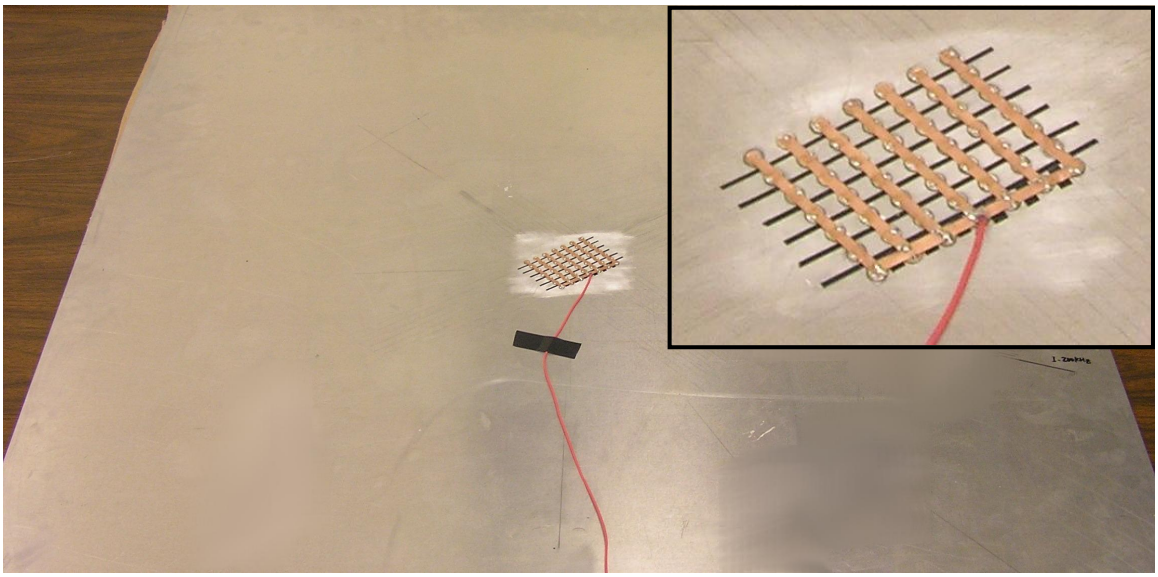

Figure 27: Quadrilateral array made by PZT discs mounted on an aluminum plate.

3.6.3 Array Characterization Using Broadband Pulses

The first step in the characterization of the array's radiation directivity consists in identifying the radiation directions and the corresponding steering frequencies. This can be efficiently done by using the pulser to excite the array and record the wavefield

data $u_3(x_1, x_2, t)$. For broadband excitations, the array radiates mostly at the frequencies of intersection of the dispersion curves and the maxima of array directivity function, $|\mathcal{D}(\boldsymbol{k}_0(\omega), \theta)|$. At these frequencies, the array radiates along the corresponding steering directions. Such radiation patterns can be visualized by evaluating and plotting the root mean square (RMS) value of the plate response, which is defined as:

$$RMS(x_1, x_2) = \sqrt{\sum_{i=1}^{N} u_3(x_1, x_2, t_i)^2 / N} \tag{53}$$

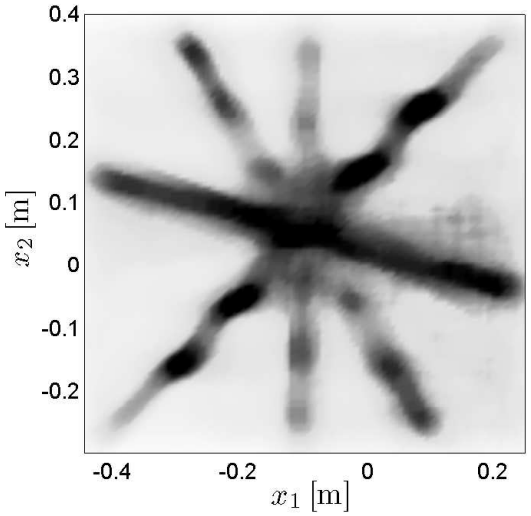

Figure 28: Array RMS radiation pattern using broadband pulses.

where N is the number of time samples. The results of Fig. 28 clearly show four evident radiation directions. Subsequent frequency analysis of the data identifies the frequencies corresponding to each directional response as $\approx 105, 150, 200$ and 280 kHz, which correlate well with the theoretical predictions of Table 2, with the exception of the first experimental value which is approximately 10% higher. The discrepancy may be caused by a not precise disc transducers positioning during the array installation on the plate, which results in an altered array directivity function with maxima shifted from their expected position.

3.6.4 Array Characterization Using Narrowband Tone Bursts

With the knowledge of the steering frequencies identified in Section 3.6.3, narrowband tone bursts centered at the steering frequencies were employed to better evaluate the radiation patterns, given the fact that tone bursts concentrate the excitation energy in a narrow frequency bandwidth. Again, the radiation pattern of the array at the steering frequencies can be characterized in the time domain through RMS values of the wavefield data, as described by Eq. (53). The results are depicted in Fig. 29, which are in good agreement with those of Fig. 28 using the pulse excitation and with the numerical predictions presented in Fig. 24 of Section 4.4.

Alternatively, the wavefield data are interpreted in the frequency/wavenumber domain, which shows the directionality of the array as peaks associated with a specific wavenumber vector and a corresponding radiation direction. This representation highlights a clear difference between the wavenumber content of the single, omnidirectional disc transducer used for the dispersion analysis, whose response is characterized by circular contours (Fig. 26). The array radiation patterns presented in Fig. 30 are superimposed with the A_0 mode analytical dispersion circles (dashed line), which shows that the A_0 mode is mostly excited. In addition, the dash-dotted line indicates the radiation direction predicted by the theory. The presence of the A_0 mode radiation shows the tuning capabilities of the array, while the good agreement of the radiation directions validates the theoretical approach to the array design. At 105 kHz and 280 kHz, the array shows the best directivity without coupling to other directions (Fig. 30a and Fig. 30d). Slight coupling between 150 kHz and 200 kHz was observed as manifested by the presence of contour of energy peaks in each other's directions, as shown in Fig. 30b and Fig. 30c.

A direct approach to identify radiation directionality of the array is to perform a polar scan around the array. The scan circle is selected with a diameter of 600 mm and 400 scan points, as illustrated in Fig. 31. The diameter size of the scan circle is

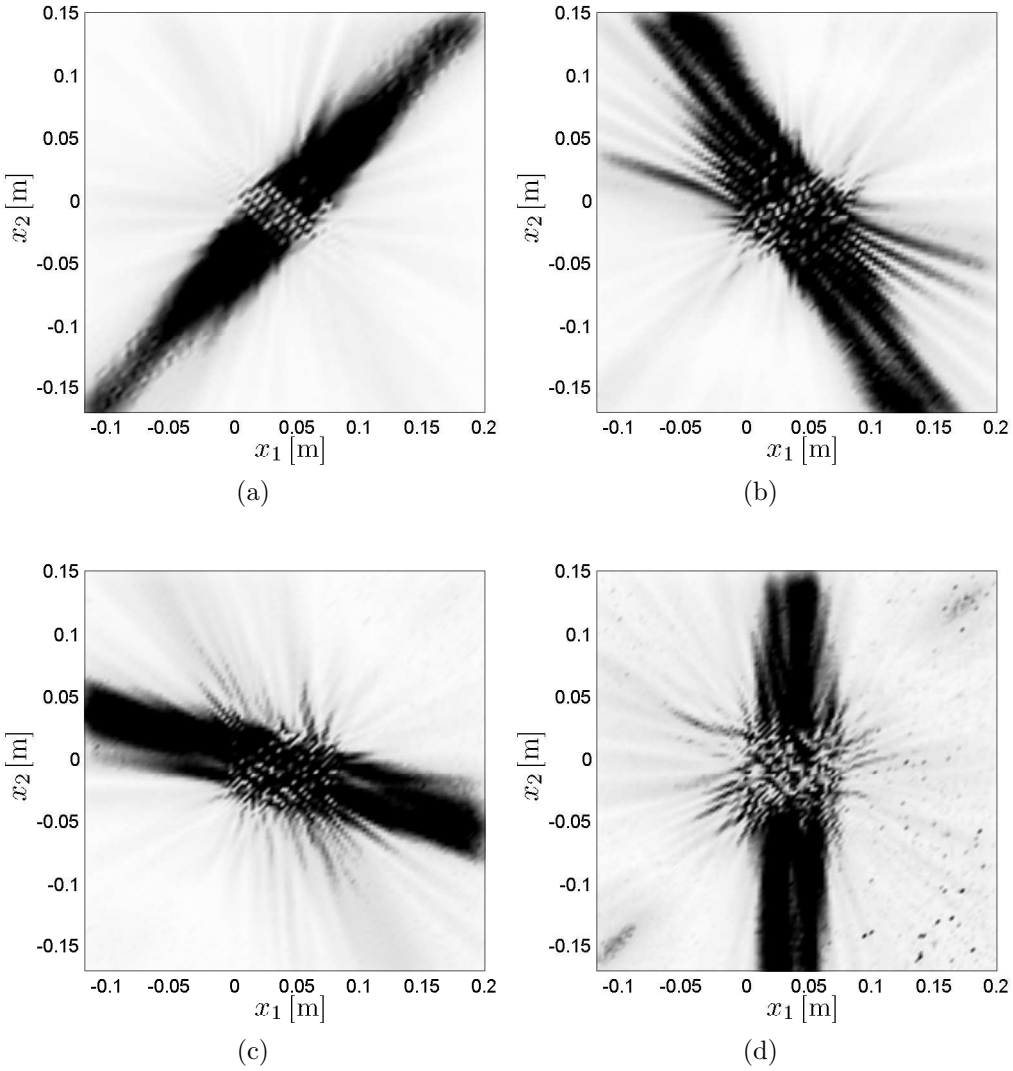

Figure 29: RMS radiation directionality of the array: (a) 105 kHz; (b) 150 kHz; (c) 200 kHz; (d) 280 kHz

chosen with the only requirement to be large enough to allow a definite beam forming; however, looking at Fig. 29, it is clear that the interference phenomena generated by the array actuation, form waves along definite directions already at 100 mm from the array center. The radiation strength is evaluated by calculating the recorded wavefield RMS values (Eq. (53)) at the corresponding scan point, which is associated with a radiation angle. This generates the polar plots presented in Fig. 32 for the four steering frequencies (105, 150, 200 and 280 kHz). Also the results in the current

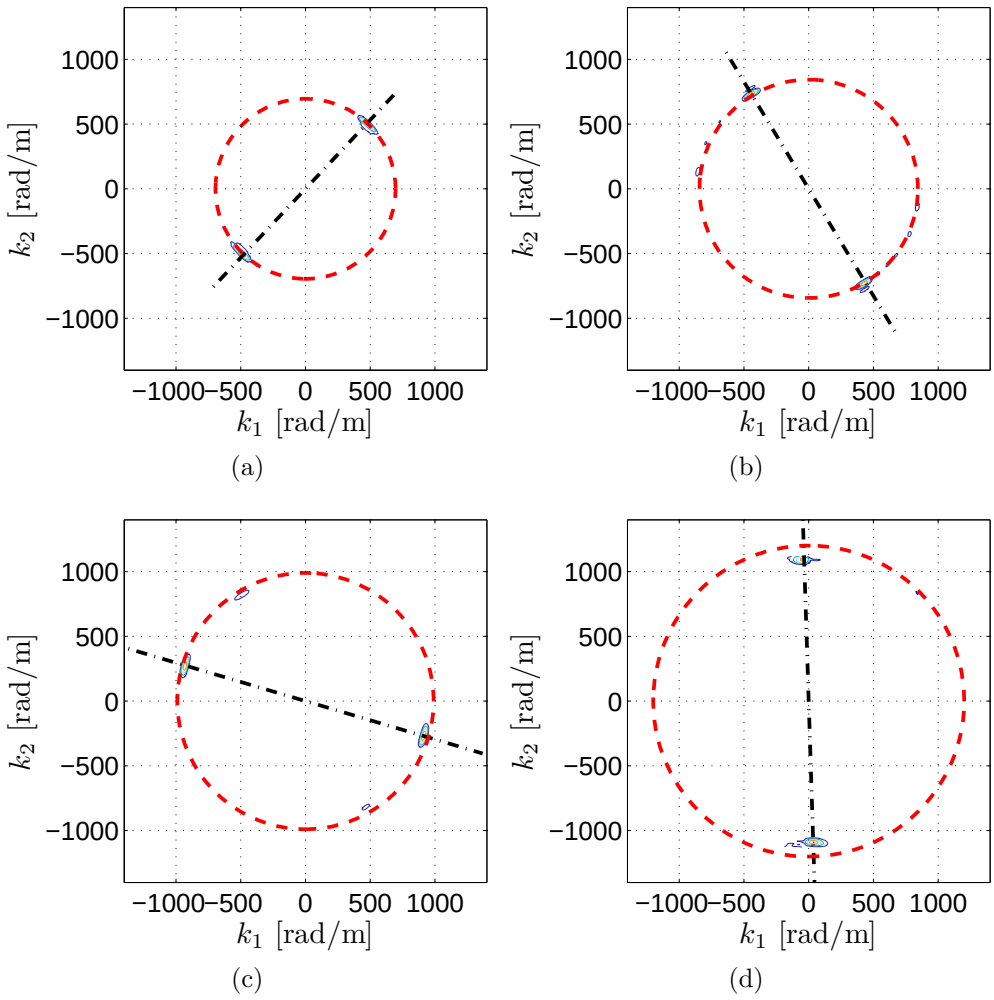

Figure 30: Radiation directionality of the array in wavenumber domain at: (a) 105 kHz; (b) 150 kHz; (c) 200 kHz; (d) 280 kHz

form establish a good correlation between numerical and experimental performance.

3.7 Application to Composite Plates

Till now, FSATs have been evaluated only for isotropic substrates applications. However this is not strictly necessary for the concept to be valid. In this section, the periodic array analyzed before is applied in a composite plate. The main issue related to the dispersion properties of composite materials is discussed first, then A_0 mode tuning is conducted and numerical simulations are performed to evaluate the performance.

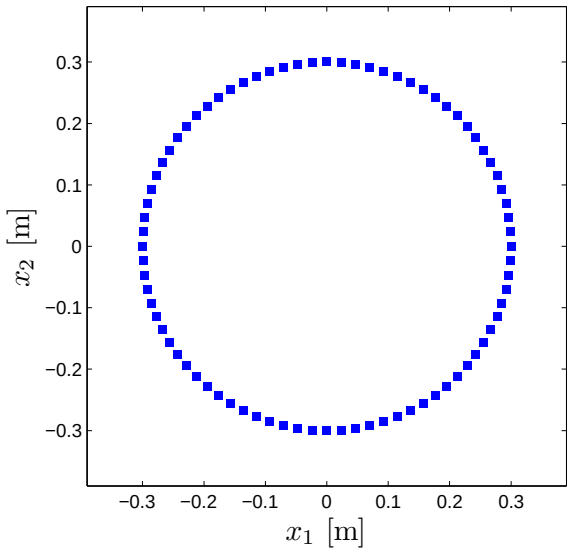

Figure 31: SLDV scan circle with the diameter of 600 mm and 400 scan points, and the array at its center (not shown).

3.7.1 Dispersion Analysis of Composites Plates

The application of the frequency-steering concept to composite materials requires knowledge of the dispersion properties, which are highly influenced by the lay-up sequence. Dispersion is evaluated through analytical and numerical procedures of the kind presented in [9]. The technique consists in the discretization of the cross section of the panel through standard finite element procedures. Wave propagation conditions are then imposed along a specified direction, which allows the estimation of the dispersion curves at different propagation angles; examples of dispersion curves for different composite lay-ups, for a propagation angle of 0 deg, are presented in Fig. 33, as obtained through an in-house code implementing the approach of [9]. The material properties and the lay-ups of the various cases are listed in Table 3 and in 4 respectively.

To appreciate the anisotropy of wave propagation in composite panels, it is better to show the dispersion relations computed at a fixed frequency and to observe how the wavenumbers, corresponding to different wave modes, change, varying the direction of propagation (Fig. 34). The iso-frequency dispersion relations, corresponding to the

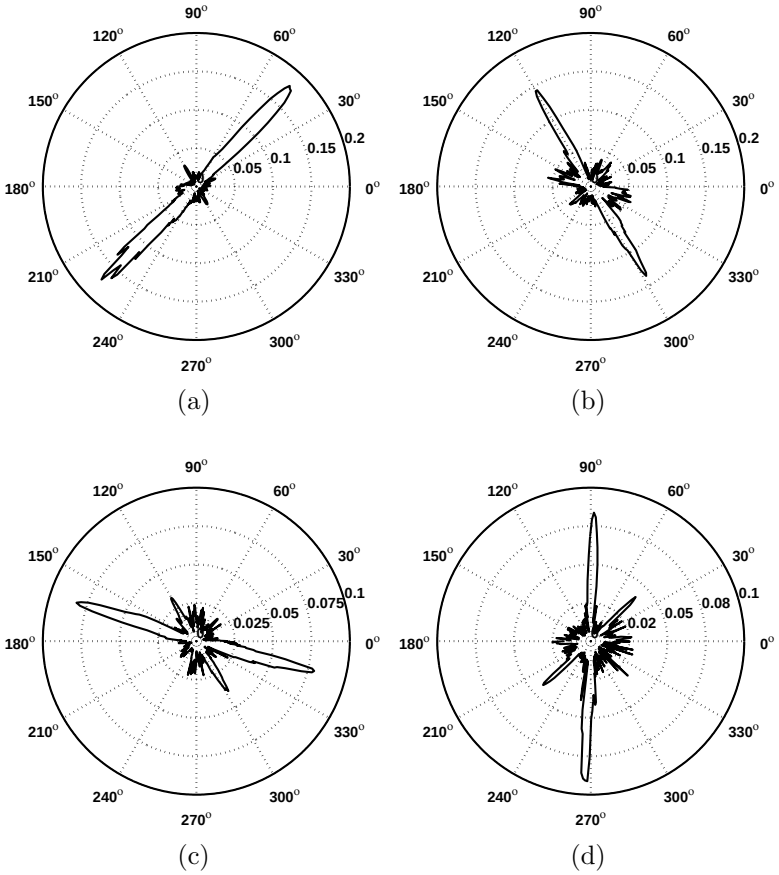

Figure 32: Circle scan of RMS radiation directionality of the array at: (a) 105 kHz; (b) 150 kHz; (c) 200 kHz; (d) 280 kHz

various wave modes, are computed at the dimensionless frequency $\omega h/c_{\mathrm{T}} = 4$, where h is the plate thickness, and c_T is the transverse (in-plane shear) wave velocity in the lamina, defined as $c_{\mathrm{T}} = \sqrt{G_{12}/\rho}$. The results show that the dispersion behavior becomes quite complex in particular for S_0 and SH_0 mode, which are clearly characterized by a strong anisotropy. This suggests that array design for frequency-based steering and tuning of these modes may be quite challenging.

The design procedure for such a case follows the same process explained for isotropic materials, whereby the directivity function provided by the array needs to match the dispersion curves through intersection of the peak values at selected directions. The results of Fig. 34 also show however that the A_0 mode is typically almost

circular, behaving, therefore, similarly to an isotropic mode. Given the practical relevance of A_0 generation for structural integrity evaluation, the array design proposed for isotropic materials can be easily modified to match the dispersion properties of the composite panel as discussed in the following section. Future work will investigate the tuning requirements for other modes, such as S_0 and SH_0, for directional guided wave generation in composites.

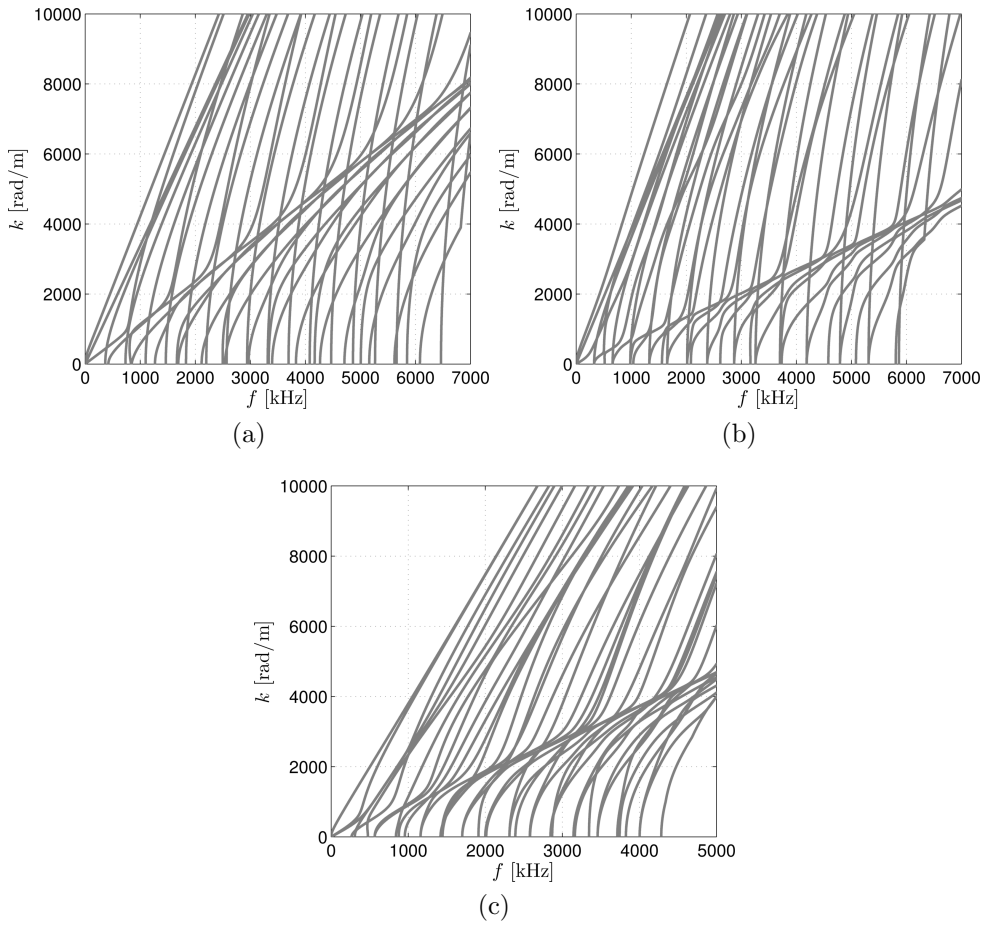

Figure 33: Composite panels dispersion curves (0 deg propagation angle): (a) Glass fiber S2 $[0_8]$ lay-up sequence; (b) Carbon fiber/epoxy T700/SE84HT $[0_2/+90_2]$ lay-up sequence; (c) Graphite/epoxy AS4/3502 $[+45_6/-45_6]_s$ lay-up sequence.

3.7.2 Array Design for A_0 Tuning

We considered an unidirectional composite panel with dimensions of 450 mm×450 mm×1.84 mm featuring 8 glass fiber S2 layers arranged according to the $[0_8]$ lay-up

Table 3: Material properties of considered composite plates

Material	E_{11} [MPa]	E_{22} [MPa]	E_{33} [MPa]	G_{12} [MPa]	G_{23} [MPa]	G_{13} [MPa]	ν_{12} [–]	ν_{13} [–]	ν_{23} [–]	ρ [kg/m^3]
glass fiber S2	45760	13600	13600	5700	3000	4000	0.257	0.257	0.3	1650
T700/SE84HT	131100	8000	8000	4230	3077	4230	0.337	0.337	0.3	1560
AS4/3502	131000	11300	11300	5970	3750	5970	0.3	0.3	0.34	1578

Table 4: Lay-ups of considered composite plates

Specimen	Stacking sequence	Dimension
glass fiber S2	$[0_8]$	450mm×450mm×1.84mm
T700/SE84HT	$[0_2/+90_2]$	450mm×450mm×2.3mm
AS4/3502	$[+45_6/-45_6]_s$	450mm×450mm×3mm

sequence. As indicated above, the difference compared with the isotropic plate case is that the dispersion relation is no longer circular due to the presence of material anisotropy. Fig. 34a shows the dispersion relations at 110kHz for the considered composite panel; at this frequency, A_0, S_0 and SH_0 modes are present. The A_0 mode steering frequencies of the array can still be identified by following similar procedures outlined in Section 3.4. Figure 35a shows the intersection of the dispersion relation of the A_0 mode with the maxima of the array force distribution in the wavenumber domain, which occurs at four steering frequencies 110, 145, 190 and 230kHz. The simulation of the panel response excited by the array was performed through an Abaqus finite element model of the layered panel. The model counted of C3D8R 8 nodes linear brick elements with reduced integration, with a row of elements for each layer through the thickness of the panel. The action of the array is simulated placing out–of–plane concentrated forces at the nodes where the array elements are supposed to be. The time integration is performed by an explicit solver. The material properties of the composite panel are listed in Table 3. The array shows similar radiation properties as those in the isotropic case. As an example, Fig. 35b presents the array radiation pattern at 110kHz in terms of out-of-plane displacements.

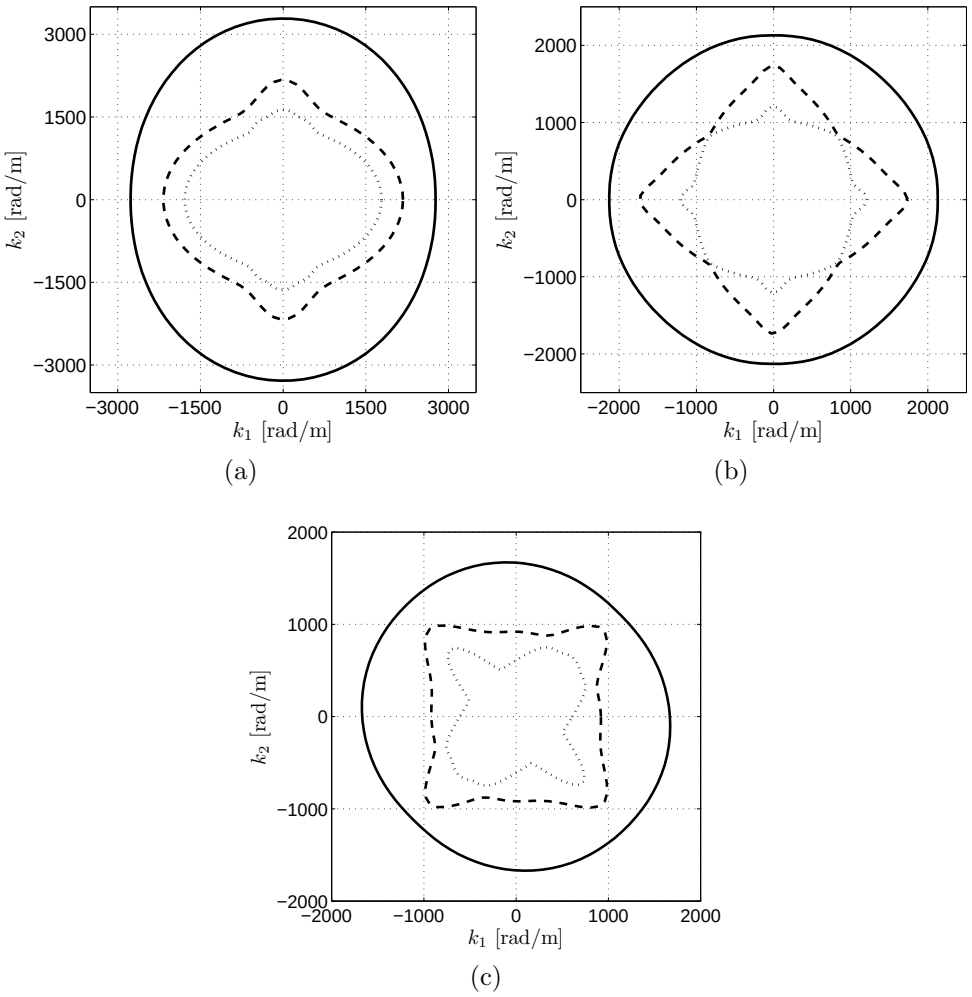

Figure 34: Composite panels dispersion relations at $\omega h/c_{\mathrm{T}} = 4$: A_0 solid line, SH_0 dashed line and S_0 dotted line. (a) Glass fiber S2 $[0_8]$ lay-up sequence; (b) Carbon fiber/epoxy T700/SE84HT $[0_2/+90_2]$ lay-up sequence; (c) Graphite/epoxy AS4/3502 $[+45_6/-45_6]_{\mathrm{s}}$ lay-up sequence.

3.8 Conclusions

In this chapter, an FSAT with the configuration of a quadrilateral periodic array and its directivity have been presented. The FSAT array is characterized by 4 beam steering directions associated to 4 distinct frequencies. Wave mode tuning has been discussed. Numerical predictions are in good agreement with experimental results, validating the concept of frequency–dependent directionality. At the end, the FSAT array application has been extended to composite panels through an FE simulation;

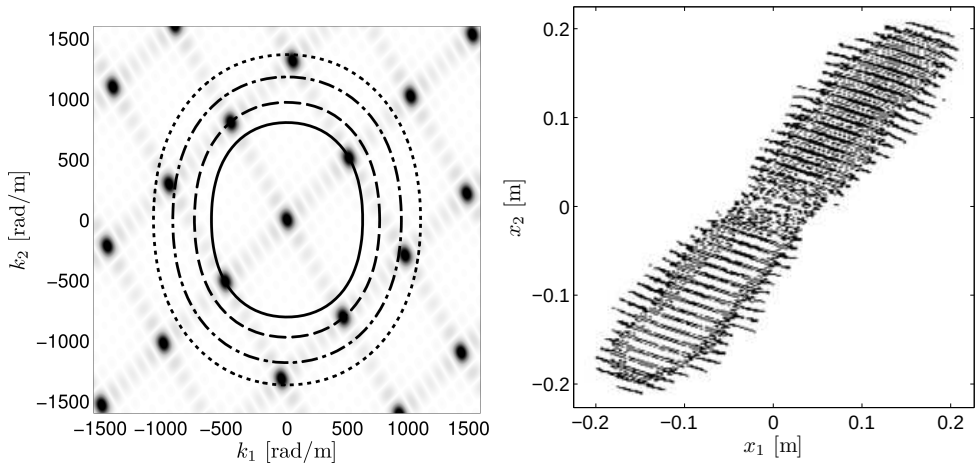

Figure 35: Simulation results of the quadrilateral array on the composite panel: (a) force distribution and A_0 mode dispersion relation at: 110 kHz solid line, 145 kHz dashed line, 190 kHz dashed dotted line, 230 kHz dotted line; (b) out-of-plane displacement pattern when excited by the array at 110 kHz.

the obtained numerical results confirm the FSATs effectiveness also for applications on non–isotropic substrates. However, the FSAT array directivity is quite limited for effective SHM applications. In the next chapter, the WS–FSAT configuration is presented, featuring an improved directivity, suitable for directional wave actuation and sensing.

CHAPTER IV

WAVENUMBER SPIRAL FREQUENCY STEERABLE ACOUSTIC TRANSDUCER

4.1 Overview

The FSAT array of Chapter 3 is characterized by four frequency values and four corresponding directions, which limits its potential use for directional actuation and sensing. This motivates the investigation of new FSAT designs with continuous, or quasi–continuous, frequency–directional capabilities.

This chapter presents a transducer geometry, which features a spiral distribution of active material in the wavenumber domain. The Wavenumber Spiral FSAT (WS–FSAT) is characterized by a unique relationship between frequency and direction of generation and sensing, resulting in an excellent candidate for effective structural health interrogations. The proposed device represents a departure from spiral-shaped transducer configurations proposed in literature for SHM [89] and other applications [33, 58, 74, 21] since the spiral qualification of the FSAT refers to its wavenumber representation and not to the actual shape in the spatial domain. Numerical analysis in actuation and preliminary experimental validation of the WS–FSAT are also discussed.

4.2 Wavenumber definition of the WS–FSAT and corresponding spatial shape

The frequency-dependent directivity of Eq. (17) suggests the possibility of designing the material distribution for desired directionality at specified frequencies. One strategy is to obtain a directionality pattern characterized by a unique relation between frequency of maximum sensitivity and direction of wave propagation. Based on the

discussions above, this may be achieved by specifying the directivity of the transducer as a function of the wave vector $\boldsymbol{k}_0(\omega)$, to then obtain the corresponding spatial distribution of the active material through an inverse FT in space (Eq. (18)). A desired directivity distribution features a single lobe at angles which vary with frequency and associated wave vector of the propagating wave. This corresponds to a directivity function $\mathcal{D}$ with maxima defining a spiral in the wavenumber domain. A schematic of the desired wavenumber directivity is presented in Fig. 36, which shows the desired location of the directivity maxima tracing a spiral in wavenumber space. The spiral shape allows for iso-frequency circles corresponding to a given wavenumber to intersect a single directivity maximum, and therefore to identify a single direction for the given wave vector. In the schematic of Fig. 36, intersections with 3 circles are shown to illustrate how increasing wavenumbers, and therefore frequencies, corrrespond to transducer sensitivities at increasing angles of wave direction. Such wavenumber values are associated with frequencies of maximum transducer directivity through the dispersion relation of the medium.

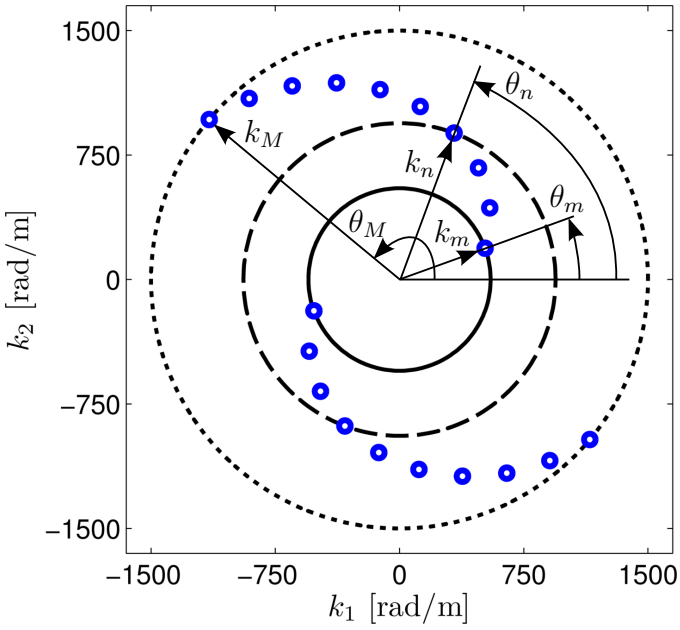

Figure 36: Schematic of spiral directivity in the wavenumber domain.

The spiral directivity function may be expressed as follows:

$$\mathcal{D}(\boldsymbol{k}_0(\omega),\theta) = -j\frac{a}{N}\sum_{n=1}^{N}\left[\frac{J_1\left(a\left|\boldsymbol{k}_0-\boldsymbol{k}_n\right|\right)}{a\left|\boldsymbol{k}_0-\boldsymbol{k}_n\right|} - \frac{J_1\left(a\left|\boldsymbol{k}_0+\boldsymbol{k}_n\right|\right)}{a\left|\boldsymbol{k}_0+\boldsymbol{k}_n\right|}\right] \tag{54}$$

where a is the patch radius in spatial domain, $J_1(x)$ is the first order Bessel function and $\boldsymbol{k}_n$ denotes the wave vector corresponding to the angle θ_n at which the n-th maximum of the spiral is located (Fig. 36), and where a corresponding directional lobe occurs. The location of $\boldsymbol{k}_n$ as a function of θ_n is given by:

$$\boldsymbol{k}_n(\theta_n) = [(k_M - k_m)\frac{\theta_n-\theta_m}{\theta_M-\theta_m} + k_m](\cos\theta_n\boldsymbol{i}_1 + \sin\theta_n\boldsymbol{i}_2) \tag{55}$$

which is the shape of an Archimedean spiral [78] defined in terms of minimum and maximum values of the wave vector amplitudes k_m and k_M, which in turn correspond to maximum directivities occurring respectively at angles $\theta = \theta_m$ and $\theta = \theta_M$ (Fig. 36). These bounds on the wave vector's amplitude are associated with frequency limits which essentially define the bandwidth of the transducer.

The spatial distribution corresponding to Eq. (54) is obtained using Eq. (18), which leads to a convenient analytical evaluation of the shape of the WS–FSAT. The sum of two Bessel functions in Eq. (54) is introduced to ensure that the corresponding inverse FT leads to a real valued function $f(\boldsymbol{x})$. The spatial distribution of the piezoelectric material is given by the following expression:

$$f(\boldsymbol{x}) = \frac{1}{N}\text{rect}\left(\frac{|\boldsymbol{x}|}{a}\right)\sum_{n=1}^{N}\sin(\boldsymbol{k}_n\cdot\boldsymbol{x}) \tag{56}$$

which is obtained by evaluating the inverse FT of Eq. (54) analytically.

As a way of an example, Figure 37(a) shows the directivity of a spiral with preferred directions $N = 22$, with $\theta_m = 0$, $\theta_M = 120^o$, $k_m = 550$ rad/m and $k_M = 1500$ rad/m. The spiral is defined by a discrete sequence of angular values whose spacing is selected to maintain constant arc-lengths along the spiral. This leads to a regular spacing of the discrete frequency values corresponding to the directions θ_n used for

the definition of the spiral. The corresponding spatial distribution for a radius of the patch equal to $a = 5$ cm is shown in Fig. 37(b), where the gray background corresponds to a value of 0, the dark regions are associated with negative values, and the light regions define positive polarization. The design of Fig. 37(b) is denoted in the remainder of the chapter as 'transducer (a)'.

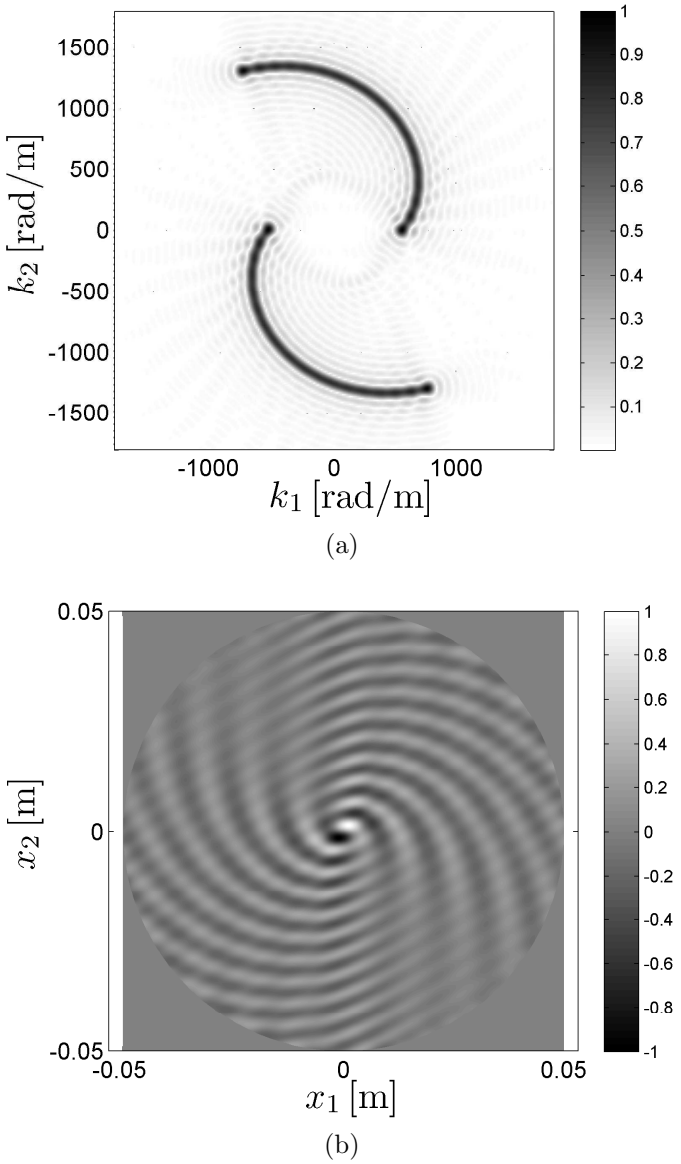

Figure 37: Transducer (a): spiral directivity function, $|\mathcal{D}(\boldsymbol{k}_0(\omega), \theta)|$ (a), and corresponding spatial distribution $f(\boldsymbol{x})$ (Eq. (56)) (b).

Figure 38 presents four directivities for four wavenumber values $k_n(\theta_n)$ and associated directions θ_n. These directivities are computed by evaluating the directivity function in Eq. (54) for the given wavenumber $k_n(\theta_n)$, i.e. $\mathcal{D}(k_0(\omega) = k_n(\theta_n), \theta)$.

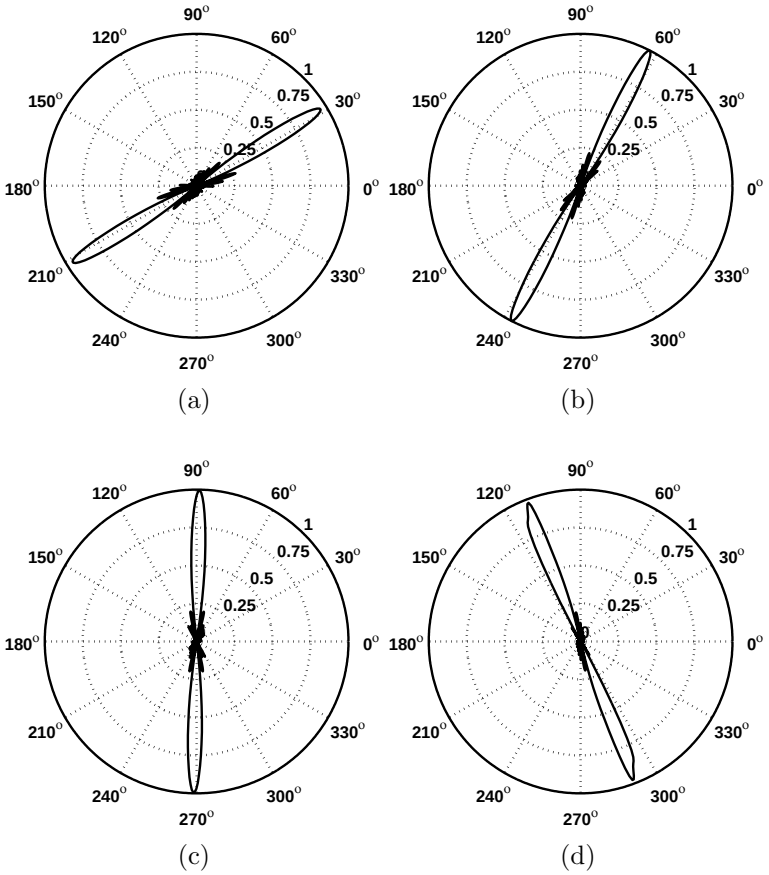

Figure 38: Directivity curves $\mathcal{D}(k_0(\omega) = k_n(\theta_n), \theta)$: (a) $n = 5$, $\theta_n = 31.6$ deg; (b) $n = 10$, $\theta_n = 62.9$ deg; (c) $n = 15$, $\theta_n = 88.9$ deg; (d) $n = 20$, $\theta_n = 111.6$ deg.

The spatial distribution described by Eq. (56) is practically unfeasible as it requires grading of the material or of the polarization, which is not physically possible. A simple strategy to overcome this involves the application of a thresholding procedure which transform $f(\boldsymbol{x})$ in a constant-valued function distributed over the considered domain. A tolerance value ε is introduced as a percentage of the maximum of $f(\boldsymbol{x})$, so that the final spatial distribution function can be described as follows:

$$\bar{f}(\boldsymbol{x}) = \begin{cases} 1, & f(\boldsymbol{x}) \geq \varepsilon \\ 0, & f(\boldsymbol{x}) < |\varepsilon| \\ -1, & f(\boldsymbol{x}) \leq -\varepsilon \end{cases} \tag{57}$$

The design corresponding to a tolerance level of $\varepsilon = 15\%$ of the maximum of $f(\boldsymbol{x})$, is presented in Fig. 39(b), which shows areas in black and white corresponding respectively to negatively and positively polarized regions. This configuration, referred to as 'transducer $(b)'$, has a reduced radius $a = 2.5$ cm in order to reduce the overall dimensions of the transducer. The corresponding directivity is estimated through the numerical evaluation of the associated FT and it is shown in Fig. 39(a). The thresholding procedure along with the reduction of the radius generally introduce side lobes, which are clearly visible in Fig. 39. However, of note is the fact that the spiral distribution in the wavenumber domain is largely maintained, so that the directional properties of the transducer are conserved. In general, transducer (b) exhibits reduced directional performance compared to transducer (a), which is characterized by wavenumber maxima located along a narrow spiral. This corresponds to a better filtering resolution, which is important for a precise and focused directionality. The spiral for transducer (b) is wider and it is characterized by evident side lobes. The performance of the large, non-thresholded transducer (transducer (a)) is directly compared with that of the smaller thresholded one (transducer (b)) in Fig. 40, which shows a cross section of the directivity functions at an angle $\theta = 45^o$, i.e. $|\mathcal{D}(\boldsymbol{k}_0(\omega), \theta = 45^o)|$.

4.3 WS–FSAT design for guided wave mode tuning

The wavenumber filtering properties of the WS–FSAT can be converted to frequency through the dispersion relations of the underlying medium. The case of Lamb waves in isotropic plates is here considered.

In this section, the transducers are designed to operate in a frequency range where

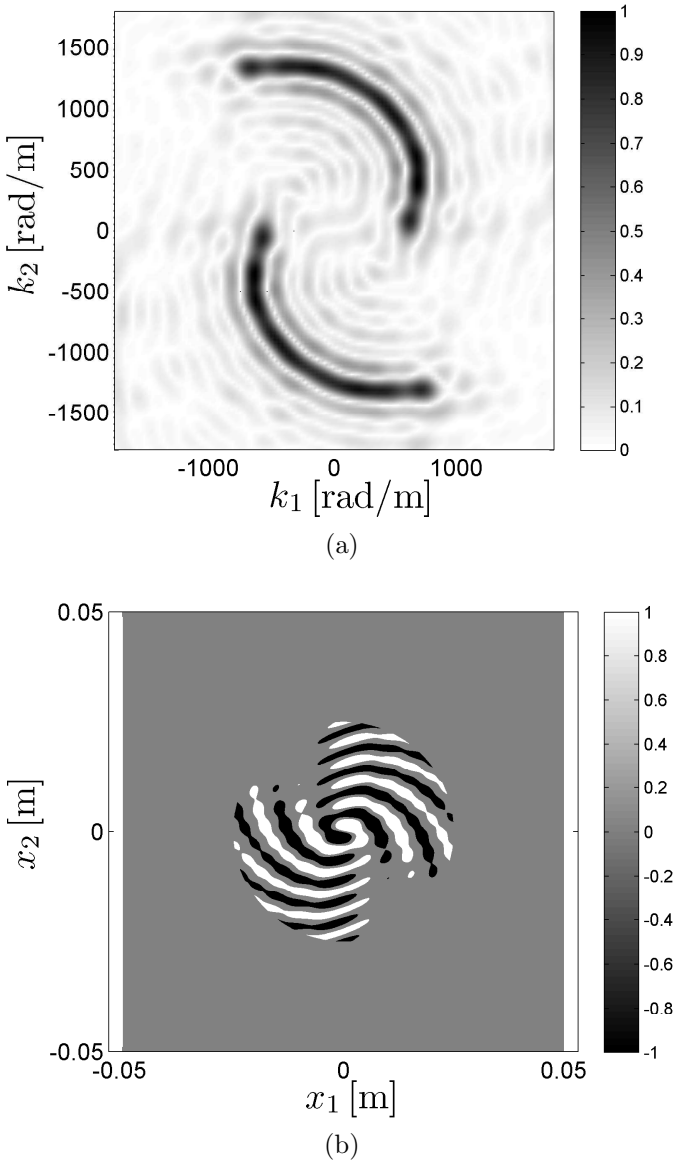

Figure 39: Transducer (b): spiral directivity function, $|\mathcal{D}(\boldsymbol{k}_0(\omega), \theta)|$ (a), and corresponding spatial distribution $\bar{f}(\boldsymbol{x})$ (Eq. (57)) (b).

wave propagation is the superposition of the first anti-symmetric A_0 and symmetric S_0 Lamb wave modes, i.e. for frequencies below the A_1 mode cut-off. Figure 41 shows the dispersion relation for an aluminum plate with thickness equal to 0.75 mm, which is used for all the studies presented herein. Specifically, the transducers are tuned to the A_0 mode frequency/wavenumber range, although a similar frequency/wavenumber mapping procedure may be followed for tuning the device to

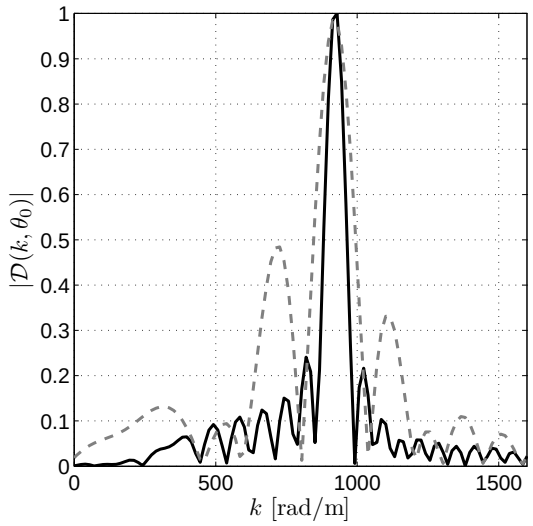

Figure 40: Transducers directivity function, $|\mathcal{D}(k, \theta_0)|$, along direction $\theta_0 = \pi/4$; transducer (a) black solid line, transducer (b) gray dashed line.

S_0. The frequency/wavenumber mapping based on the A_0 dispersion branch is illustrated in Fig. 41 which determines the WS–FSAT frequency and wavenumber range of operation.

For a selected wave mode, the combination of the wavenumber/direction mapping provided by the spiral design, and the wavenumber/frequency mapping defined by the considered dispersion branch leads to a frequency/direction correlation which directly determines the direction of a generated/sensed wave based on the frequency of the leading harmonic term excited/recorded by the transducer. An example of this correlation map based on the A_0 mode for the considered spiral FSAT is shown in Fig. 42.

The WS–FSAT may operate in generation mode to perform beam steering through a simple frequency sweep. This may enable the directional generation of Lamb waves for active interrogation of structural health. One of the potential applications of the FSAT in sensor mode is the localization of a broadband source based on the received frequency. This task relies on the operation of the WS–FSAT in a frequency range characterized by a unique relation between frequency of maximum sensitivity

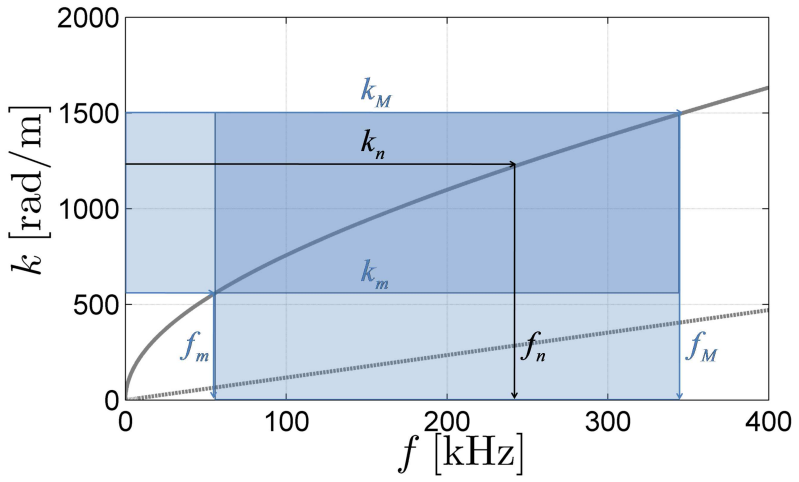

Figure 41: Dispersion relation for an Aluminum plate of 0.75 mm thickness (solid gray line A_0 mode, dashed gray line S_0 mode) and determination of the A_0 mode sensing frequency f_n correspondent to a wavenumber k_n. Similarly, sensor bandwidth $f_m - f_M$ from $k_m - k_M$. Sensor operating region in dark shaded area.

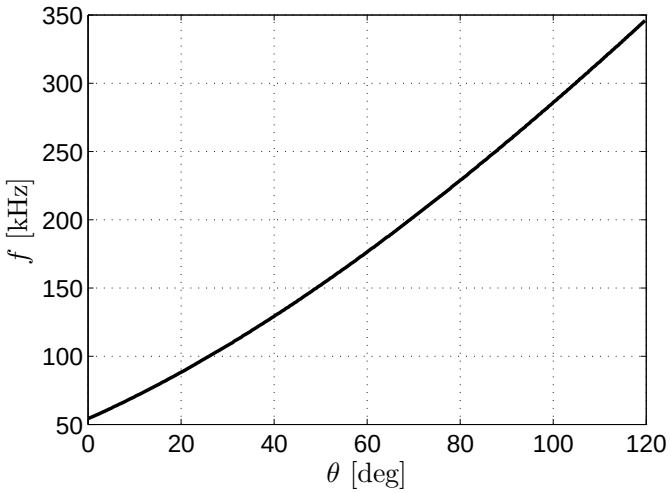

Figure 42: WS–FSAT θ-frequency correlation map based on A_0 mode dispersion branch.

and direction of wave propagation, so that ambiguities associated with multi-modal propagation can be avoided.

4.4 Numerical evaluation in actuation mode

The performance of the transducer (b) presented in Fig. 39(b) is here evaluated numerically. The choice of transducer (b), instead of transducer (a), is motivated by

the feasibility of its practical implementation, even if better performance would be expected by transducer (a). For this analysis the transducer is used in actuation mode and it is assumed to be installed on a 0.75 mm thick aluminum plate. The WS–FSAT is assumed to be driven at a specific frequency to generate guided waves along a specific direction. The adopted numerical procedure is the same of the one presented in Section 3.5.1 for the quadrilateral array, with the shape of the WS–FSAT approximated as the assembly of small discs with diameter of 0.8 mm (Fig. 43). The plate response due to the whole set of sources is computed as a superposition of the contributions of the individual discs, weighted with the correct value of the polarization.

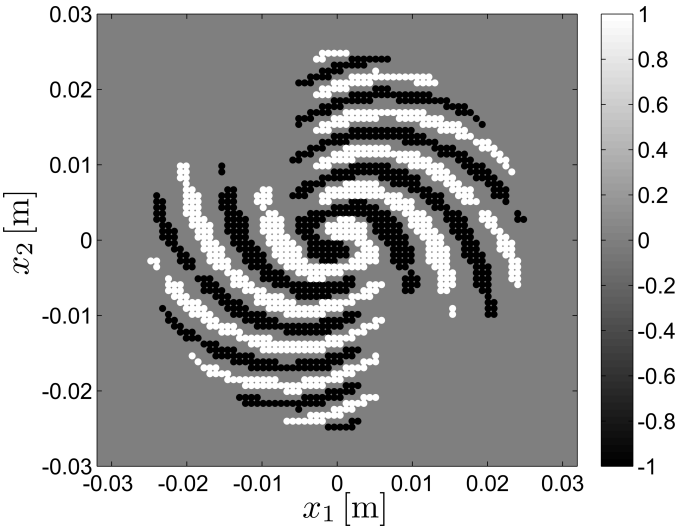

Figure 43: Transducer (b) discretized with a set of circular sources for numerical analysis. White discs have opposite polarization with respect to black discs.

The directions θ_n chosen for the guided wave generation are the same as those shown in Fig. 38. Figure 44 presents the plate out-of-plane response to harmonic excitations at frequencies f_n, determined via medium dispersion relation corresponding to $k_n(\theta_n)$. The plots clearly show the directional characteristics of radiation, and confirm the radiation directions predicted by the directivities of Fig. 38. Being these results obtained with transducer (b), they are a good starting point to state positively

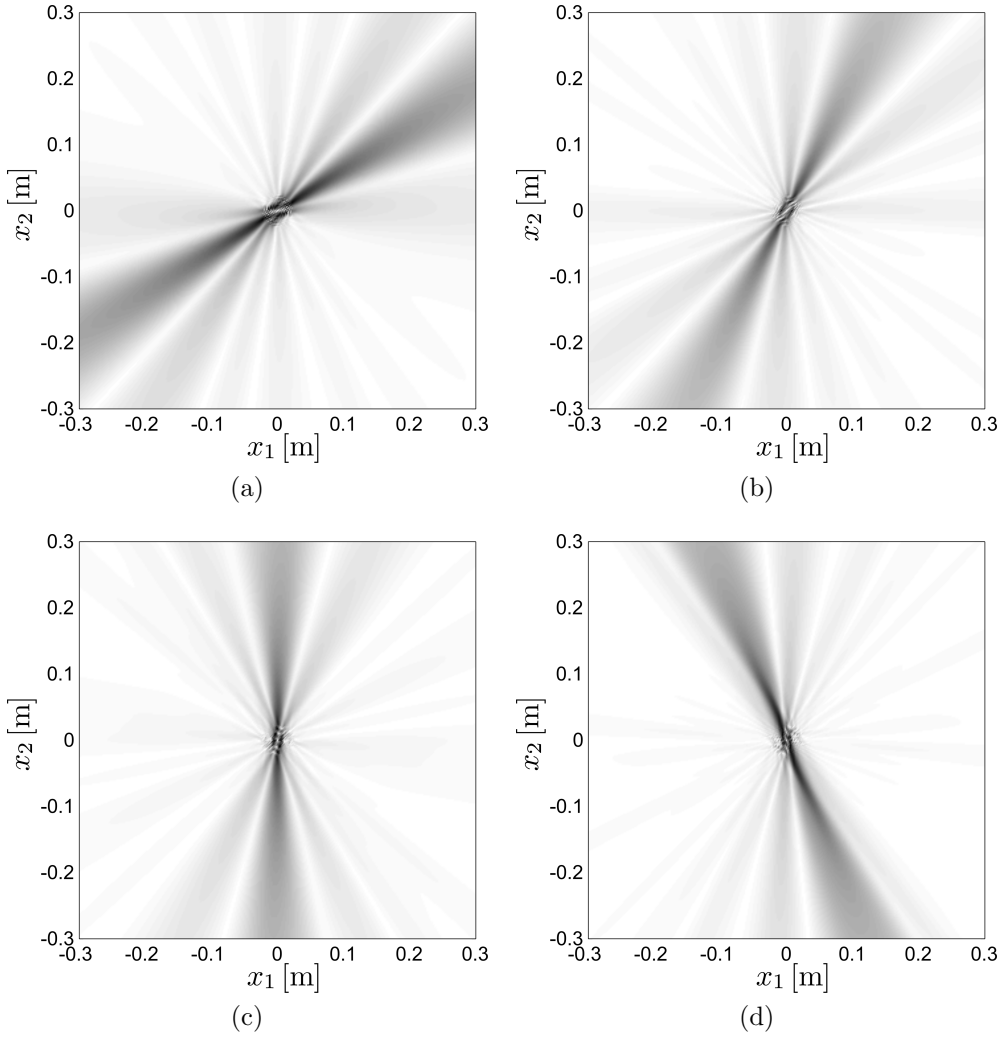

Figure 44: Aluminum plate response (0.75mm thick) for selected excitation frequencies f_n: $n = 5$, $f_n = 110.9$ kHz (a); $n = 10$, $f_n = 183.3$ kHz (b); $n = 15$, $f_n = 253.3$ kHz (c); $n = 20$, $f_n = 320.4$ kHz (d).

that the thresholding procedure does not compromise the directional properties of the WS–FSAT.

4.5 Experimental validation in sensing mode

Fabrication of a spiral FSAT piezoelectric transducer prototype and its testing are discussed in Chapter 5. Here, a preliminary experimental evaluation of the spiral design operating in sensing mode relies on measurements performed using a SLDV on a refined grid of points, out of which the desired WS–FSAT is sampled. This results

in a configuration whereby the sensor output is computed as the weighted sum of the response recorded at the selected measurement points, with weights defined by the spiral shape function (Eq. (56)) or its thresholded version (Eq. (57)). While different from the formulation based on piezoelectric sensing presented in Chapter 2, this approach allows great flexibility in testing various sensor shapes, without the need to manufacture physical sensors.

The objective of the tests is to evaluate the frequency content of the response recorded by the WS–FSAT array for different directions of incoming waves corresponding to a broadband input applied to the test structure. The intent is to simulate the performance of a sensor as a detection device able to estimate the location of a broadband input applied to the structure through frequency–based estimation of the direction of arrival (DOA). The filtering properties of the transducer as a function of DOA are compared with the theoretical predictions to validate the concept and demonstrate its effectiveness.

4.5.1 Set-up

Tests are performed on a 6061 aluminum plate of dimensions 1 m $\times$ 1 m $\times$ 0.75 mm. A broadband input is excited through a 5 mm PZT transducer bonded to the plate. The PZT is driven by a 900 V pulse generated by a Panametrics-NDT 5058PR pulser. The pulse is characterized by a 10%–90% rise time $t_{rise} \leq 40$ ns, whose bandwidth, estimated as BW $= 0.35/t_{rise} = 8.75$ MHz, is wide enough to excite the frequency range of interest (<500 kHz). The plate response is recorded over a 0.1 $\times$ 0.1 m area located at a distance of 0.28 m from the PZT disc. Wavefield measurements over the scan area are performed by repeating the excitation pulse over each scan point at a repetition rate of 20 Hz. The repetition rate signal is used as a trigger so that phase information is maintained at each measurement point, and the recorded wavefield appears as simultaneously captured in all points. This properly mimics the

response that would be recorded by a distributed sensor covering the scan area and evaluating the overall response of the plate over this region. The experimental set-up is shown in Fig. 45, while Fig. 46 presents the time history and the frequency content of plate response recorded at one of the scan points to illustrate the types of waveform considered during the experimental evaluation. Of note is the fact that a broadband impulse with as flat of a spectrum as possible is desired in order to provide a more robust frequency-based estimation of DOA. As PZT discs are not ideal broadband sources, yet are simple to operate and provide a repeatable input, refinements are needed in order to improve of the bandwidth of the excitation.

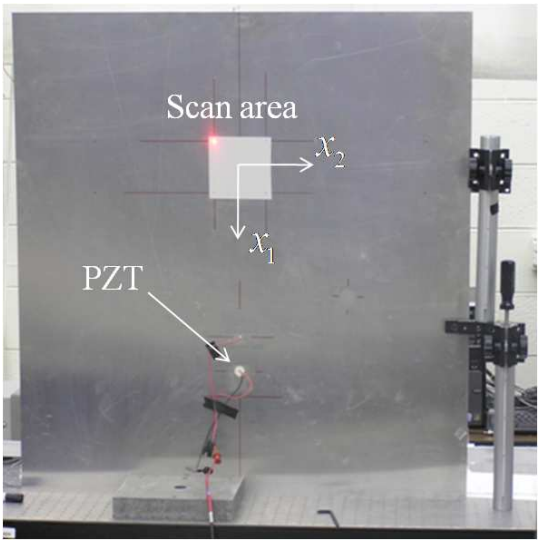

Figure 45: Experimental setup.

4.5.2 Sampling of measurement grid and evaluation of the spiral sensor response

The plate response is measured over a grid of $M \times M$ points, with $M = 128$. Sampling of the measurement points is simply performed by evaluating the sensor shape function $f(\boldsymbol{x}_j)$ at grid point $\boldsymbol{x}_j$. The measurement grid, and the sampled version based on the considered shape for the spiral sensor are shown in Fig. 47.

The response of the WS–FSAT array obtained from the sampling of the grid

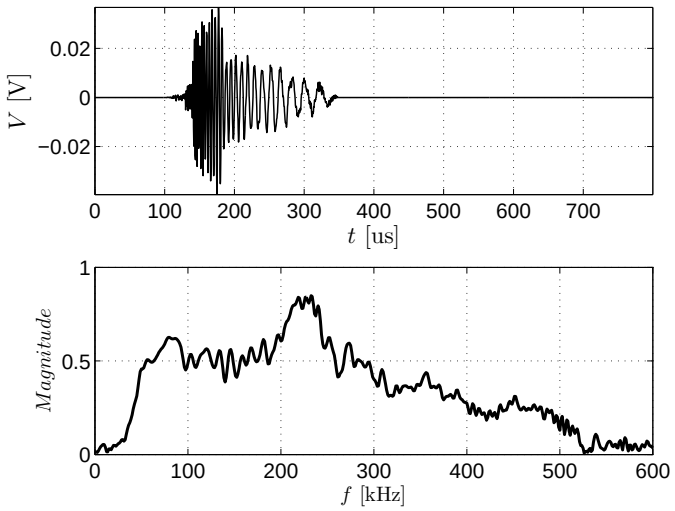

Figure 46: Time history and spectrum of a generic acquisition $u(\boldsymbol{x}_j, t)$.

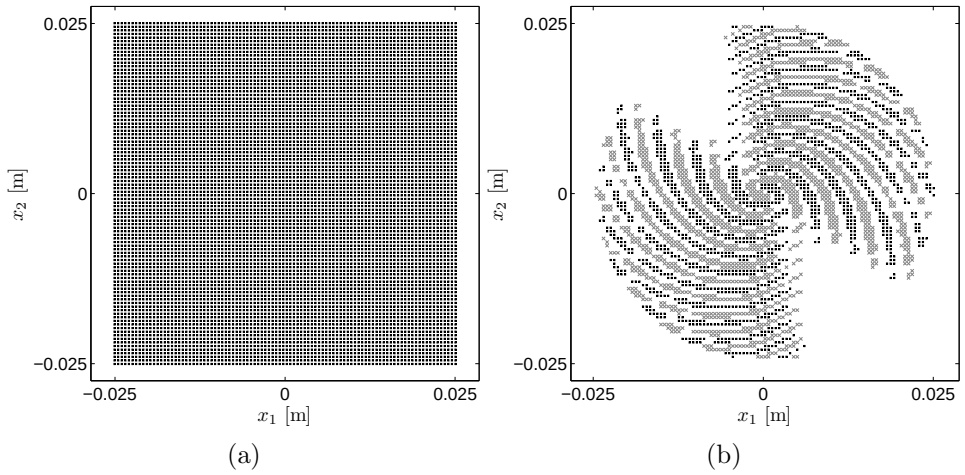

Figure 47: Measurement grid over scan area (a), and sampled grid corresponding to the spiral FSAT obtained through weighting according to Eq. 57 (black squares and gray crosses respectively denote locations x_j where $\bar{f}(\boldsymbol{x}_j) = 1$, and $\bar{f}(\boldsymbol{x}_j) = -1$ (b).

response is evaluated for different orientation of the sensor with respect to the broadband source. The PZT disc used for excitation is maintained in a fixed position, and the influence of source-sensor relative orientation is estimated by rotating the sampled WS–FSAT with respect to the PZT. This is conveniently achieved through a coordinate transformation for each grid point $\boldsymbol{x}_j$ based on the desired angle of relative rotation θ. A single set of experimental data thus allows the estimation of the directional dependence of the sensor output for a complete angular sweep.

Given relative angular position θ, the WS–FSAT response is computed through a discretized version of Eq. (18). If $u(\boldsymbol{x}_j, t)$ denotes the response measured by the SLDV at location $\boldsymbol{x}_j$, the spiral FSAT response is computed as:

$$q_a(t, \theta) = \sum_{j=1}^{M^2} f(\boldsymbol{x}_j, \theta)\, u(\boldsymbol{x}_j, t) \tag{58}$$

where the weights $f(\boldsymbol{x}_j, \theta)$ are calculated based on the analytical spiral FSAT expression:

$$f(\boldsymbol{x}_j, \theta) = \frac{1}{N} \text{rect}\left(\frac{|\boldsymbol{x}_j|}{a}\right) \sum_{n=1}^{N} \sin(\boldsymbol{k}_n(\theta_n - \theta) \cdot \boldsymbol{x}_j) \tag{59}$$

for the case of the non-thresholded sensor, while the response of the thresholded sensor can be similarly expressed as:

$$q_b(t, \theta) = \sum_{j=1}^{M^2} \bar{f}(\boldsymbol{x}_j, \theta)\, u(\boldsymbol{x}_j, t) \tag{60}$$

The response of the continuous sensor presented in Chapter 2 is here replaced by a weighted sum of the point responses $u(\boldsymbol{x}_j, t)$ recorded over the scan area. Subscripts "a" and "b" in Eq.s (58),(60) refer to the sensors design previously described, and denoted as transducer (a) and transducer (b). Of note is the fact that while the practical implementation of transducer (a) is not feasible, the evaluation of its performance through the considered approach and Eq. (58) allows considering it as a baseline against which the performance of thresholded designs of the kind of transducer (b) can be evaluated.

4.5.3 Spatial filtering & frequency dependent directionality

FSATs, as stated in Chapters 2 and 3, can be considered as spatial filters. The experiment described so far provides a nice example to visualize the concept. From the SLDV acquisition, three transducers signals have been synthesized: $q_a(t, \theta)$ and $q_b(t, \theta)$ according to Eqs. (58) and (60) respectively, for the case of $\theta = 50°$, and $q_R(t)$, a reference signal simulating the absence of any transducer, obtained simply as:

$$q_R(t) = \sum_{j=1}^{M^2} u(\boldsymbol{x}_j, t) \tag{61}$$

The Short Time Fourier Transform (STFT) [56] of these synthesized signals is presented in Fig. 48. For the reference signal, obviously, no filtering action is observed, as indicated by the wide range of frequencies present in the time–frequency map. The peak in the proximity of 230 kHz is due to the not–completely flat frequency content of the excitation. This is evident also in Fig. 46 in the spectrum of a generic acquisition point. The STFT allows to visualize wave dispersion. In Fig. 48(a), spectrogram peaks are distributed along an "hyperbole" like curve, which is associated by the group delay curve due to the different waves speed at various frequencies. In Fig. 48(b), the filtering effect of transducer (a) is clear, producing a signal q_a with a frequency content concentrated only around 150 kHz, as expected for $\theta = 50°$, looking at the θ-frequency correlation map of Fig. 42. In Fig. 48(c), similar considerations can be made for transducer (b); in addition, other than the main peak around 150 kHz, frequency side lobes are visible, caused by the inaccuracy introduced by thresholding.

Additional results are presented based on the estimation of the spectral content of the response recorded for increasing angles of DOAs. The considered angles and related results are reported in Table 5, which lists the theoretically expected frequencies of peak harmonic response compared with those estimated experimentally on the basis of the two considered sensor designs. The frequency peaks are derived from the wavenumber/frequency mapping based on the A_0 mode dispersion, estimated from the analytical evaluation of the dispersion relations for the considered aluminum plate. The comparisons show a very good agreement between expected and measured frequency peaks, and between actual and estimated DOA for both sensor designs. As expected the estimations based on the thresholded, smaller transducer (b) are less accurate, but can still be considered as sufficient for the direction determination of an incoming wave.

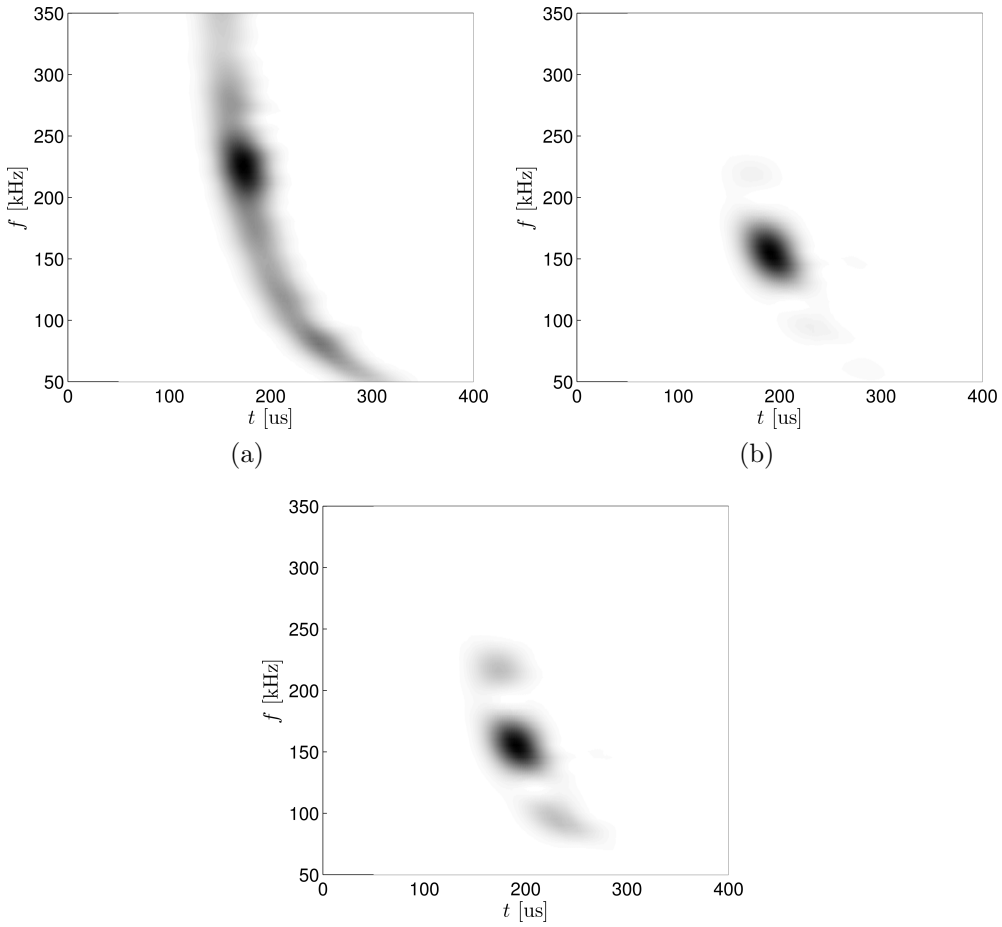

Figure 48: Spectrograms of synthesized spiral FSAT signals for $\theta = 50°$; reference signal, $q_R(t)$ (a), $q_a(t,\theta)$ (b), $q_b(t,\theta)$ (c).

The frequency filtering characteristics of the two sensors are compared in Fig. 49, which shows the frequency spectra corresponding to the estimated responses q_a and q_b for different values of the angle θ. The plots also show the expected frequency corresponding to the considered angle as a vertical dashed red line to provide a visual comparison of the accuracy of the predictions.

Results presented in Fig. 49 and Table 5 overall demonstrate the good performances of the sensors. The sensors filter the input signal quite sharply around the expected frequency. The DOAs detected by both sensors are very close to those expected. In particular, from the spectra of Fig. 49, one can observe that both sensors

Table 5: Actual vs estimated peak frequencies and angles of DOA for transducers (a) and (b).

Actual	f [kHz]	**70**	**108**	**152**	**202**	**257**	**315**
	θ [deg]	**10**	**30**	**50**	**70**	**90**	**110**
Estimated (transducer (a))	f [kHz]	74	112	158	209	254	311
	θ [deg]	12	32	52.5	72.6	89	108.5
Estimated (transducer (b))	f [kHz]	75	112	146	212	272	310
	θ [deg]	12.8	32	47.4	73.8	95.4	108.1

detect a main peak very similar to each other for all DOAs considered. The most evident difference is the presence of side lobes for transducer (b), as however expected looking at the directivities in Fig.s 37(a),39(a) and 40. The presented results validate the WS–FSAT concept and show that the thresholding strategy, as in the case of the previous numerical analysis in actuation, does not compromise the sensor effectiveness, even if it leads to a performance reduction. This is an important conclusion to be taken into account when investigating the practical implementation of a WS–FSAT device.

4.6 Conclusions

In this chapter, the design of an FSAT with continuous frequency dependent directionality is presented and evaluated numerically in actuation and experimentally in sensing. The transducer is characterized by a geometry whose wavenumber domain representation features maximum amplitudes located along a spiral. The resulting WS–FSAT leads to a quasi–continuous frequency–dependent directional performance. This is verified numerically in actuation. In sensing mode, the transducer acts as a spatial filter at frequencies which vary with the direction of the incoming wave. Testing is performed by synthesizing the transducers as an assembly of properly arranged points belonging to the measurement grid of a SLDV. The presented experimental results show how the WS–FSAT is capable of determining the direction of the incoming wave through the received frequency into a wavenumber value. The demonstrated

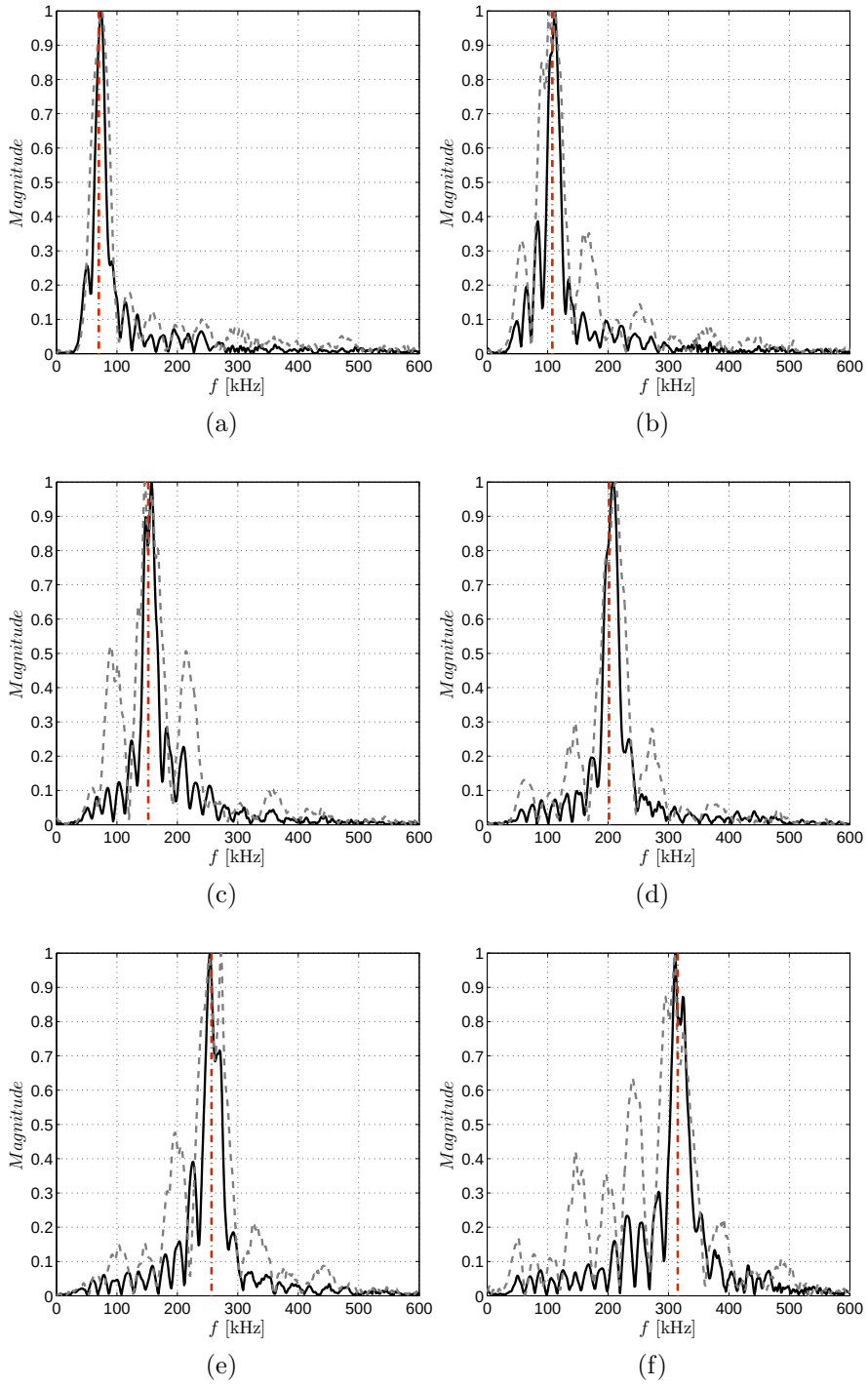

Figure 49: Comparison of spectra detected by the two spiral arrays at different angles θ: black solid line, transducer (a); gray dashed line, transducer (b); red vertical dot dashed line, expected peak frequency. (a) 10^o, (b) 30^o, (c) 50^o, (d) 70^o, (e) 90^o, (f) 110^o.

frequency-dependent directionality suggests how WS–FSATs may significantly facilitate the location of acoustic broadband events.

CHAPTER V

WS–FSAT PROTOTYPING AND TESTING

5.1 Overview

Chapter 4 presented the design of WS–FSAT and its frequency–dependent directionality characteristics.

This chapter illustrates the practical implementation of a WS–FSAT based on inkjet printing of the electrode patterns on a polyvinylidene fluoride (PVDF) substrate. Sensing performance of the produced prototype is evaluated experimentally in the presence of broadband acoustic sources. More precisely, the angular location of the sources is determined from the spectrum of the WS–FSAT acquired voltage signal. The successive implementation of a signal processing algorithm for the analysis of the output of the WS–FSAT provides the direct visualization of the source location over the area of interest. The algorithm allows for the estimation of source location through time delay evaluations. This is achieved by exploiting the concept of frequency warping [17].

5.2 Prototyping

As stated in Section 4.2, the feasible WS–FSAT design is the one considering a thresholding procedure applied to the analytical spatial distribution of active material obtained with Eq. (56). An example of feasible design is shown in Fig. 39(b). To simplify the manufacturing process, instead of realizing a spatial distribution of piezoelectric material, formed by separate areas with opposite polarization as implied in the previous chapter, an alternative, simpler solution has been implemented. An

equivalent sensor is manufactured with a continuous distribution of piezoelectric material, but with an electrode pattern reproducing the material distribution obtained after the thresholding procedure. In this case, the polarization of the active material is obviously the same in the entire sensor, but grouping the electrodes areas in two separate channels and considering the differential signal of the two, the overall effect of this manufacturing solution is the same of the previous one. This consideration is based on the observation that the voltage sensed by a piezoelectric sensor is the result of an integration over the portion that is covered by the electrodes. The prototype fabrication discussed in this section, is designed for sensing applications, because the piezoelectric substrate adopted, polyvinylidene fluoride (PVDF), generally does not provide enough actuation authority for wave generation [24].

5.2.1 WS–FSAT design

The WS–FSAT chosen for the practical realization is characterized by the following design parameters: $N = 22$, $\theta_m = 0$, $\theta_M = 180^o$, $k_m = 528$ rad/m and $k_M = 1509$ rad/m, which corresponds to a frequency bandwidth from 50 kHz to 350 kHz assuming the installation on a 0.82 mm thick aluminum plate. The radius of the patch is equal to $a = 2.5$ cm and the tolerance level is $\varepsilon = 8.2\%$, which is sufficient to assure well separated electrodes' areas. Figure 50 presents the electrode distribution of the considered WS–FSAT, corresponding to the two polarizations represented as black and white areas.

5.2.2 Inkjet fabrication

PVDF, whose material characteristics are listed in Table 6, represents an ideal substrate for the realization of FSATs suitable for sensing operation; in fact, its high flexibility allows to produce patches for installation also on curved surfaces, and its light weight is an undoubtable added value considering potential applications for aerospace structures. As it comes in thin sheets, it is fully compatible with inkjet

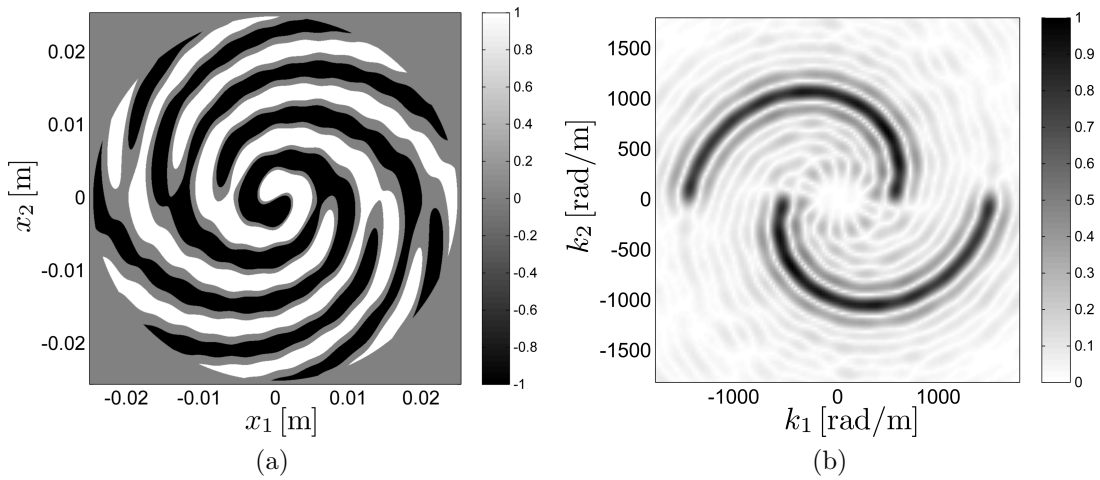

Figure 50: Adopted design for WS–FSAT prototyping: electrodes distribution $\bar{f}(\boldsymbol{x})$; white and black areas represent the two groups of electrodes (a), and corresponding directivity function, $|\mathcal{D}(\boldsymbol{k}_0(\omega), \theta)|$ (b).

printing, which provides an optimal choice for patterning electrodes with complicated shapes such as those involved in the spiral FSAT depicted in Fig. 50(a). The adopted fabrication approach consists in printing the electrodes' geometry as a thin polymer film on a metallized PVDF substrate and using the printed features as an etch resist mask for a subsequent metal etching step. The procedure is performed on a single side of the substrate, while the back side metallization provides the common ground electrical connection. A 110 um-thick PVDF film with a two-layer metallization (40 um Copper/15 um Nickel) is employed. The printer is a Microfab Jetlab II system shown in Fig. 51(a). An ultraviolet (UV) curable optical epoxy (Norland 89) proved to be a suitable ink, yielding highly reproducible features with 100 um resolution, which is sufficient for the present application. The printed image is a black and white bitmap representation of the electrodes' pattern (Fig. 52(a)) with size 625×625 pixels, which corresponds to a pixel spacing of 80 um for the printer, resulting in sufficient overlapping of adjacent ink drops. After printing the pattern with a stage velocity of 50 mm/sec, a 5-minute exposure to UV light provides adequate curing for the sample

(Fig. 52(b)). The obtained polymeric pattern provides sufficient coverage of underlaying regions for wet etching of the metal, which is performed through a 15% solution of Ferric Chloride ($FeCl_3$) in distilled water. The back side of the sample is protected to preserve its metallization. After etching, the sample appears as shown in Fig. 52(c). A few small imperfections are seen at some feature edges, but they were not found to affect electrical performance of the sensor. These imperfections are expected to be eliminated by further optimization of the printing process (pixel density, printing velocity, etc.). The polymer mask is finally stripped away with methylene chloride and methanol, leaving the desired electrodes' geometry visible in Fig. 52(d).

Table 6: PVDF material characteristics [66]

$c_{11}^E = 3.6110^9$ Pa	$c_{22}^E = 3.1310^9$ Pa	$c_{33}^E = 1.6310^9$ Pa
$c_{12}^E = 1.6110^9$ Pa	$c_{13}^E = 1.4210^9$ Pa	$c_{23}^E = 1.3110^9$ Pa
$c_{44}^E = 0.5510^9$ Pa	$c_{55}^E = 0.5910^9$ Pa	$c_{66}^E = 0.6910^9$ Pa
$\epsilon_0 = 8854 \times 10^{-12}$ F/m	$d_{15} = 27 \times 10^{-12}$ C/N	$d_{24} = 27 \times 10^{-12}$ C/N
$d_{31} = 25 \times 10^{-12}$ C/N	$d_{32} = 2 \times 10^{-12}$ C/N	$d_{33} = -33 \times 10^{-12}$ C/N
$\varepsilon_{11}^\sigma = 7.35\epsilon_0$	$\varepsilon_{22}^\sigma = 9.27\epsilon_0$	$\varepsilon_{33}^\sigma = 7.75\epsilon_0$

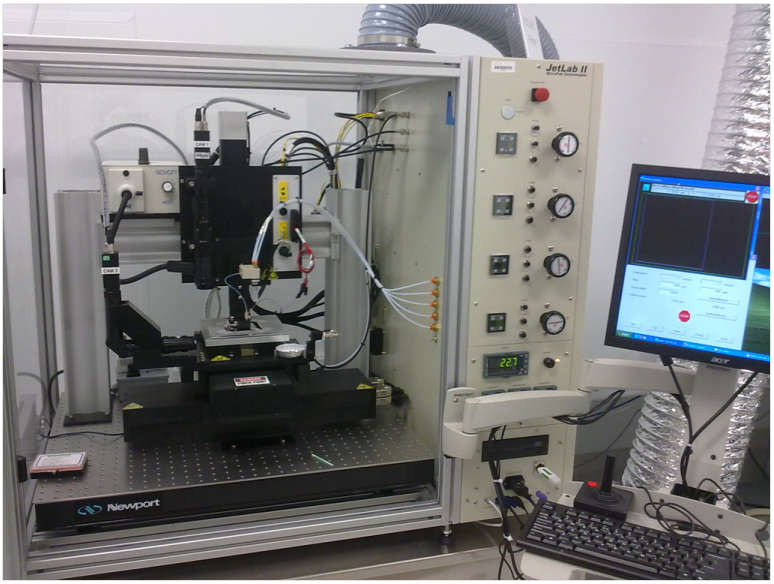

Figure 51: Microfab Jetlab printer.

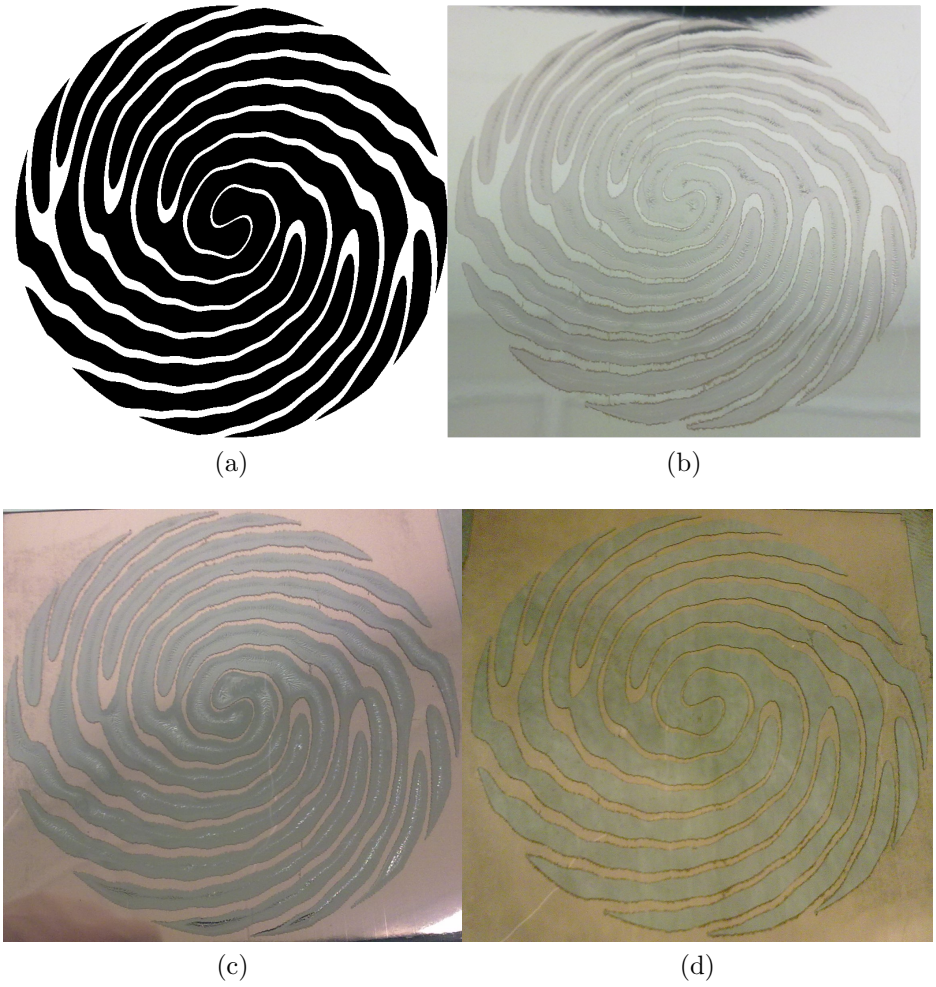

Figure 52: WS–FSAT prototyping steps: bitmap representation of electrodes pattern (a); printed ink pattern (b); metal etching (c); ink stripping (d).

The outlined fabrication process is fast and provides great flexibility in terms of the shapes that can be patterned. Moreover, the "mask & etch" approach ensures optimal performance of the electrodes, as they are realized with the original conductive coating provided by the PVDF vendor, while potential issues related to coverage uniformity are prevented, that could arise when patterning the electrodes with metallic ink directly on an unmetallized PVDF film. Finally, it is worth noting that this procedure could be extended to a number of different applications involving patterning of various materials.

5.3 Testing

Testing of the proposed transducer for angular localization of broadband acoustic sources is described in this section. The inspected structure is a 0.82 mm–thick aluminum plate of size 915 mm × 915 mm. The fabricated WS–FSAT is attached at the center of the plate through epoxy glue, as shown in Fig. 53(a). The detail of electrode areas connection is shown in Fig. 53(b): areas belonging to the two groups of electrodes have been connected together, bridging them with copper wires bonded with conductive epoxy. On the right side of the figure, it is possible to observe two wires which continue also beyond the picture. These are the wires of the two channels, which provide the output signals of the device.

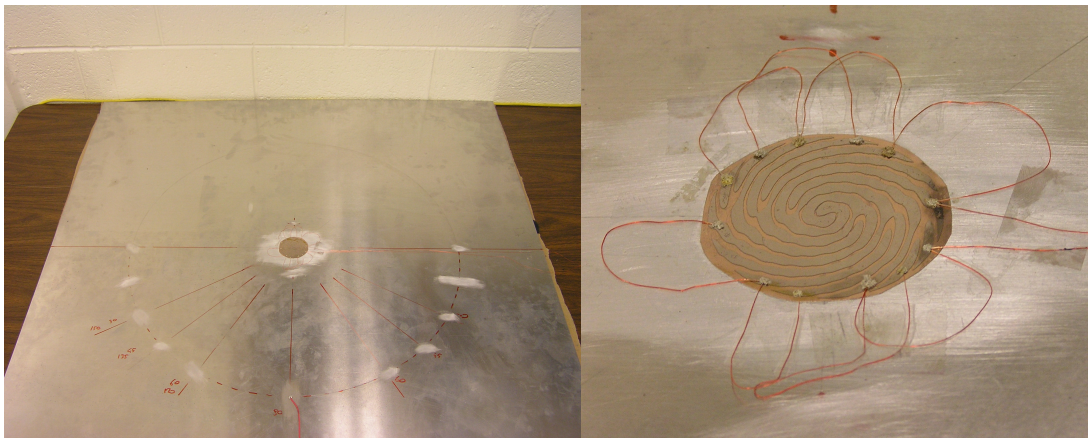

(a) (b)

Figure 53: WS–FSAT prototype installation on aluminum plate (a), and particular of electrodes' connection (b).

5.3.1 PVDF patch influence on wavefield

The spiral WS–FSAT prototype influence on an incoming wavefield is considered in this section, to verify the plane wave assumption made in Section 2.2.3. A 5 mm–diameter PZT disc has been placed 300 mm far from the WS–FSAT and excited with a tone burst centered at 160 kHz. The generated wavefield is recorded over an area enclosing the patch by a SLDV. The objective is to observe the interaction of the

PVDF patch with the wave propagation in the underlying aluminum substrate. Two subsequent snapshots of the wavefield across the sensor are presented in Fig. 54. It can be observed that for a source placed 300 mm away from the sensor, the plane wave front assumption of the incoming wave is respected. Moreover, even if the wave arrival on the sensor generates some reflections, these are of very low intensity compared to the incident wave. Similarly to what done in Section 3.6.1, the captured wavefield, $u_3(x_1, x_2, t)$, is transformed to the frequency/wavenumber domain to obtain $\hat{u}_3(k_1, k_2, \omega)$. The wavenumber content of the plate response at 160 kHz is illustrated in Fig. 55. The same observations made for the snapshots of Fig. 54 can be made also looking at this figure. In fact, the concentration of the response in a small area approximately centered in $k_1 = 0$ and $k_2 = 1000$ rad/m means an almost plane wave propagating in vertical direction. Hence, it is possible to conclude that the presence of the WS–FSAT does not alter significantly the wavefield, resulting in an almost inert sensing device.

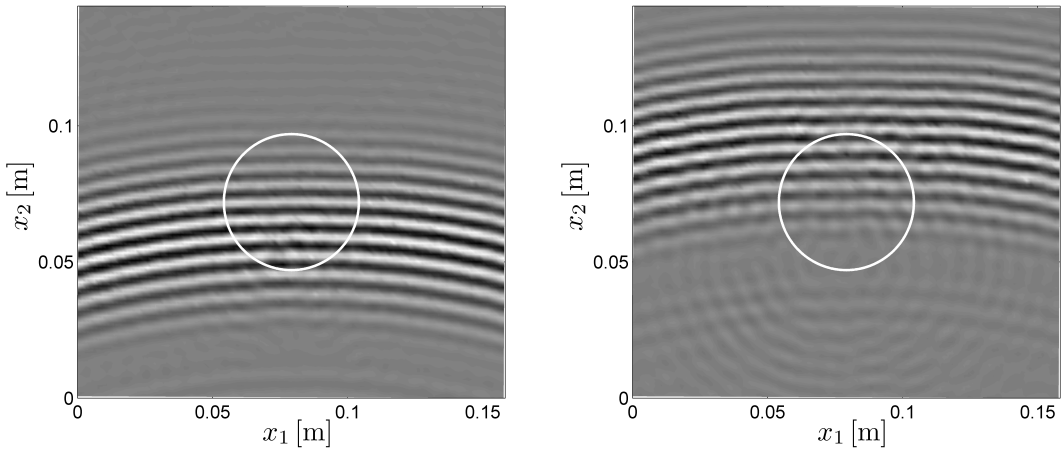

Figure 54: Incoming wavefield crossing the WS–FSAT prototype in two different time instants; earlier instant (a), and successive (b). Device dimensions highlighted by solid white line.

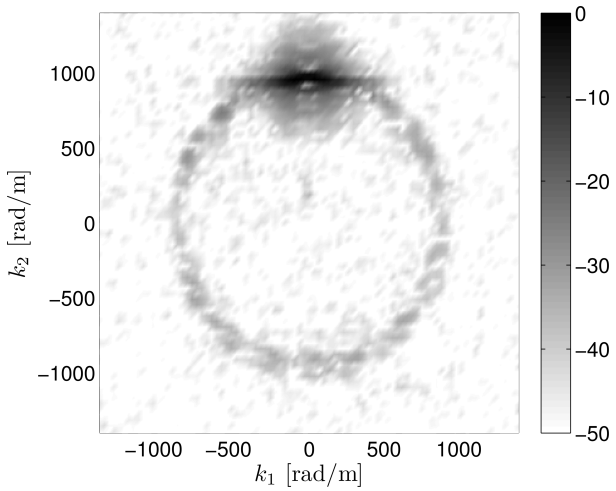

Figure 55: Wavenumber content of the plate response at 160 kHz (dB scale).

5.3.2 Acoustic source angular localization

The sensing performance of the device is tested for broadband acoustic source localization. Acoustic sources are represented by 5 mm–diameter PZT transducers driven by a broadband pulse excitation. The PZTs are attached at various locations of the plate through Sonotech shear couplant gel. Each PZT is excited once per time from a distance of 300 mm from the WS–FSAT center to emulate broadband acoustic events that the device is expected to detect. The differential voltage obtained by the two channels of the WS–FSAT is recorded by a Tektronix TDS2024 oscilloscope and then stored into a PC using a MATLAB graphical user interface (Fig. 56). Tests are performed for the angular positions shown in Fig. 56.

5.4 WS–FSAT sensor performance

In this section, the results of the testing described in Section 5.3.2 are presented. The directional sensing capability of the WS–FSAT is shown processing the signals acquired for each acoustic source position. In Section 5.4.1, results obtained just performing an FFT of the signal are illustrated. In Section 5.4.2, a more sophisticated algorithm for source localization is introduced and, in Section 5.4.3, the results

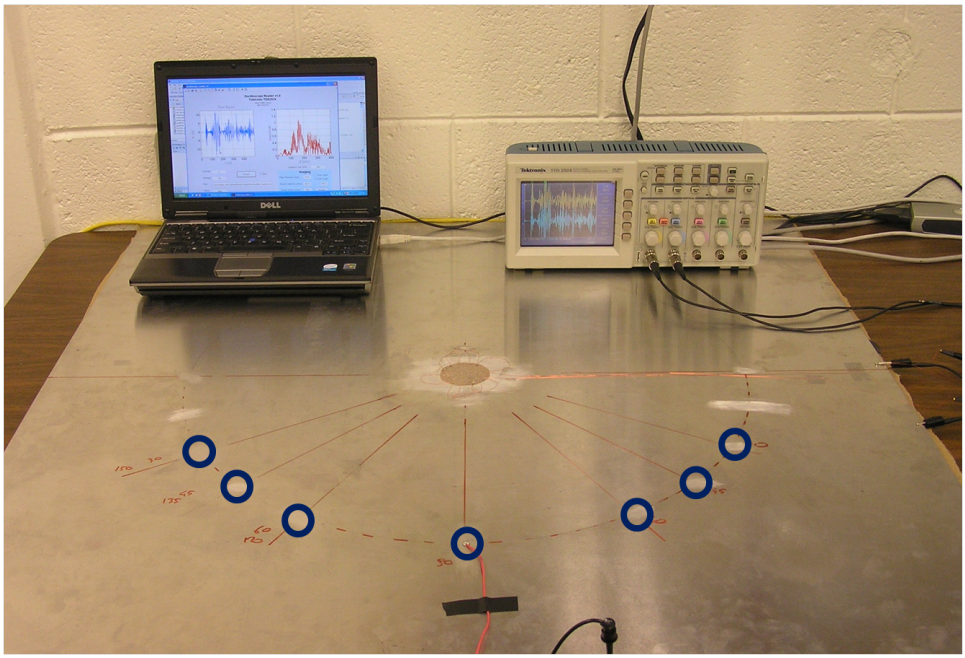

Figure 56: Experimental setup for WS–FSAT testing: sensed voltage is acquired with Tektronix TDS2024 oscilloscope and then transferred to a PC for processing. Circles denotes positions of simulated acoustic sources.

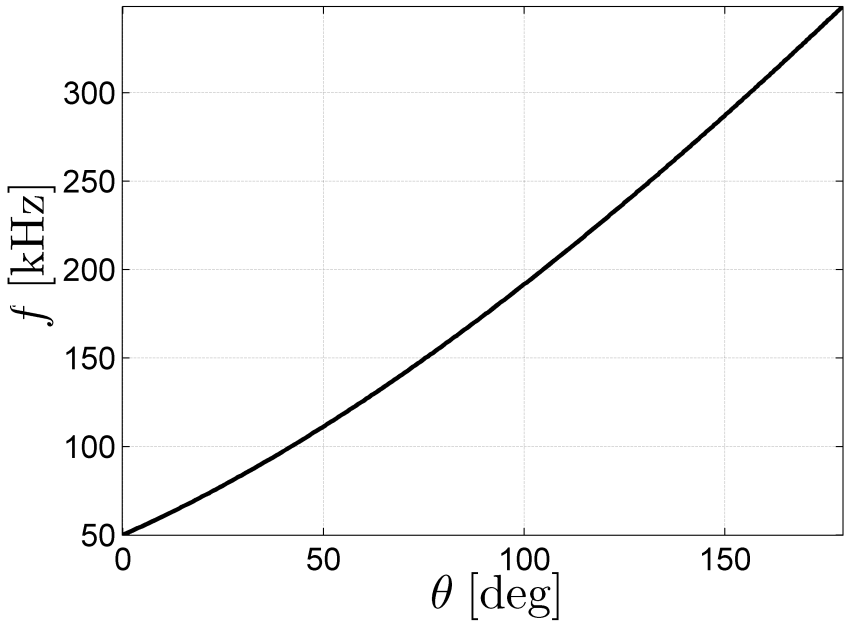

Figure 57: WS–FSAT prototype θ–frequency correlation map based on A_0 mode dispersion branch in a 0.82 mm–thick aluminum plate.

Table 7: Actual vs estimated peak frequencies and angles of DOA for WS–FSAT prototype.

Actual	f [kHz]	**84**	**104**	**126**	**174**	**228**	**257**
	θ [deg]	**30**	**45**	**60**	**90**	**120**	**135**
WS–FSAT estimation	f [kHz]	93	102	132	188	229	266
	θ [deg]	37	44	64	98	120	139

obtained with the algorithm are presented.

5.4.1 Spatial filtering & frequency dependent directionality

The frequency content of the acquired voltage signals is computed through an FFT to verify the spatial filtering properties of the WS–FSAT, similarly to the data analysis described in Section 4.5.3. Frequency peaks in the spectra are compared with the θ–frequency map of the spiral FSAT based on A_0 mode dispersion branch to detect the direction of the incoming wave (Fig. 57). Test results are shown in Fig. 58, where frequency values corresponding to actual source angular positions are indicated by a red dashed line. The WS–FSAT filters the input signal quite sharply around the expected frequency providing consistently correct information on the source angular location. The maximum localization error in these tests was found to be below 8° (Table 7).

The amplitudes of the frequency peaks for the tested directions are compared to each other in Fig. 59, in which the relative amplitudes, computed dividing the obtained values with the highest one, are shown. The difference in the amplitudes is due to the non–uniform sensitivity of PVDF at various frequencies, to the thresholding procedure of electrodes which introduces different filtering weights, and to the non–flat spectrum of the source excitation. However, this DOA–dependent sensed amplitude is a secondary effect compared to the WS–FSAT frequency sharp filtering observed in Fig. 58. In fact directional information is extracted by the frequency peak location, not by its intensity.

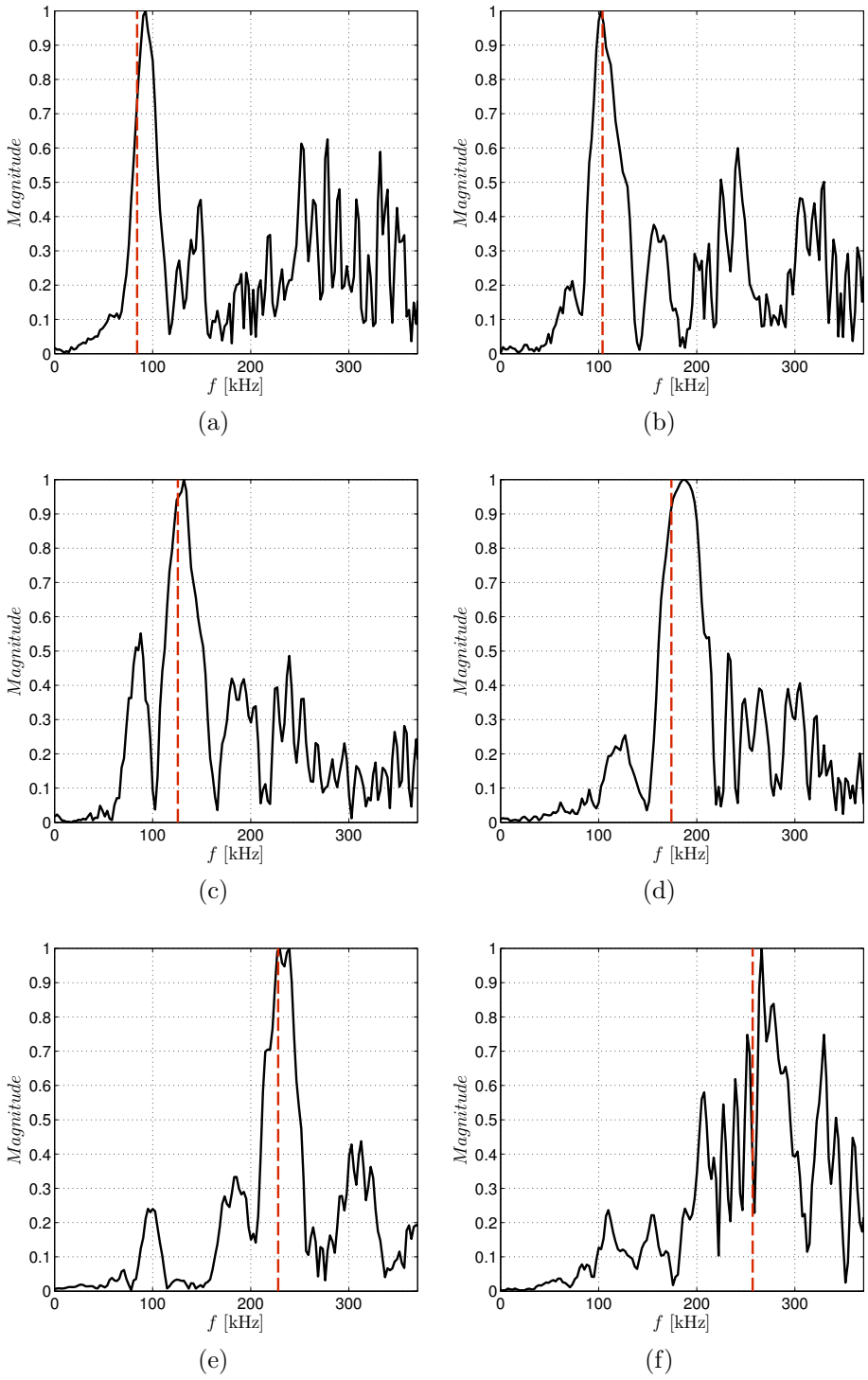

Figure 58: Normalized spectra of signals sensed by WS–FSAT due to various locations of acoustic sources; red dashed line expected frequency peak position according to correlation map: (a) 30° source; (b) 45° source; (c) 60° source; (d) 90° source; (e) 120° source; (f) 135° source.

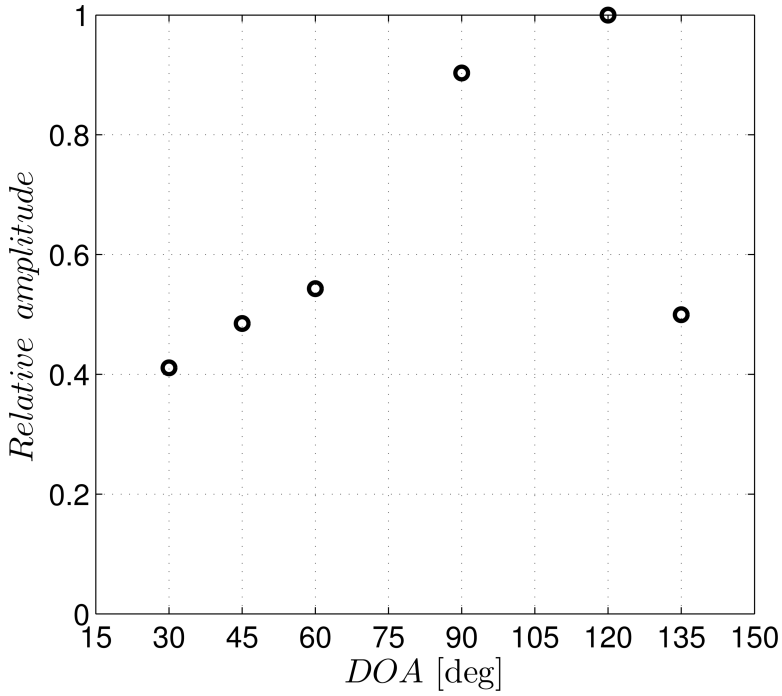

Figure 59: Relative amplitude of the frequency peaks for the tested directions.

5.4.2 Algorithm for source localization

The directional properties of the WS–FSAT enable imaging of 2D areas through the data recorded from the WS–FSAT. Two-dimensional imaging requires the estimation of both distance and directional information from the recorded signal. The latter is associated to specific spectral features of the acquired waveform. In particular, the DOA is defined, as previously, by a peak in the signal spectrum centered around the frequency corresponding to the direction of the incoming wave. This relies on the assumption that the frequency content of the excitation signal is sufficiently flat in the considered frequency range, so that the filtering properties of the WS–FSAT are not biased by a narrowband excitation. The traveled distance is evaluated through the estimation of time-of-flight (TOF). Complications related to the dispersion of GW propagation are minimized through the analysis of the recorded signals using the Warped Frequency Transform (WFT) [17, 7].

5.4.2.1 Warped Frequency Transform

The WFT performs a deformation of the frequency axis to compensate for dispersion and to allow for accurate estimation of the traveled distance in broadband propagation environments.

Assume that the acquired signal by the receiving transducer is $s(t)$ and that it is due to the propagation of a guided wave generated by an acoustic source in an unknown position but at the known time instant, $t = 0$. Knowing $s(t)$ and knowing the propagation characteristics of the guided wave mode, it is possible to describe a field quantity, $u(x', t)$, representing the guided wave mode of interest as [83]:

$$u(x', t) = \int_{-\infty}^{+\infty} S(\omega) e^{-j[k(\omega)x' - \omega t]} d\omega \tag{62}$$

where t is time and x' is the propagation distance of the guided wave measured from the receiving transducer position, $k(\omega)$ is the angular wavenumber of the guided wave mode as a function of angular frequency, ω, and $S(\omega)$ is the Fourier transform of $s(t)$. Considering the group velocity of the GW mode to be tracked, i.e. A_0 in the considered application, $c_{A_0}(\omega) = d\omega/dk$, Eq. 62 can be rewritten as:

$$u(x', t) = \int_{-\infty}^{+\infty} S(\omega) e^{-j\left[\int_0^{\omega} \tau(\omega') d\omega' - \omega t\right]} d\omega \tag{63}$$

where $\tau(\omega) = x'/c_{A_0}(\omega)$ is the group delay of the mode traveling along the structure.

The goal is to convert $s(t)$ to a function of propagation distance rather than time and to compensate the dispersed signal in $s(t)$. If $s(t)$ is supposed to be back–propagated, the signal converges to reach a minimum in spatial duration when it crosses the $t = 0$ line; continuing the back–propagation it would result in a signal divergence (Fig. 60). Therefore, the dispersion compensated space signal with the minimum duration, $s_w(x)$, can be computed as:

$$s_w(x) = u(x' = -x, t = 0) = \int_{-\infty}^{+\infty} S(\omega) e^{j \int_0^{\omega} \tau(\omega') d\omega'} d\omega \tag{64}$$

where x is the distance from the receiving transducer, but in the opposite direction with respect to the previous x'.

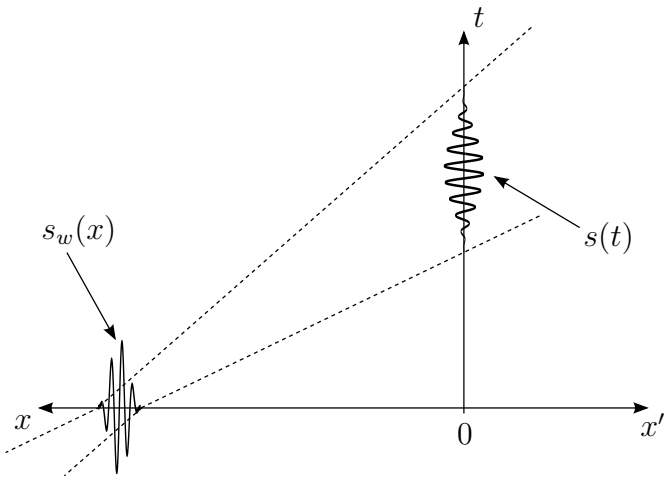

Figure 60: Schematic diagram illustrating the application of the dispersion compensation algorithm. Receiving transducer is placed at the axes origin 0.

Equation (64) is evaluated by designing the warping map $w(\omega)$ according to the dispersion relation of the GW mode to be tracked, based on the following rule:

$$K \frac{d\, w^{-1}(\omega)}{d\omega} = \frac{1}{c_{A_0}(\omega)} \tag{65}$$

where K is a normalization constant and $w^{-1}(\omega)$ denotes the functional inverse of $w(\omega)$. The WFT thus represents the signal spectrum, $S(\omega)$, as a function of a warped frequency, ω_w:

$$\omega_w \doteq w^{-1}(\omega) \Leftrightarrow \omega = w(\omega_w) \tag{66}$$

Equation (64), in fact, with the introduction of ω_w becomes:

$$s_w(x) = \int_{-\infty}^{+\infty} S(w(\omega_w)) e^{jKx\omega_w} \dot{w}(\omega_w) d\omega_w \tag{67}$$

where $\dot{w}(\omega_w) = dw(\omega_w)/d\omega_w$.

Finally, Eq. (67) represents the warped frequency transform, applied to the acquired time signal $s(t)$, and allows to calculate the warped signal in space, $s_w(x)$. The WFT can be efficiently computed as a non-uniform Fourier transform associated with $w(\omega)$, followed by a conventional inverse FT [17].

5.4.2.2 STFT for distance and direction retrieval

The STFT of the acquired signal is an ideal tool for the simultaneous retrieval of both DOA and TOF. The STFT of the warped signals produces spectrograms where time is directly replaced by a space variable expressing the traveled distance. Furthermore, all frequency components associated to a specific propagation path of the incident wave packet are mapped to the same traveled distance. Acoustic events, due to wave generation, therefore appear as localized high-energy spots in the warped spectrogram, with range and angular information provided by the spatial and frequency coordinate, respectively. Spectral localization produced by the filtering effect of the WS–FSAT yields a warped frequency information, which can be univocally associated to the corresponding (unwarped) frequency through the inverse warping map $w^{-1}(\omega)$. Finally, the DOA is estimated by combining eq. (55) with the dispersion relation of the considered medium. The procedure, illustrated in Fig. 61, allows converting the warped spectrogram of a signal recorded by the WS–FSAT into a polar image of the inspected area which directly provides location information for the source (see Section 5.4.3).

5.4.3 Results

The imaging technique presented in the previous section has been applied to the FSAT signals acquired in the experiment presented in Section 5.3.

The voltage signal, $s(t)$, measured in the case of the source positioned at 45° is shown in Fig. 62(a) and the relative time–frequency representation is presented in Fig. 62(b). As expected, a high-energy spot appears at the intersection between the

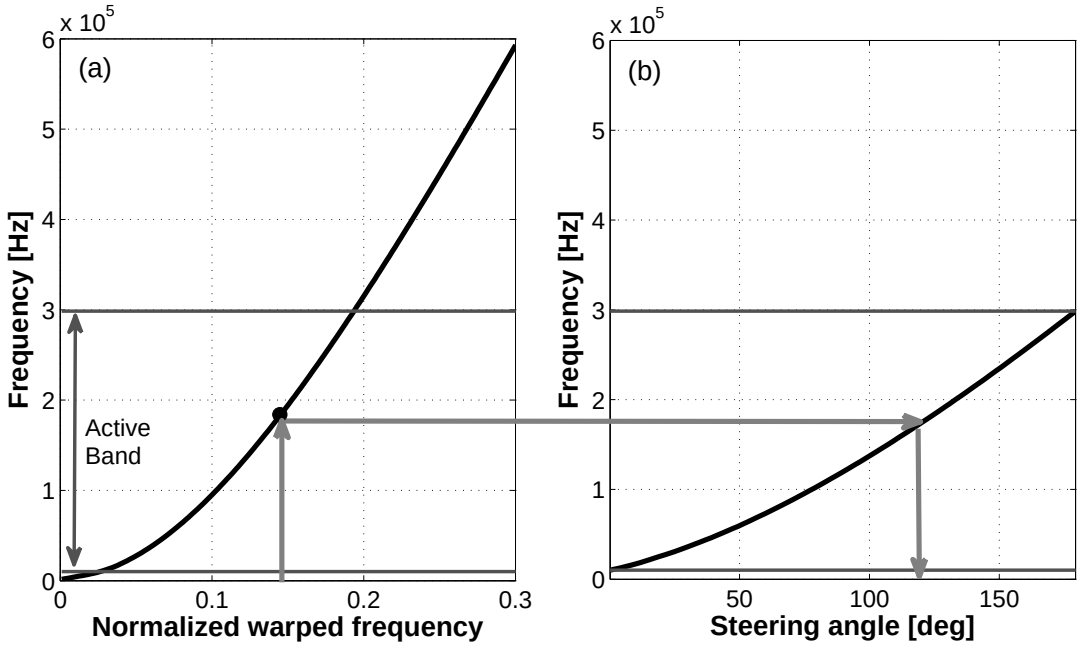

Figure 61: Directional information retrieval from the warped spectrogram. (a) Warped to unwarped frequency map obtained from eq. (65). (b) Frequency-angle map calculated by plugging the dispersion relation of the medium into eq. (55).

group delay curve $\tau(\omega) = D/c_{A_0}(\omega)$ associated with propagation over the distance $D = 300$ mm between the WS–FSAT and the acoustic source (solid line) and the frequency coordinate corresponding to the direction of arrival (dashed line).

The WFT provides the desired signal compression and distance information, as it can be seen from the warped signal, $s_w(x)$, in Fig. 62(c). A similar information on wave packet compression due to dispersion compensation can be observed from the warped spectrogram, obtained performing a conventional STFT to the warped signal, shown in Fig. 62(d). In particular, three wave–packets are present in the warped signal graph, but only one energy spot around 0.3m is present also in the warped spectrogram and gives information about the source location. The other two wave–packets, in fact, are due to S_0 mode and their frequency is out of the WS–FSAT active band and thus meaningless for the purpose of source location detection.

The imaging is completed converting directly the warped spectrogram into a polar

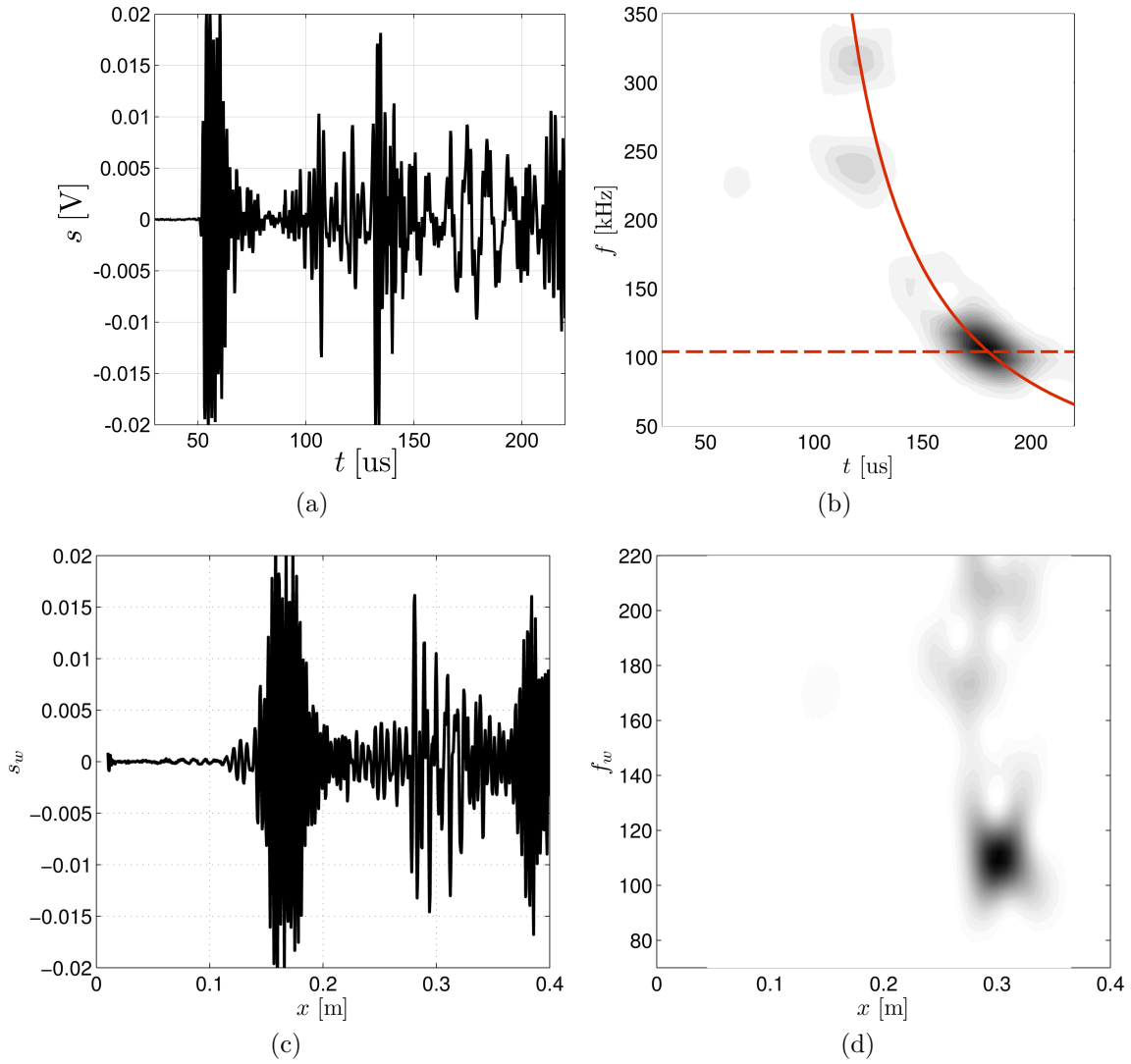

Figure 62: Voltage signal s, measured by the WS–FSAT in the case of the 45° source (a); time-frequency representation: group delay curve in solid line and frequency of DOA in dashed line (b); warped signal, s_w, representation (c) warped spectrogram: f_w warped frequency (d).

image of the domain through the mapping procedure illustrated in Fig. 61. The corresponding source imaging in the spatial domain is displayed in Fig. 63(b). Secondary lobes are visible, but their intensity is considerably smaller than the peak amplitude of the main lobe, whose position is only 4.6mm away from the actual source location. The remaining polar images of Fig. 63 are relative to the other source angular locations, and are obtained in the same way of the just analyzed 45° case. The actual

source positions are indicated by '+' markers and the maximum localization error in these tests was found to be below 30mm.

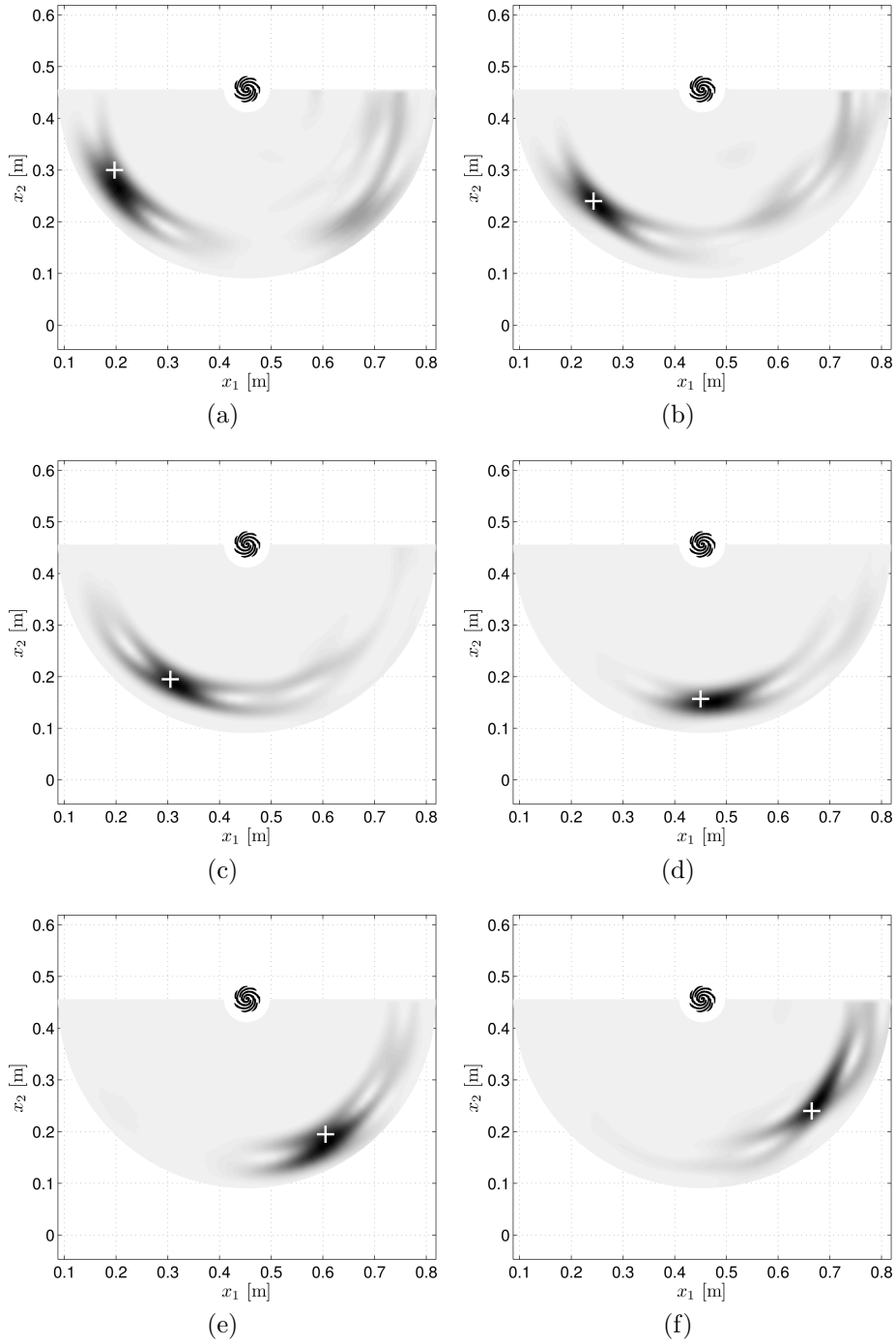

Figure 63: Imaging of acoustic sources at various locations obtained through the spectrogram re–mapping technique. Actual source positions are indicated by '+' markers: (a) 30° source; (b) 45° source; (c) 60° source; (d) 90° source; (e) 120° source; (f) 135° source.

5.5 Conclusions

In this chapter, a WS–FSAT prototype is presented and it is demonstrated that fully-functional devices can be produced exploiting a convenient fabrication approach based on inkjet printing of the electrode patterns on PVDF substrate. The fabricated device has been tested for acoustic sources angular detection. The presented results is obtained by processing the differential output of a single WS–FSAT, i.e. source angular localization has been actually achieved using only one channel. The proposed device, thus, represents a very promising option for lightweight, low–cost and hardware–efficient inspection in various SHM environments. A dedicated signal processing algorithm for the output of the WS–FSAT has also been presented. It provides imaging of acoustic sources with remarkable accuracy considering that the task is performed using only one channel. This technique not only allows angular locations finding of the sources, but also the estimation of their distance from the WS–FSAT. However it must be stressed out that the source distance is evaluated through the estimation of TOF, which implies to know the instant in which the source is fired. In the perspective of an impact detection application, this can be an important limitation. To overcome this issue, correlation techniques, based on matching of broad band signals dispersion, are under examination.

CHAPTER VI

ACTUATION CONCEPTS FOR WS–FSAT

6.1 Overview

In Chapter 5 a prototype of WS–FSAT has been presented and its frequency–dependent directionality characteristics have been tested in sensing.

This chapter describes a preliminary testing of WS–FSAT for actuation. First, a voltage signal is applied to the electrodes of the PVDF prototype considered in the previous chapter and the wavefield generated in the plate is recorded by a SLDV. Next, a Macro Fiber Composite (MFC) [84] WS–FSAT architecture is discussed as a potential improvement of the transducer actuation capability.

6.2 Actuation of PVDF WS–FSAT

Section 5.2 stated that PVDF is not an ideal substrate for actuation, at least compared with piezoceramics, due to its much lower modulus, as it can be observed comparing Table 1 for PZT with Table 6 for PVDF. However, PVDF based transducers have been proposed also for GW generation in structures [54]. The next sections present the results obtained by operating the PVDF prototype in actuation.

6.2.1 Experimental setup

The plate of Fig. 53 with the WS–FSAT bonded to its center, is instrumented. For hardware connections simplicity's sake, a voltage signal was applied only to one electrode's group of the WS–FSAT. This is equivalent to considering a transducer with an electrode distribution illustrated in Fig. 64(a), or, in other words, to operating the WS–FSAT in a single channel mode. The directivity of the single channel WS–FSAT, depicted in Fig. 64(b), is less performing than considering both channels; in fact, a

lower spiral distribution of maxima is observed, comparing it with the directivity of the entire WS–FSAT, depicted in Fig. 50(b). However, even in single channel mode, a clear spiral shape is preserved, and therefore also the directional capability of the device.

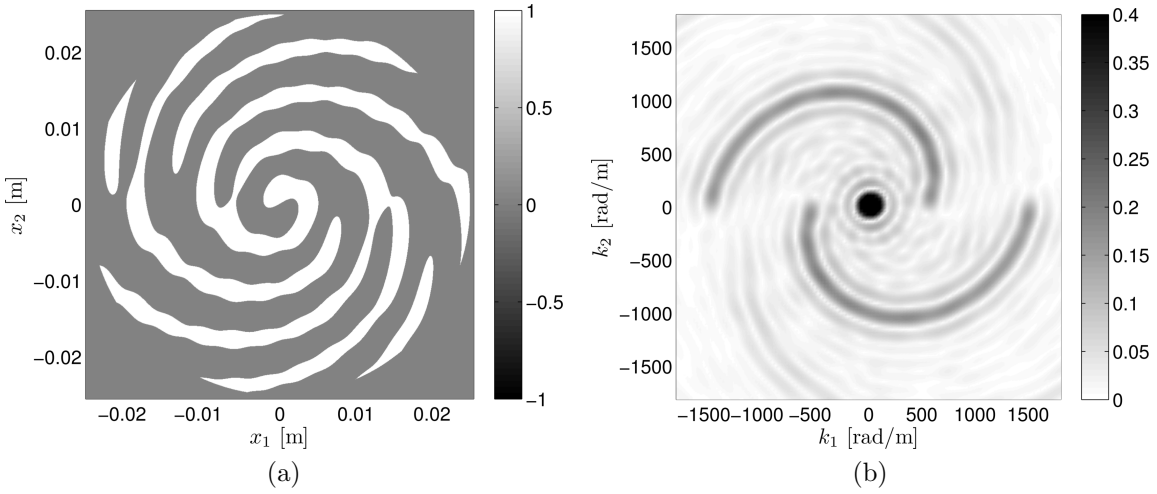

Figure 64: WS–FSAT scheme of actuation: pattern of the activated electrode (a), and corresponding directivity function, $|\mathcal{D}(\boldsymbol{k}_0(\omega), \theta)|$ (b).

The input voltage signals are provided by an amplified Agilent 33220A function generator and the wavefield generated by the WS–FSAT is recorded with a SLDV. Reflective tape is applied in the side without the transducer, as shown in Fig. 65, to enhance the quality of the laser scanning.

Two kinds of analysis are performed. The first considers the successive application of tone bursts centered at different frequencies to verify if the radiation pattern of the transducer is along the correspondent direction predicted by the θ–frequency correlation map of Fig. 57. A second analysis consists in exciting the WS–PVDF with a chirp characterized by a frequency content covering the entire bandwidth of the device. This excitation produces a sweep in the directions of generated waves as the signal evolves in time.

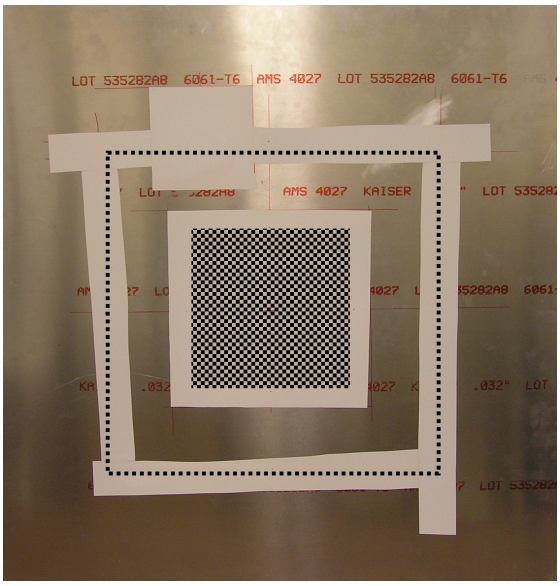

Figure 65: Reflective tape application on the plate side without the transducer. Two SLDV scan grids are highlighted in black: external, single line, grid for tone bursts polar plots; internal square grid for chirp wavefield recording. Transducer in the center of the grids, mounted on the opposite side (not seen).

6.2.2 Tone burst excitations

The tone bursts considered are 7–cycles at different excitation frequencies. In each case, the perturbations generated by the actuated transducer are recorded in scan points located along the edges of a square (see Fig. 65). Each side of the square measures 50 cm and the transducer is placed in the center. The radiation patterns are evaluated constructing polar plots with the RMS values of the time acquisitions along the scan path, similarly to what done to obtain the directivity polar plots of Fig. 31 for the quadrilateral array case.

The polar plots obtained from the elaboration of the data acquired by the tone bursts analysis are illustrated in Fig. 66. Preferred radiation directions are evident and are in agreement with the directions predicted by the θ–frequency correlation map of Fig. 57. The presence of side–lobes can be observed in the cases of the three lowest frequencies, i.e. 60 kHz, 90 kHz and 120 kHz. Side–lobes may be reduced activating both channels of the WS–FSAT, due to the better directivity of this configuration.

The three mid frequency cases, i.e. 150 kHz, 180 kHz and 210 kHz, presents a cleaner radiation pattern. The polar plots of the three highest frequencies analyzed, i.e. 250 kHz, 280 kHz and 330 kHz, are quite noisy. Possible reasons could be a poor response of the amplifier and/or of the PVDF substrate at high frequencies of excitation, but further studies would be necessary to assess better this issue.

6.2.3 Chirp excitation

The time history and the spectrum of the adopted chirp are depicted in Fig. 67(a). The time–frequency representation of the signal is illustrated in Fig. 67(b). The wavefield generated by the chirp activated WS–FSAT is recorded along the square checkered area of Fig. 65.

The obtained wavefield is represented by the snapshots collected at successive time instants and shown in Fig. 68. It is worth noting how the radiation pattern evolves with time, changing continuously direction as frequency sweeps. Moreover, it is interesting to observe the reduction in the wavelength of the propagating waves. This can be easily perceived comparing the first snapshot, i.e. t =194 us, with the last one, i.e. t =390 us. This is a direct consequence of exciting with a chirp which is a linear swept–frequency sine signal; in fact, looking at the time–frequency representation of the signal (Fig. 67(b)), the instantaneous excited frequency linearly increases with time, and therefore the wavelength of the generated waves reduces accordingly. This wavelength reduction, and therefore an increment in the wavenumber associated with the propagating waves, is more evident transforming the captured wavefield $u_3(x_1, x_2, t)$ to the wavenumber domain to obtain $\hat{u}_3(k_1, k_2, t)$ using a 2D FT, which is defined as:

$$\hat{u}_3(k_1, k_2, t) = \int_{-\infty}^{+\infty}\int_{-\infty}^{+\infty} u_3(x_1, x_2, t) e^{-jk_1x_1} e^{-jk_2x_2} dx_1 dx_2 \tag{68}$$

where k_1, k_2 are the wave vector components along the horizontal and vertical axis,

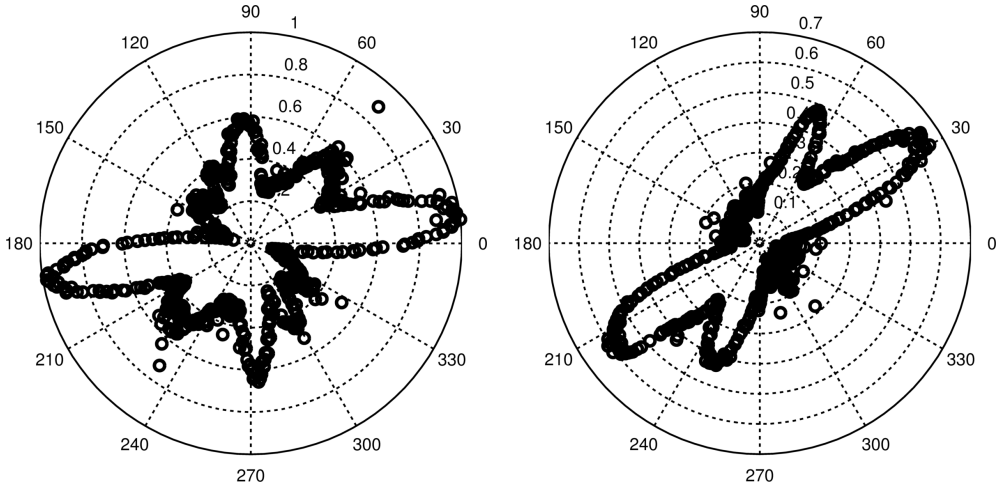

(a) (b)

(c) (d)

(e) (f)

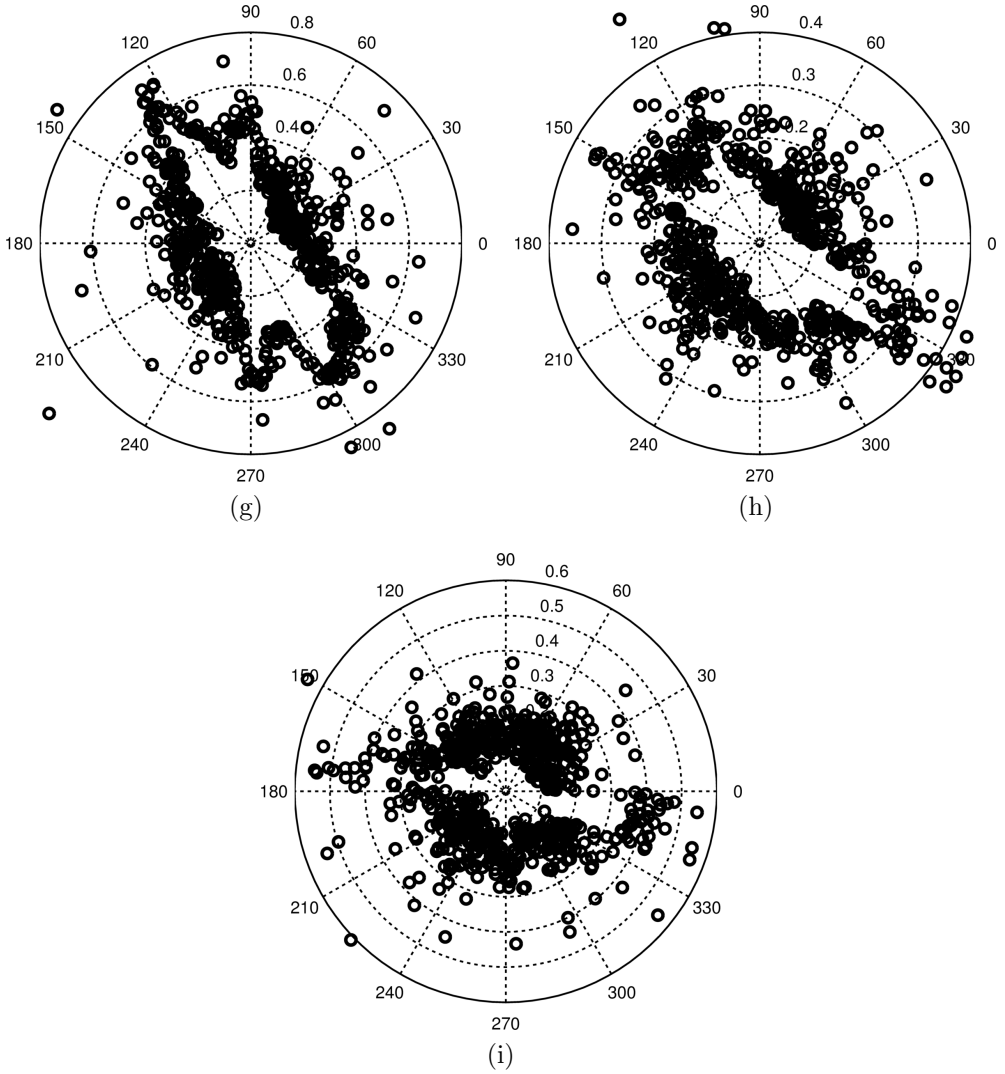

Figure 66: RMS radiation directionality of the WS–FSAT obtained with tone burst excitations centered at different frequencies: (a) 60 kHz; (b) 90 kHz; (c) 120 kHz; (d) 150 kHz; (e) 180 kHz; (f) 210 kHz; (g) 250 kHz; (h) 280 kHz; (i) 330 kHz.

respectively. The wavenumber content of the plate response at the same time instants of Fig. 68 is illustrated in Fig. 69. The directional wave pattern is evident also here looking at the direction who connects the peaks at each instant. The distance of the peaks from the origin of the wavenumber domain increases with time, corresponding to the aforementioned wavelength reduction. Moreover, overlapping each wavenumber snapshot, the peaks appear aligned along the wavenumber spiral which defines the WS–FSAT, as shown in Fig. 70, providing a clear validation of the WS–FSAT design.

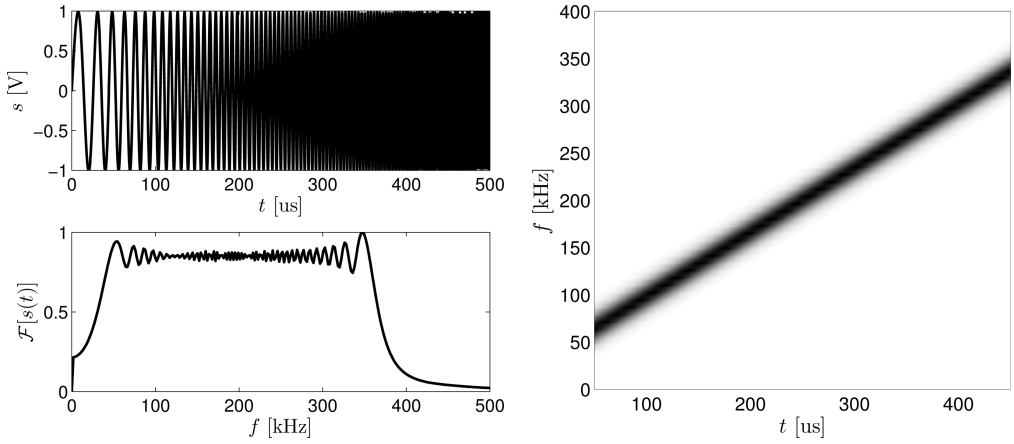

(a) (b)

Figure 67: Chirp excitation from 30 kHz to 380 kHz: signal time history and spectrum (a), and signal time–frequency representation (b).

The presence of side–lobes in the snapshots, of both Fig. 68 and 69, is due to the same reasons enounced in Section 6.2.2.

Another possible representation of the chirp generated wavefield considers successive time intervals and computes the RMS of the plate response for each time interval; the RMS of the j–th time interval is computed as:

$$RMS_j(x_1, x_2) = \sqrt{\sum_{t_i=t_{lj}}^{t_{uj}} u_3(x_1, x_2, t_i)^2 / N_j} \tag{69}$$

where $u_3(x_1, x_2, t)$ is the recorded out–of–plane displacement field, t_{lj}, t_{uj} are the lower and upper boundaries of the j–th time interval respectively, and N_j is the number of time instants recorded in the j–th interval.

In this way, the energy distribution associated to the time evolution of the radiation pattern can be observed. The RMS plots are presented in Fig. 71. Of course, the radiation pattern is the same of those observed previously. For the first time interval, i.e. $0 \leq t < 100$ us, no preferred propagation direction is noted; this is caused by the very first part of the chirp signal which excites low frequencies outside the bandwidth of the WS–FSAT and also because the waves take a certain time to propagate in space and in the initial time interval the propagation is still developing. In the other time

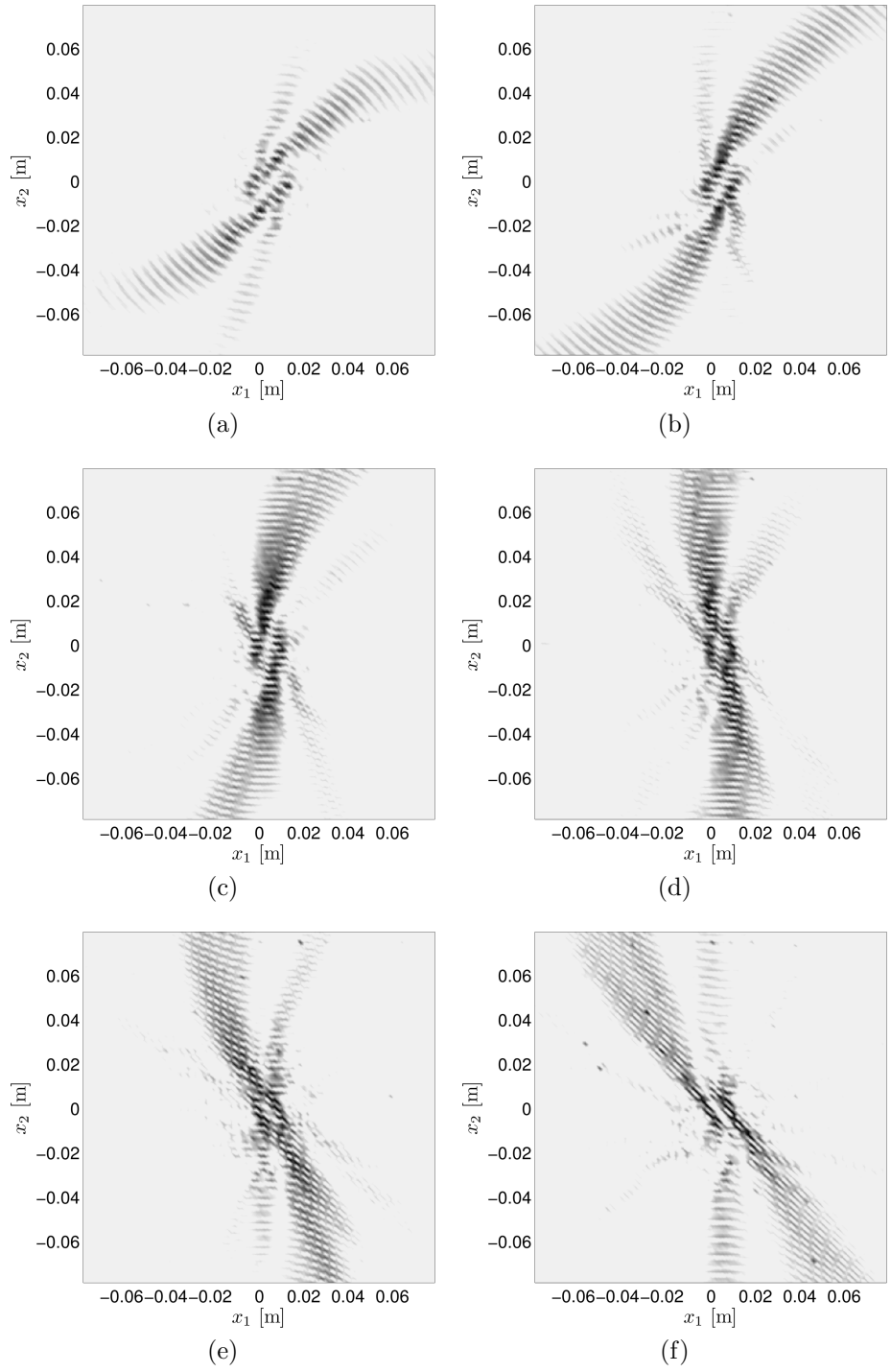

Figure 68: Snapshots at successive time instants of wavefield generated by chirp excitation of the WS–FSAT: (a) $t = 194$ us; (b) $t = 234$ us; (c) $t = 273$ us; (d)$t = 312$ us; (e) $t = 351$ us; (f) $t = 390$ us.

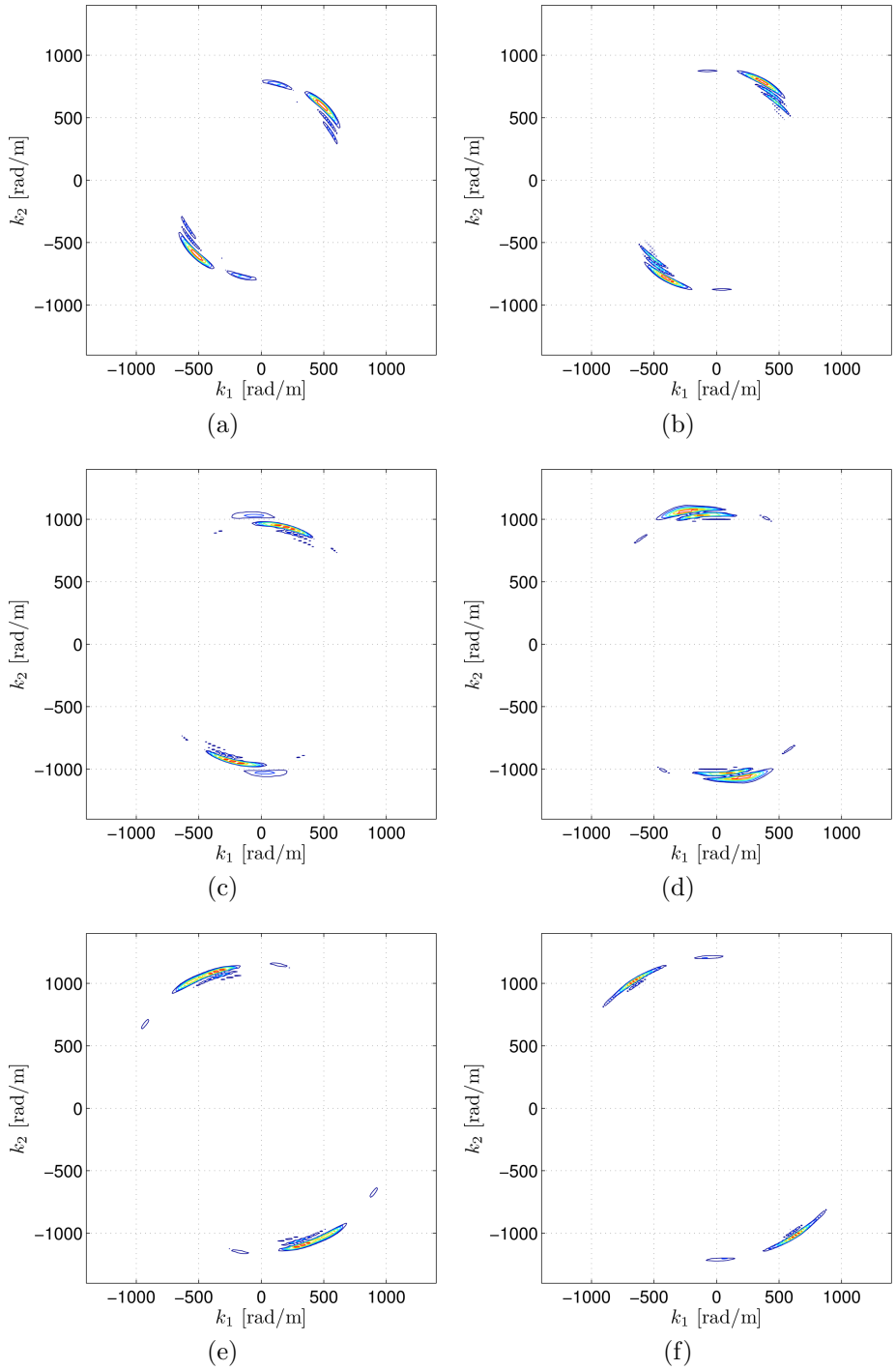

Figure 69: Wavenumber content at successive time instants of wavefield generated by chirp excitation of the WS–FSAT (linear scale): (a) $t = 194$ us; (b) $t = 234$ us; (c) $t = 273$ us; (d)$t = 312$ us; (e) $t = 351$ us; (f) $t = 390$ us.

intervals, the radiation pattern is evident; again, when high frequencies are excited, the results are quite noisy, similarly to what observed for the polar plots of Fig. 66.

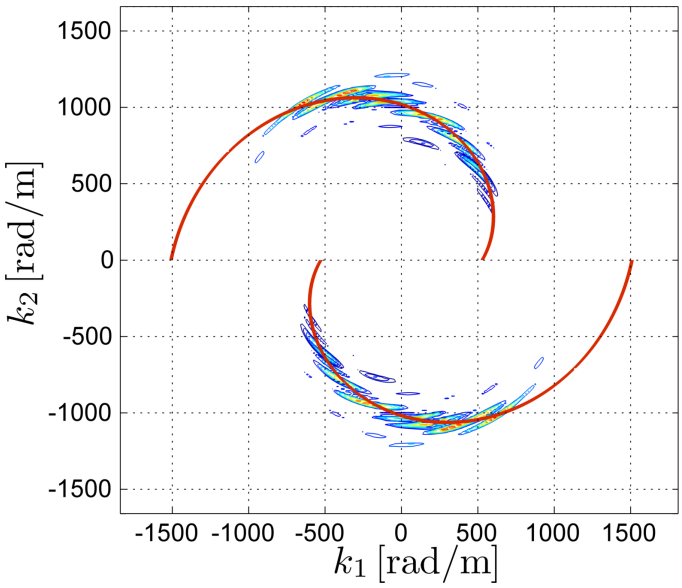

Figure 70: Overlap of contour wavenumber snapshots of Fig 69 (linear scale). In red, wavenumber spiral which defines the WS–FSAT.

Similarly to what done in Section 5.4.1 for sensing, the behavior at different frequencies of the WS–FSAT based on PVDF substrate is here analyzed in actuation. The signals of scan points along a circumference have been selected from the wavefield obtained by the chirp excitation (Fig. 72(a)) and the RMS of each signal is visualized in the polar plot of Fig. 72(b). The intensity of the actuation performance is stronger in particular from 30° to 150° and from 210° to 330°. Reasons of this non–uniformity can be the PVDF frequency dependent behavior, and the thresholding procedure of electrodes which introduces different filtering weights.

The two approaches, i.e. tone burst and chirp excitations, are two equivalent strategies to experimentally validate the actuation capability of the WS–FSAT. The frequency dependent directionality expected from the numerical analysis of Section 4.4 has been achieved, in fact, in both cases. The obtained results outlines the WS–FSAT as a promising device which may be adopted for active structural scanning. Due to its light weight and hardware simplicity it could be embedded to critical aerospace structural elements and operated remotely to asses the integrity of the monitored

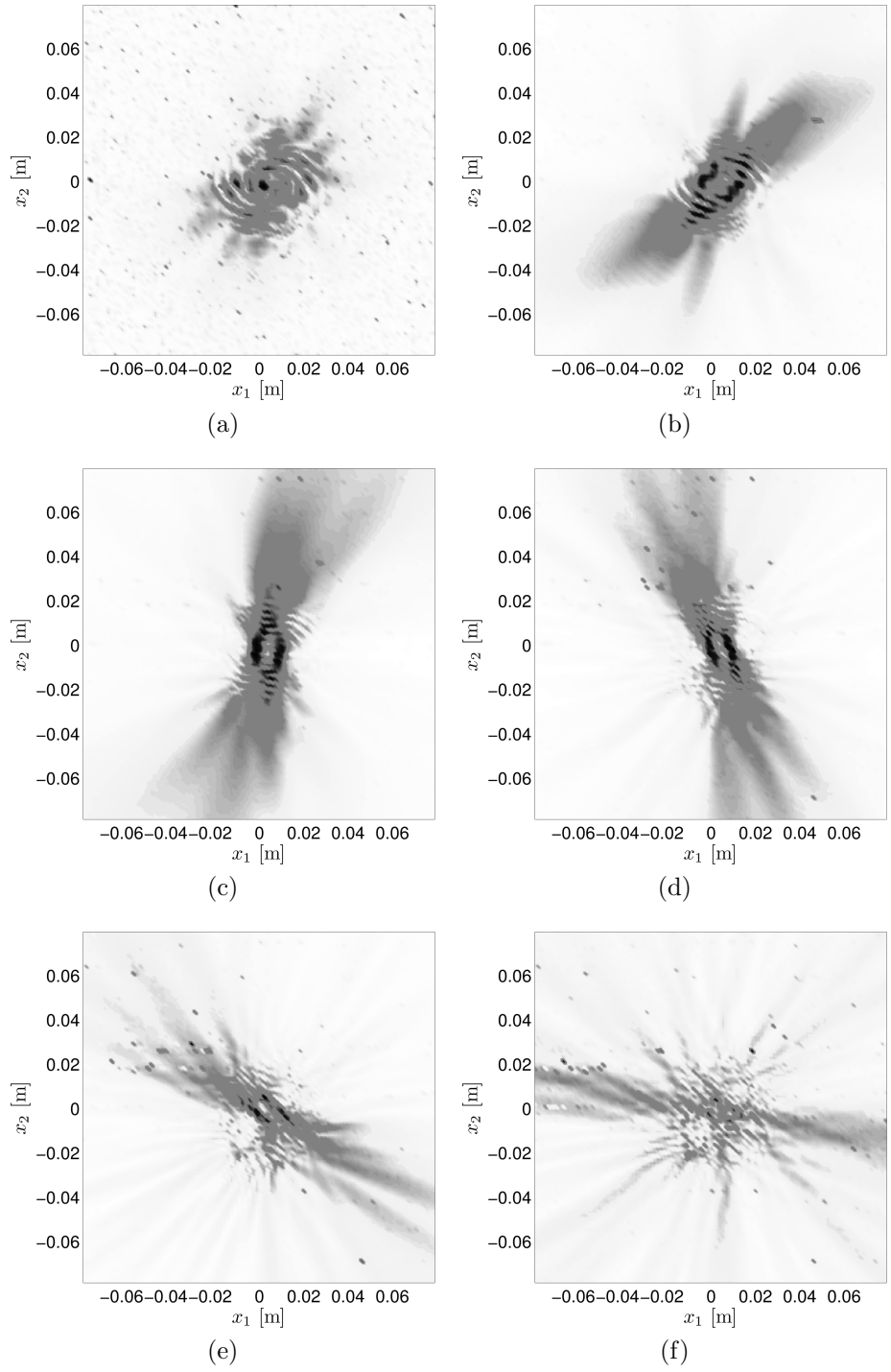

Figure 71: RMS computed for successive time intervals of wavefield generated by chirp excitation of the spiral FSAT: (a) $0 \leq t < 100$ us; (b) 100 us $\leq t < 200$ us; (c) 200 us $\leq t < 300$ us; (d) 300 us $\leq t < 400$ us; (e) 400 us $\leq t < 500$ us; (f) 500 us $\leq t < 600$ us.

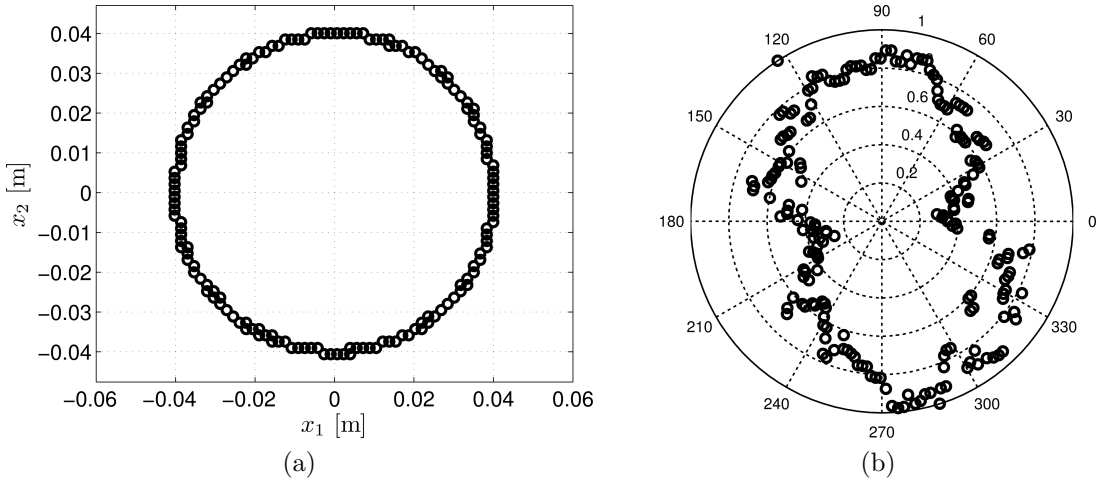

Figure 72: WS–FSAT direction dependent actuation intensity: selected points for actuation directional analysis (WS–FSAT placed in the center, not seen) (a), normalized RMS of acquired signals in selected points (b).

structure. In a pulse–echo scheme of operation, the WS–FSAT could generate waves in selected directions and sense eventual back scatterers due to the presence of damage, localizing it.

6.3 MFC WS–FSAT

The active materials which have been discussed in this work with detail are PZT and PVDF. PZT, and piezoceramics in general, have a high structural stiffness, which provides them a strong, voltage dependent actuation authority. Additionally, piezoceramics are capable of interacting with dynamic systems at frequencies spanning from about 1 Hz well into the megahertz range. However, there are several practical limitations to implementing this delicate type of material. Namely the brittle nature of ceramics makes them vulnerable to accidental breakage during handling and bonding procedures, and limits their ability to conform to curved surfaces. Moreover they are usually quite bulky and their application on thin structures could interfere and distort the wavefield, as shown in Fig. 73. The RMS of the wavefield generated by a propagating wave from the bottom to the top clearly shows how a PZT patch can prevent the wave propagation across the region covered by PZT (Fig. 73(a)),

and actually how the waves are reflected back (Fig. 73(b)). PVDF, as a piezoelectric polymeric film, is very thin, flexible and lightweight, overcoming the limitations of PZT, but, featuring a low structural stiffness, its actuation efficacy is compromised.

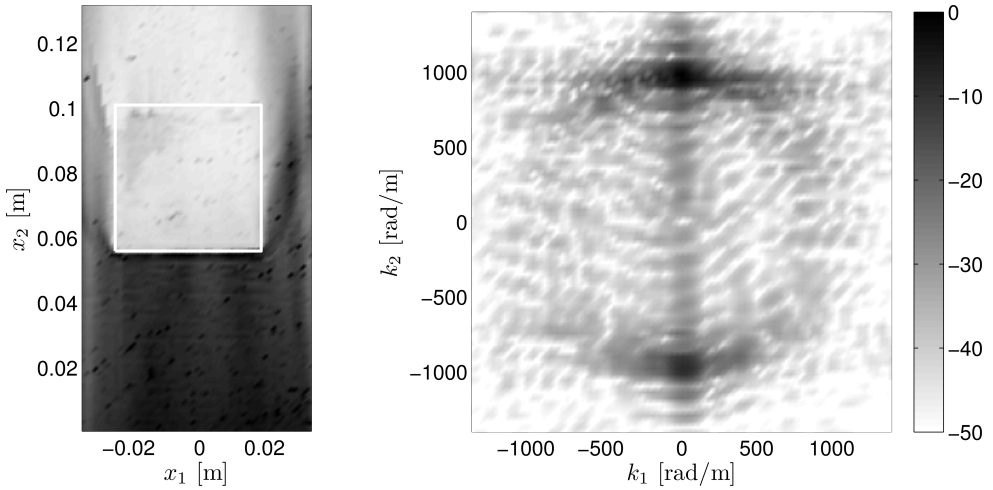

Figure 73: PZT patch influence on crossing wavefield: wavefiled RMS, patch dimensions highlighted by solid white line (a), wavenumber content of wavefield at 160 kHz, dB scale (b).

The idea of a composite material consisting of an active piezoceramic fibrous phase embedded in a polymeric matrix phase remedies many of the aforementioned restrictions. Typically, crystalline materials have much higher strengths in the fiber form, where the decrease in volume fraction of flaws leads to an increase in specific strength. Also, in addition to protecting the fibers, the flexible nature of the polymer matrix allows the material to more easily conform to the curved surfaces found in realistic applications. Presently, there is an ever–increasing number of research grade and commercially available composites containing piezoelectric fibers. For example, Piezoelectric Fiber Composites called Active Fiber Composite (AFC) were introduced by Hagood and Bent [28] as an alternative to monolithic piezoceramic wafers for structural actuation applications. AFCs employs high cost, extruded, round piezoceramic

fibers. Also, an additional disadvantage with AFCs is high operating voltage requirements; the attenuation of the driving electric field by unwanted accumulations of low dielectric matrix material between the electrodes and the piezoceramic elements ends to drive voltages higher. Developed by the NASA–Langley Research Center, MFC actuators and sensors present superior qualities among AFCs in performance and behavior. The main difference with AFCs is that the fibers are rectangular, and diced from a regular ceramic. The manufacturing process is quite cheap and repeatable, and the shape of the fibers together with the manufacturing process allows to put the fibers in direct contact with the electrodes, therefore solving the problem of the permittivity mismatch [84]. MFCs thus attracted great interest for new industrial applications and in the academic community as well. Smart Material Corp. is manufacturing MFCs, licensed by NASA in a full scale production. MFCs, due to their interesting properties, can represent a valuable substrate for the manufacturing of a better performing in actuation WS–FSAT. In the next sections, some guidelines for the realization of an MFC–based WS–FSAT will be provided.

6.3.1 Design scheme

A typical MFC transducer is made of an active layer, constituted by uniaxially aligned fibers surrounded by a polymeric matrix, sandwiched between two soft thin encapsulating layers (Fig. 74). The fibers specifically have a rectangular cross–section and are machined from low–cost piezoceramic wafers using a computer controlled dicing saw [85]. The packaging brings the electric field to the active layer through the use of a specific surface electrode pattern. The electrodes can be either continuous, in which case a voltage difference is applied between the top and bottom electrodes resulting in an electric field perpendicular to the plane of the transducer, or interdigitated [28], resulting in a curved electric field mostly aligned in the direction of the fibers (Fig. 75). In the first case, the piezoelectric fibers are driven in the d_{31}–mode,

while in the second case, the fibers are driven in the d_{33}–mode, resulting in a higher achievable free strain but for much higher applied voltages [19].

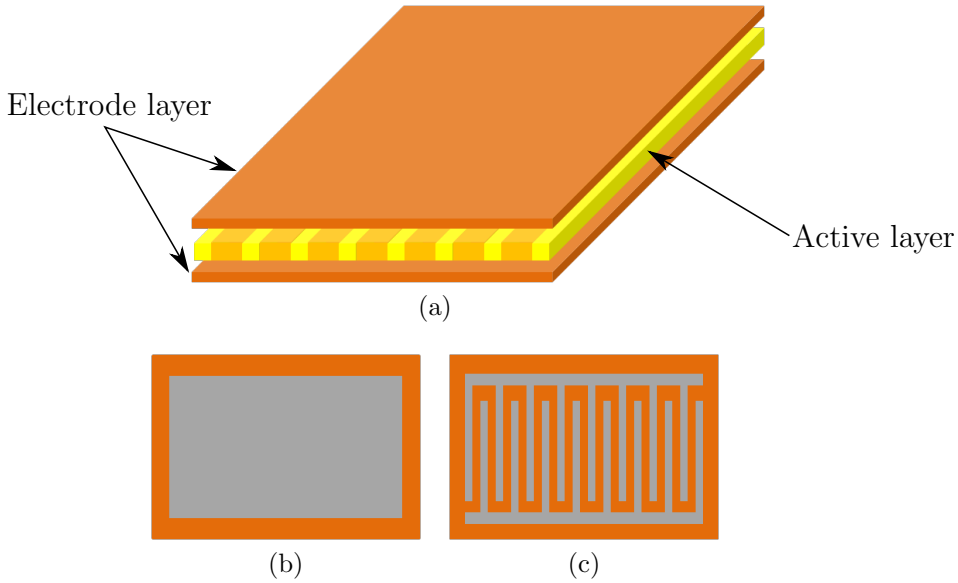

Figure 74: MFC constitutive elements: (a) MFC schematic; (b) d_{31}–mode, continuous electrode; (c) d_{33}–mode, interdigitated electrode.

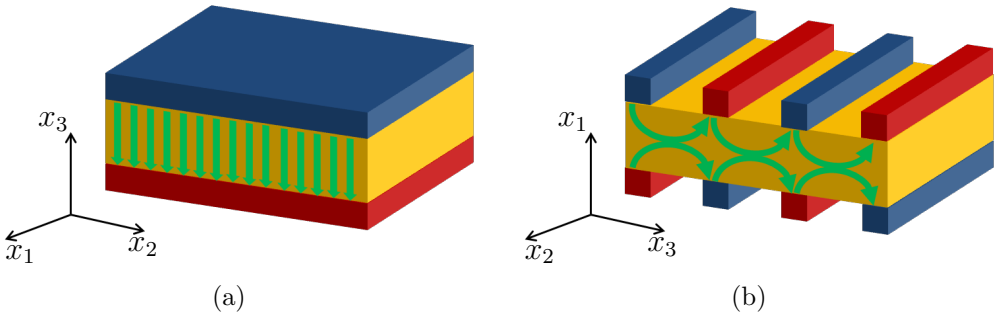

Figure 75: Electric field distribution for different electrode configurations: (a) d_{31}–mode; (b) d_{33}–mode. Positive electrode (red), negative electrode (blu), electric field (green).

In Chapter 2, the theory for directional sensing and generation of GWs with shaped piezo patches was developed assuming a through the thickness polarization of the active material; the electric field resulted then perpendicular to the transducer plane. An MFC operating in the d_{31}–mode presents the same electrical configuration

and it is therefore a suitable substrate for the manufacturing of a WS–FSAT. As done in the case of PVDF in Chapter 5, the fabrication approach would consist in substituting the continuous top electrode with the WS–FSAT shaped electrodes' geometry while the back side metallization would provide the common ground electrical connection (Fig. 76).

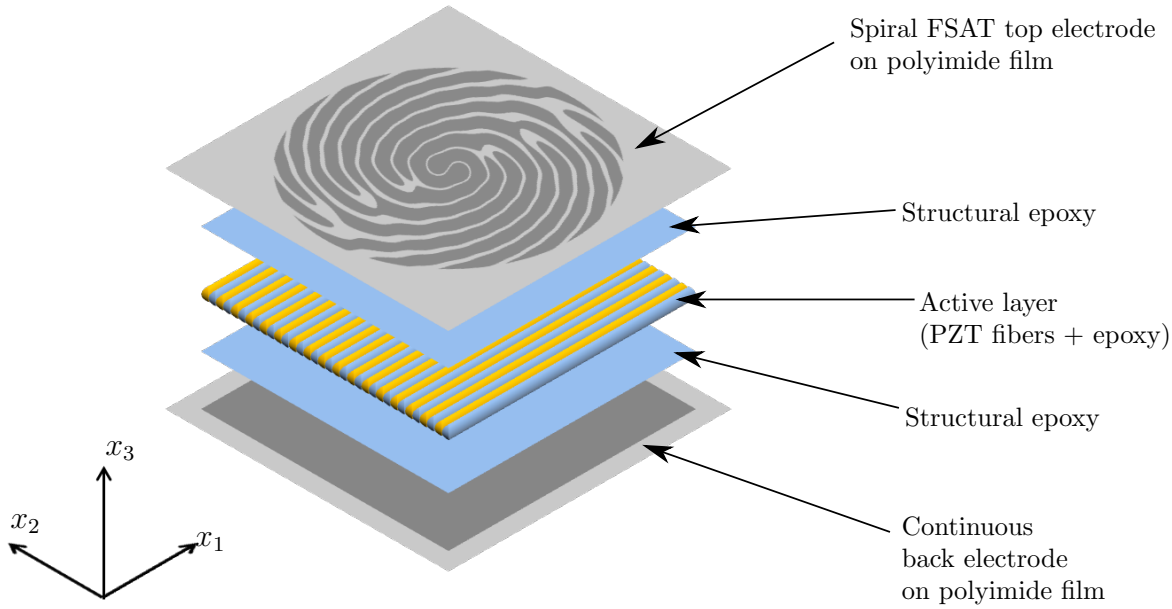

Figure 76: MFC based WS–FSAT architecture.

6.3.2 MFC anisotropy influence

For their composite fiber composite nature, MFCs are clearly anisotropic, in both elastic and piezoelectric properties. For this reason, the material directivity, $\mathcal{H}(\theta)$, defined in Eq. (14), is no longer constant in term of the angle of wave propagation θ. Assuming active fibers aligned along x_1 (Fig. 77), $\mathcal{H}(\theta)$ is re–written here expanding the direction–dependent part, as:

$$\mathcal{H}(\theta) = \frac{t_P}{A_P} \frac{(d_{31}c_{11} + d_{32}\nu_{12}c_{22})\cos^2(\theta) + (d_{31}\nu_{12}c_{22} + d_{32}c_{22})\sin^2(\theta)}{[\boldsymbol{b}^T(\boldsymbol{d}^\sigma \boldsymbol{C}^E \boldsymbol{d}^{\sigma T} - \boldsymbol{\epsilon}^\sigma)\boldsymbol{b}]} \tag{70}$$

Adopting the values listed in Table 8 for the MFC properties, the behavior of $\mathcal{H}(\theta)$ is showed in Fig. 78. Looking at the expression of the sensed voltage of

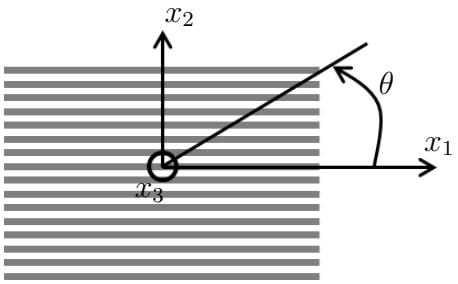

Figure 77: Fibers orientation with respect to direction of wave propagation, θ.

Table 8: MFC material characteristics. MFC is considered globally, not only as its active layer (fiber volume fraction 0.865) [11].

$c_{11} = 31 \times 10^9$ Pa
$c_{22} = 16 \times 10^9$ Pa
$\nu_{12} = 0.31$
$d_{31} = -182 \times 10^{-12}$ C/N
$d_{32} = -173 \times 10^{-12}$ C/N

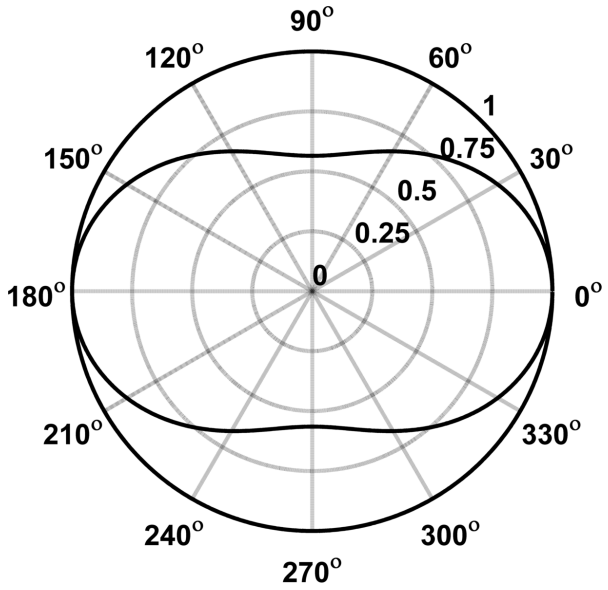

Figure 78: Material directivity, $\mathcal{H}(\theta)$, for MFC with properties listed in Table 8.

Eq. (13), which can be considered also as the actuating voltage for acoustic reciprocity principles, $\mathcal{H}(\theta)$ acts as a θ–dependent weighting factor. Most importantly, it does not influence the frequency dependency of the directionality, and therefore its effect is just secondary and may be neglected. It is possible to offset this secondary effect

on the voltage introducing some compensating factors to the geometric directivity, $\mathcal{D}(\omega, \theta)$, which for the WS–FSAT becomes:

$$\mathcal{D}(\boldsymbol{k}_0(\omega), \theta) = -j\frac{a}{N}\sum_{n=1}^{N}\mathcal{C}_n\left[\frac{J_1\left(a\left|\boldsymbol{k}_0 - \boldsymbol{k}_n\right|\right)}{a\left|\boldsymbol{k}_0 - \boldsymbol{k}_n\right|} - \frac{J_1\left(a\left|\boldsymbol{k}_0 + \boldsymbol{k}_n\right|\right)}{a\left|\boldsymbol{k}_0 + \boldsymbol{k}_n\right|}\right] \tag{71}$$

where $\mathcal{C}_n = 1/\mathcal{H}(\theta_n)$ are the compensating factors. The aim of this modification is to make the product $\mathcal{H}(\theta)\mathcal{D}(\boldsymbol{k}_0(\omega), \theta)$ a constant maximum value, regardless the direction of waves propagation θ, and consequently remove the effect of the active material anisotropy.

The electrodes' distribution computed with the compensated $\mathcal{D}(\boldsymbol{k}_0(\omega), \theta)$ of Eq. (71), and its geometric directivity, for a WS–FSAT with parameters values listed in Table 9, are presented in Fig. 79. For comparison purposes, Fig. 80 shows the WS–FSAT obtained still for the parameters of Table 9, but without anisotropy compensation.

Table 9: WS–FSAT parameters values used to compute geometric directivity $\mathcal{D}(\boldsymbol{k}_0(\omega), \theta)$ in the cases of compensated and not–compensated material anisotropy.

$N = 90$
$\theta_m = 0$ deg
$\theta_M = 180$ deg
$k_m = 528$ rad/m
$k_M = 1509$ rad/m
$a = 2.5$ cm
$\varepsilon = 15\%$

Comparing Fig. 79 with Fig. 80, it is worth noting how the electrodes' areas, along the directions where $\mathcal{H}(\theta)$ is less than 1 (Fig. 78), are thicker in the anisotropy compensated WS–FSAT and consequently the spiral shape of the compensated directivity $\mathcal{D}(\boldsymbol{k}_0(\omega), \theta)$ appears with a stronger weighting in the same range of directions.

Figure 81 presents the product $\mathcal{H}(\theta)\mathcal{D}(\boldsymbol{k}_0(\omega), \theta)$ for four wavenumber values $k_n(\theta_n)$ and associated directions θ_n, computed with the anisotropy compensated version of the WS–FSAT (black lines) and with the original one (grey lines). As expected,

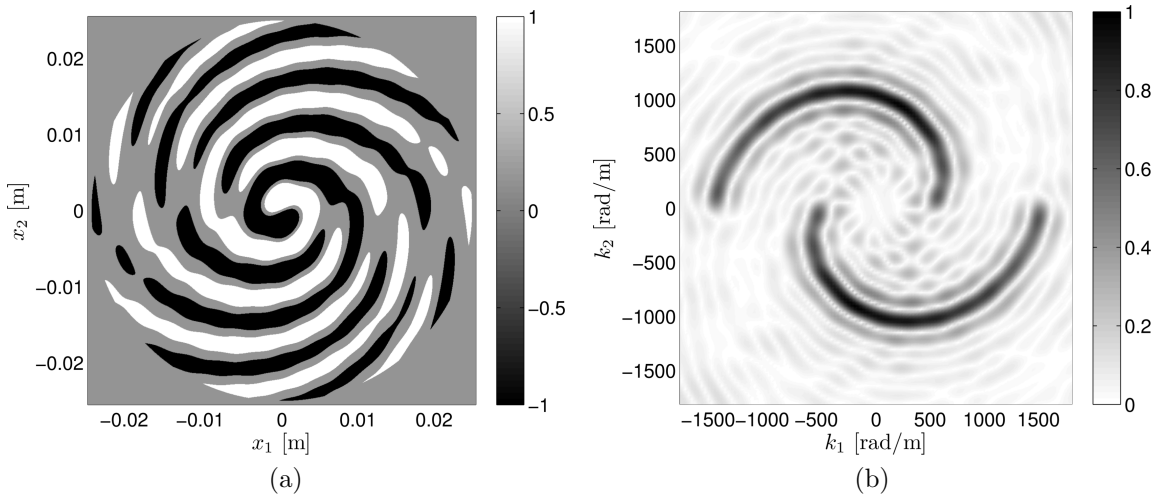

Figure 79: Active material anisotropy compensated WS–FSAT: electrodes' distribution (a), and corresponding directivity function, $|\mathcal{D}(\boldsymbol{k}_0(\omega), \theta)|$ (b).

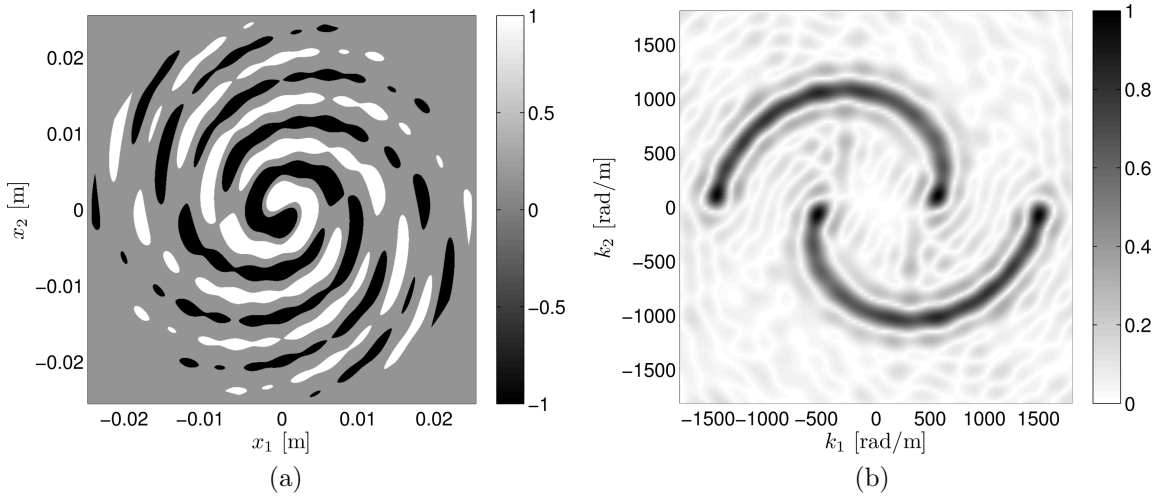

Figure 80: Active material anisotropy not–compensated WS–FSAT: electrodes' distribution (a), and corresponding directivity function, $|\mathcal{D}(\boldsymbol{k}_0(\omega), \theta)|$ (b).

the compensated WS–FSAT design keeps the maximum value of the material and geometric directivities constant regardless the direction, removing the modulating effect of active material anisotropy on the sensing/actuating voltage.

6.4 Conclusions

In this chapter, preliminary testing of WS–FSAT in actuation has been carried. The prototype described in Chapter 5 has been activated by the application of voltage

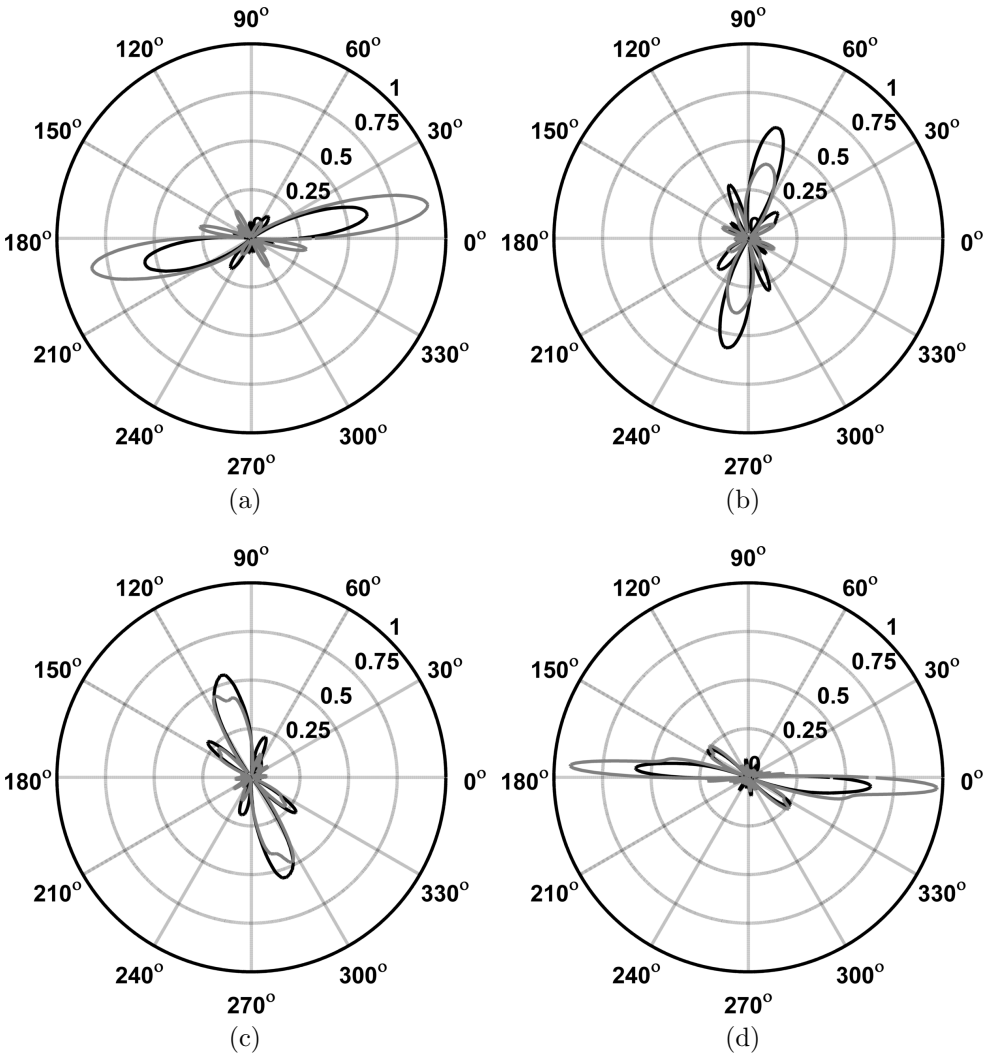

Figure 81: Directivity curves $\mathcal{H}(\theta)\mathcal{D}(\boldsymbol{k}_0(\omega) = k_n(\theta_n), \theta)$: (a) $n = 5$, $\theta_n = 13$ deg; (b) $n = 30$, $\theta_n = 78$ deg; (c) $n = 45$, $\theta_n = 108$ deg; (d) $n = 90$, $\theta_n = 180$ deg. Black lines: anisotropy compensated WS–FSAT. Grey lines: original WS–FSAT.

signals to its electrodes and the wavefields generated have been recorded. For hardware simplicity, only one electrodes' group has been activated, however the expected directionality of the device has been observed successfully. Next, because the PVDF substrate is not ideal for waves generation, an alternative manufacturing process for the realization of the WS–FSAT, featuring an electrodes shaped MFC, has been discussed as a possible improvement of the transducer actuation authority, considering also the influence of the MFC material anisotropy.

CHAPTER VII

CONCLUDING REMARKS AND FUTURE WORK

7.1 Summary

This research studies Frequency Steerable Acoustic Transducers (FSATs) for directional generation/sensing of guided waves. The theoretical analysis of equations governing sensing and generation of Lamb waves through surface mounted piezoelectric transducers provides the design tools to develop transducer shapes which generate interference phenomena resulting in strong frequency-based beam forming capability. In particular, an expression of the transducers directivity has been formulated based on spatial distribution of active material, valid for both wave sensing and actuation, in agreement with acoustic reciprocity principles. The FSATs can be designed to produce directional patterns which vary with the actuation frequency in generation and sense a dominant frequency component depending on direction of an incoming wave in sensing.

The FSAT configurations presented are a quadrilateral array and a geometry whose wavenumber domain representation features maximum amplitudes located along a spiral, named Wavenumber Spiral FSAT (WS–FSAT). The quadrilateral array demonstrates, through numerical analysis and experimental validation, the concept of frequency-dependent directionality. However it suffers from limited directional performance. The WS–FSAT, instead, features a continuous frequency based directivity, and is an excellent candidate for effective Structural Health Monitoring (SHM) applications. Prototyping and successive testing of the WS–FSAT proved its effectiveness in sensing for location of broadband acoustic sources. An imaging technique was adopted for improved post processing of the WS–FSAT output. Finally, the

WS–FSAT was experimentally validated also in generation.

7.2 Contributions

The research presented in this work achieves the following contributions:

1. a novel class of transducers (FSATs) for sensing and generation of guided waves with frequency–based directionality;

2. the WS–FSAT geometry, characterized by an excellent directionality, allowing location detection of broadband acoustic sources and directional scanning;

3. the WS–FSAT manufacturing, based on inkjet printing of the electrode patterns on a polyvinylidene fluoride (PVDF) substrate;

4. the experimental validation of WS–FSAT directional capabilities in both sensing and actuation;

5. the implementation of a working imaging technique to enrich further the sensing capabilities of the WS–FSAT, providing an immediate visualization of the acoustic event.

7.3 Limitations & challenges

Sensing performance of WS–FSAT may be affected by the frequency content of the incoming wave–packet. If it is not broadband and uniformly weighted, the filtering action of the device could be biased and result in the wrong estimation of the direction of arrival. In the acoustic source angular localization experiment (Section 5.3.2), the broadband excitation used for the generation of waves was characterized by the frequency content shown in Fig. 46. Even if the spectrum is not perfectly flat, the filtering action of the PVDF WS–FSAT was strong enough to overcome this. In a perspective of WS–FSAT application for impact detection, a relevant issue is the bandwidth of the induced perturbation by the impact, which traditionally is not so

broadband [65]. The highest excited frequency in impacts is usually also not as high as the frequencies considered in PVDF WS–FSAT testing, which considered values up to 350 kHz. A specific WS–FSAT design for sensing of a realistic impact induced wavefield is required and may involve a narrow WS–FSAT bandwidth spanning a lower frequency range than the one considered in this thesis. This would result in larger WS–FSATs, due to the lower frequency range, i.e. lower wavenumber spiral, with a reduced frequency shift per DOA change, caused by the narrow bandwidth.

The WS–FSAT tuning on A_0 mode is discussed in Section 4.3, for which the device ideally performs a rigorous mode selection and is sensitive to the chosen mode only. Contributions from other modes are mapped to a different frequency range. However, some multimodal interactions might be possible. In practice, in fact, the filtering effect is slightly affected by wavenumber spiral side lobes outside the $[k_m, k_M]$ range, which can introduce spurious modal contributions within the frequency band reserved for the tuned mode. The wavenumber range, from which S_0 interference within the A_0 operating region can arise, is identified in Fig. 82(a) and marked with solid circles in Fig. 82(b). Secondary lobes of the spiral distribution within the highlighted ring are responsible for interfering S_0 terms. Since the amplitude of side lobes is relatively small compared to that of main lobes, these terms do not affect the localization of strong acoustic sources, while they can pose challenges to the detection of weak scatterers [8].

In this work, FSATs have been designed to operate in a frequency range where wave propagation is the superposition of the first anti–symmetric A_0 and symmetric S_0 Lamb wave modes, i.e. for frequencies below the A_1 mode cut–off. Dispersion curves of modes are strictly dependent by the plate thickness and, in particular, as the thickness increases, the cut–off frequencies of modes shift towards lower frequencies (Fig. 83). This might complicate the design of WS–FSAT for applications to thick plates, where may be hard to isolate only one dispersion curve in the operating region

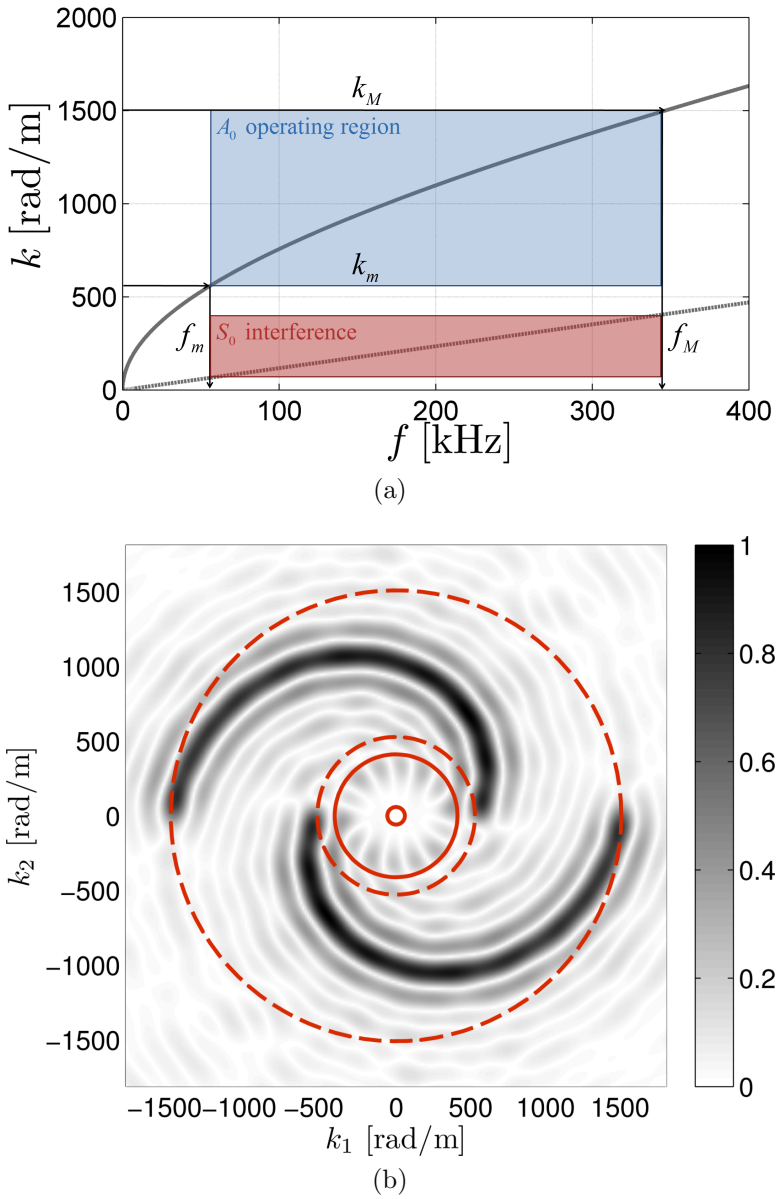

Figure 82: Dispersion characteristics of the A_0 and S_0 modes for a 0.82 mm–thick aluminum plate. The "k range" $[k_m,\ k_M]$ and corresponding frequency bands of directional sensitivity to the A0 mode are highlighted, along with the wavenumber range where secondary lobes of the spiral distribution can give rise to S_0 interference within the A_0 sensor operating region (a); WS–FSAT directivity. Dashed circles represent the wavenumber range $[k_m,\ k_M]$, while solid circles delimit the wavenumber interval sensitive to "S0 interference" phenomena for a 0.82 mm-thick aluminum plate (b).

of the device.

To achieve a good actuation efficacy, it is essential to have a good impedance

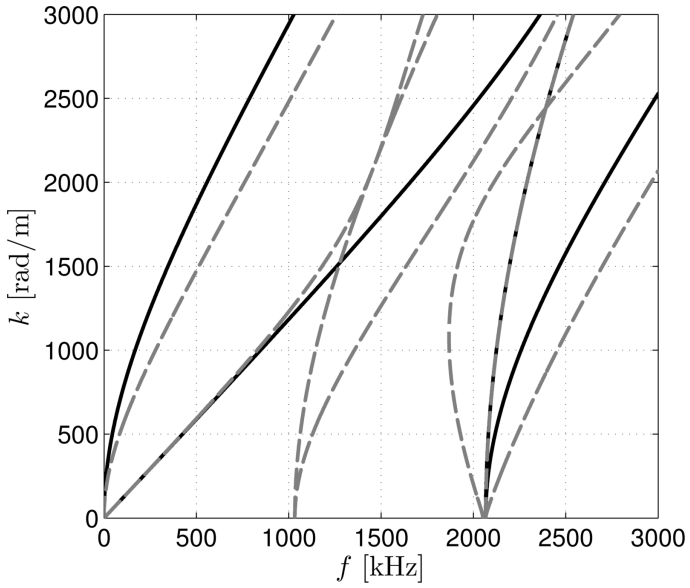

Figure 83: Dispersion curves of Lamb waves in aluminum plates of different thickness, t: solid lines, $t = 0.75$ mm; dashed lines, $t = 1.5$ mm.

matching between the active substrate and the structure. The adoption of PVDF is not an optimal choice. The introduction of a copper matching layer between the PVDF device and the structure could lead to a better coupling with an improved actuation performance [54]. The alternative solution of a WS–FSAT based on MFC substrate, described in Section 6.3, would imply an improvement in the impedance matching due to the high stiffness of the composite fiber phase, but still need to be proven.

7.4 Conclusions & future work

This research has investigated the potential of patterned transducers for directional guided wave generation and sensing. Effective frequency based wave steering has been demonstrated through numerical models and experiments. The quadrilateral array and the WS–FSAT prototypes have attractive features which may be exploited for SHM applications. FSATs may be good candidates for remote sensing and actuation applications because of their hardware simplicity. In the field of aerospace structures, FSATs may be suitable for embedded installations on plate– and shell–like

structures, as wings and fuselages. They may be adopted both in passive mode, for impact detection, and in active mode, for on–demand structural scanning. Also FSAT installations on pipelines may be effective for leaks detection. However, much work is needed towards their practical implementation. In fact, FSAT lab experiments were based on idealized setups, and FSAT performance evaluation on real structures is still required. Considerable work needs to be done to achieve in–service qualification of the FSATs and associated hardware; other important issues to be addressed are discussed as follows.

The thresholding procedure outlined in Section 4.2 was seen as a necessary step to obtain a feasible transducer geometry. This step leads to performance reduction compared with transducers with the analytical spatial distribution, characterized by a grading of the active material. A possible alternative to the thresholding procedure may be the realization of a porous electrode pattern [62, 61] which would mimic the analytical grading for an improved WS–FSAT directivity. As an example, the geometry of a WS–FSAT porous electrode pattern is shown in Fig. 84. Issues that need to be considered with this approach are the thickness of the smallest electrode features, which may be not sufficient to ensure effective conductivity. Also, the inkjet fabrication approach may not have enough resolution for the porous pattern realization.

Considering the source localization experiment of Section 5.4, a significant improvement would be the development of a strategy for time–of–flight (TOF) estimation without requiring knowledge of the instant in which the acoustic event takes place. This would allow a more realistic WS–FSAT application in the context of impact detection and localization.

The actuation capability of the WS–FSAT also requires additional investigation. Its actuation efficacy could most likely be improved with the implementation of the WS–FSAT based on macro fiber composite (MFC) substrate, following the approach suggested in Section 6.3. In this case, an aspect that deserves further consideration

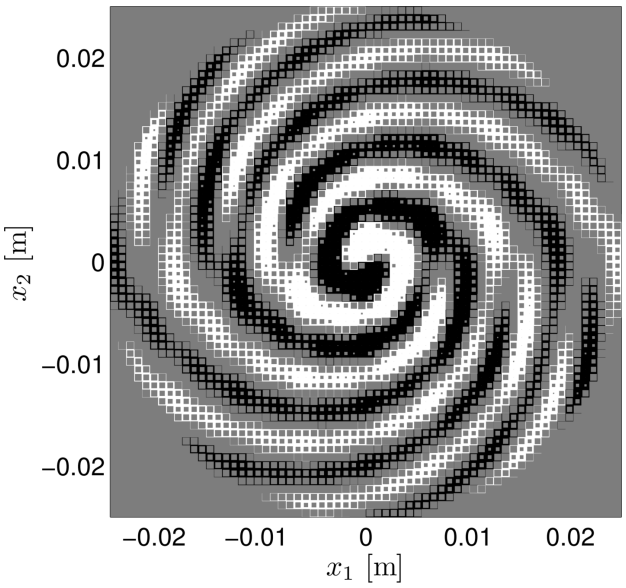

Figure 84: Design of a porous electrodes' pattern for a potential improvement of the WS–FSAT directional capability.

is the behavior of the MFC in d_{31}–mode with shaped electrodes. The homogeneous properties of Table 8, in fact, are computed for the continuous electrode case and the substrate action with shaped electrodes needs to be verified.

The WS–FSAT performance for localization of scatterers needs to be evaluated for a more precise qualification as a potential device for active SHM applications. Two possible schemes of operation are available to perform this task: pulse–echo and pitch–catch. In the former, the WS–FSAT acts both as an actuator and sensor at the same time. In the pitch–catch approach, a pulse signal is sent across the specimen under interrogation and the WS–FSAT receives the signal. From various characteristics of the received signal, such as delay in time of transit, amplitude, frequency content, etc., information about the damage can be obtained. For this last approach, some work has already been done in [8], where issues related to S_0 mode interference emerged.

Due to the increasing prominence of composite materials in aerospace structures, the application of FSATs to composite laminates needs to be analyzed to consolidate

the attractiveness of the wave frequency steerability concept in GW SHM. In this case, major issues are represented by material anisotropy and high wave attenuation. The effect of anisotropy is analyzed in Section 3.7 with the quadrilateral array tuning on the A_0 mode in a glass fiber laminate. Wave attenuation is potentially the biggest issue because it could significantly reduce the area on which the FSATs would be effective.

It may be worth studying phased operations of two WS–FSATs, trying to achieve side lobes suppression and single beam activation, allowing real 360 deg directional scan, without the ± 180 deg uncertainty. Formulating a topology optimization problem of the WS–FSAT design for a reduction of side lobes and a beamwidth improvement are also interesting further developments.

REFERENCES

[1] Achenbach, J. D., *Acoustic Fields and Waves in Solids*. North Holland, 1984.

[2] Ahmad, R., Kundu, T., and Placko, D., "Modeling of phased array transducers," *The Journal of the Acoustical Society of America*, vol. 117, no. 4, pp. 1762–1776, 2005.

[3] Alers, G., "Emat designs for special applications," *Materials Evaluation*, vol. 45, no. 10, pp. 1184–118, 1987.

[4] Alleyne, D. and Cawley, P., "Optimization of lamb wave inspection techniques," *NDTE International*, vol. 25, no. 1, pp. 11–22, 1992.

[5] Alleyne, D. and Cawley, P., "The interaction of lamb waves with defects," *IEEE transactions on ultrasonics, ferroelectrics, and frequency control*, vol. 39, pp. 381–397, 1992.

[6] Auld, B. A., *Acoustic Fields and Waves in Solids*. Krieger, 1990.

[7] Baravelli, E., De Marchi, L., Speciale, N., and Ruzzene, M., "Bimodal warped frequency transform (bwft) for guided wave mode conversion characterization," in *Proceedings of SPIE*, vol. 8348, p. 834803, 2012.

[8] Baravelli, E., Senesi, M., Gottfried, D., De Marchi, L., and Ruzzene, M., "Inkjet fabrication of spiral frequency-steerable acoustic transducers (fsats)," in *Proceedings of SPIE*, vol. 8348, p. 834817, 2012.

[9] Bartoli, I., Marzani, A., di Scalea, F. L., and Viola, E., "Modeling wave propagation in damped waveguides of arbitrary cross-section," *Journal of Sound and Vibration*, vol. 295, no. 3-5, pp. 685–707, 2006.

[10] Bartoli, I., Marzani, A., di Scalea, F. L., and Viola, E., "Modeling wave propagation in damped waveguides of arbitrary cross-section," *Journal of Sound and Vibration*, vol. 295, no. 35, pp. 685 – 707, 2006.

[11] Biscani, F., Nasser, H., Belouettar, S., and Carrera, E., "Equivalent electro-elastic properties of macro fiber composite (mfc) transducers using asymptotic expansion approach," *Composites Part B: Engineering*, vol. 42, no. 3, pp. 444–455, 2011.

[12] Chiu, W., "Damage detection in bonded repairs using piezoceramics," *Smart Materials and Structures*, vol. 9, no. 4, pp. 466–475, 2000.

[13] Chung, S., Li, M., Kanamaluru, S., and Chang, K., "Meander-image-line-feed microstrip antenna array for frequency-swept beam steering," in *Antennas and Propagation Society International Symposium, 1996. AP-S. Digest*, vol. 2, pp. 1254–1257, IEEE, 1996.

[14] Collet, M., Ruzzene, M., and Cunefare, K., "Generation of lamb waves through surface mounted macro-fiber composite transducers," *Smart Materials and Structures*, vol. 20, p. 025020, 2011.

[15] Croxford, A., Wilcox, P., Drinkwater, B., and Konstantinidis, G., "Strategies for guided-wave structural health monitoring," *Proceedings of the Royal Society A*, vol. 463, no. 2087, pp. 2961–2981, 2007.

[16] Dalton, R., Cawley, P., and Lowe, M., "The potential of guided waves for monitoring large areas of metallic structures," *Journal of Nondestructive Evaluation*, vol. 20, pp. 29–46, 2001.

[17] De Marchi, L., Marzani, A., Caporale, S., and Speciale, N., "Ultrasonic guided-waves characterization with warped frequency transforms," *IEEE Transactions on Ultrasonics, Ferroelectrics, and Frequency Control*, vol. 56, no. 10, pp. 2232–2240, 2009.

[18] Degertekin, F. L., "Single mode lamb wave excitation in thin plates by hertzian contacts," *Applied Physics Letters*, vol. 69, no. 2, pp. 146–148, 1996.

[19] Deraemaeker, A. and Nasser, H., "Numerical evaluation of the equivalent properties of macro fiber composite (mfc) transducers using periodic homogenization," *International Journal of Solids and Structures*, vol. 47, no. 24, pp. 3272–3285, 2010.

[20] Deutsch, W., Deutsch, K., Cheng, A., and Achenbach, J., "Defect detection with rayleigh and lamb waves generated by a self-focusing phased array," *NDT.net*, vol. 3, no. 12, pp. 1–6, 1998.

[21] Dougherty, R. P., "Spiral-shaped array for broadband imaging," *US Patent*, no. 5,838,284, 1998.

[22] Ellerbrock, P. J., "Dc-xa structural health-monitoring fiber optic-based strain measurement system," *Proceedings of SPIE - the International Society for Optical Engineering*, vol. 3044, no. PAGE, pp. 207–218, 1997.

[23] Fromme, P., Wilcox, P. D., Lowe, M., and Cawley, P., "A guided ultrasonic waves array for structural integrity monitoring," *AIP Conference Proceedings*, vol. 760, no. 1, pp. 1780–1787, 2005.

[24] Giurgiutiu, V., *Structural health monitoring with piezoelectric wafer active sensors*. Academic Press, 2007.

[25] Giurgiutiu, V. and Bao, J., "Embedded-ultrasonics structural radar for nondestructive evaluation of thin-wall structures," in *2002 ASME International Mechanical Engineering Congress*, (New Orleans, LA, USA), November 2002.

[26] Giurgiutiu, V., Bao, J., and Zagrai, A., "Structural health monitoring system utilizing guided lamb waves embedded ultrasonic structural radar," *US Patent*, no. 6,996,480, 2006.

[27] Graff, K. F., *Wave Motion in Elastic Solids*. Dover, 1975.

[28] Hagood, N. and Bent, A., "Development of piezoelectric fiber composites for structural actuation," in *AIAA/ASME/ASCE/AHS/ASC 34th Structures, Structural Dynamics, and Materials Conference*, vol. 1, pp. 3625–3638, 1993.

[29] Hall, J. and Michaels, J., "Minimum variance ultrasonic imaging applied to an in situ sparse guided wave array," *Ultrasonics, Ferroelectrics and Frequency Control, IEEE Transactions on*, vol. 57, no. 10, pp. 2311–2323, 2010.

[30] Hall, S., Hall, G., and J.A., M., *High-Speed Digital System Design: A Handbook of Interconnect Theory and Design Practices*. Wiley-IEEE Press, 2000.

[31] Holland, M. G. and Claiborne, L. T., "Practical surface acoustic wave devices," *Proceedings of the IEEE*, vol. 62, pp. 582–611, 1974.

[32] Ihn, J. and Chang, F., "Pitch-catch active sensing methods in structural health monitoring for aircraft structures," *Structural Health Monitoring*, vol. 7, pp. 5–19, 2008.

[33] Kaiser, J., "The archimedean two-wire spiral antenna," *Antennas and Propagation, IRE Transactions on*, vol. 8, no. 3, pp. 312–323, 1960.

[34] Kehlenbach, M., "Identifying damage in plates by analyzing lamb wave propagation characteristics," *Proceedings of SPIE - the International Society for Optical Engineering*, vol. 4702, no. PAGE, pp. 364–375, 2002.

[35] Keilers, C., "Identifying delamination in composite beams using built-in piezoelectrics .1. experiments and analysis," *Journal of Intelligent Material Systems and Structures*, vol. 6, no. 5, pp. 649–663, 1995.

[36] Kessler, S. S., "Design of a piezoelectric-based structural health monitoring system for damage detection in composite materials," *Proceedings of SPIE - the International Society for Optical Engineering*, vol. 4701, no. PAGE, pp. 86–96, 2002.

[37] Kim, D. and Philen, M., "On the beamsteering characteristics of mfc phased arrays for structural health monitoring," in *49th AIAA/ASME/ASCE/AHS/ASC Structures, Structural Dynamics, and Materials Conference*, (Schaumburg, IL, USA), April 2007.

[38] Kino, G., Corl, D., Bennett, S., and K., P., "Real time synthetic aperature imaging system," *Ultrasonics Symposium, IEEE CNF*, pp. 722–731, 1980.

[39] Kollar, L., "Calculation of the stresses and strains in embedded fiber optic sensors," *Journal of Composite Materials*, vol. 32, no. 18, pp. 1647–1679, 1998.

[40] Koosha, A. and Sunthankar, Y., "A novel directional ultrasonic radiator," in *Ultrasonics Symposium, 1989. Proceedings., IEEE 1989*, pp. 785–788, IEEE, 1989.

[41] Krautkramer, J., Krautkramer, H., and Hislop, J., *Ultrasonic Testing of Materials*. Springer-Verlag, 1990.

[42] Lanza di Scalea, F., Matt, H., and Bartoli, I., "The response of rectangular piezoelectric sensors to rayleigh and lamb ultrasonic waves," *J. Acoust. Soc. Am.*, vol. 121, pp. 175–187, 2007.

[43] Laude, V., Gerard, D., Khelfaoui, N., Jerez-Hanckes, J., and Khelif, A., "Subwavelength focusing of surface acoustic waves generated by an annular interdigital transducer," *Applied Physics Letters*, vol. 92, no. 904104, 2008.

[44] Li, J. and Rose, J., "Implementing guided wave mode control by use of a phased transducer array," *IEEE Transactions on Ultrasonics, Ferroelectrics, and Frequency Control*, vol. 48, no. 3, pp. 761–768, 2001.

[45] Marantidis, C., "Acoustic-emission sensing in an on-board smart structural health monitoring-system for military aircraft," *Smart Sensing, Processing, and Instrumentation*, vol. 2191, pp. 258–264, 1994.

[46] Matt, H. M. and Lanza di Scalea, F., "Macro-fiber composite piezoelectric rosettes for acoustic source location in complex structures," *Smart Mater. Struct.*, vol. 16, p. 1489, 2007.

[47] McNab, A. and Campbell, M. J., "Ultrasonic phased arrays for nondestructive testing," *NDT International*, vol. 20, pp. 333–337, 2007.

[48] Michaels, J., "Detection, localization and characterization of damage in plates with an *in situ* array of spatially distribuited ultrasonic sensors," *Smart Materials and Structures*, vol. 17,035035 (15pp), 2008.

[49] Michaels, J., Croxford, A., and Wilcox, P., "Imaging algorithms for locating damage via *in situ* ultrasonic sensors," *IEEE Sensors Applications Symposium*, pp. 63–67, 2008.

[50] Michaels, J., Hall, J., and Michaels, T., "Adaptive imaging of damage from changes in guided wave signals recorded from spatially distributed arrays," *Health Monitoring of Structural and Biological Systems 2009, edited by Tribikram Kundu, Proc. of SPIE*, vol. 7295, no. 729515, pp. 1–15, 2009.

[51] Monkhouse, R. S. C., Wilcox, P., and Cawley, P., "Flexible interdigitated pvdf transducers for the generation of lamb waves in structures," *Ultrasonics*, vol. 35, pp. 489–498, 1997.

[52] Monkhouse, R., "Flexible interdigital pvdf transducers for the generation of lamb waves in structures," *Ultrasonics*, vol. 35, no. 7, pp. 489–498, 1997.

[53] Monkhouse, R., "Rapid monitoring of structures using interdigital lamb wave transducers," *Smart Materials and Structures*, vol. 9, no. 3, pp. 304–309, 2000.

[54] Monkhouse, R., Wilcox, P., and Cawley, P., "Flexible interdigital pvdf transducers for the generation of lamb waves in structures," *Ultrasonics*, vol. 35, no. 7, pp. 489–498, 1997.

[55] Mukdadi, O. M., Desai, Y. M., Datta, S. K., Shah, A. H., and Niklasson, A. J., "Elastic guided waves in a layered plate with rectangular cross section," *The Journal of the Acoustical Society of America*, vol. 112, no. 5, pp. 1766–1779, 2002.

[56] Oppenheim, A., Schafer, R., Buck, J., and others, *Discrete-time signal processing*, vol. 2. Prentice–Hall, 1989.

[57] Osmont, D., "Health monitoring of sandwich plates based on the analysis of the interaction of lamb waves with damages," *Proceedings of SPIE - the International Society for Optical Engineering*, vol. 4327, no. PAGE, pp. 290–301, 2001.

[58] Paradies, R. and Schläpfer, B., "Finite element modeling of piezoelectric elements with complex electrode configuration," *Smart Material Structures*, vol. 18, no. 2, p. 025015, 2009.

[59] Pelts, S., "comb transducer for guided wave generation and mode selection," 1996.

[60] Pierce, S., "Laser generation of ultrasonic lamb waves using low power optical sources," *Iee Proceedings-science Measurement and Technology*, vol. 145, no. 5, pp. 244–249, 1998.

[61] Preumont, A., Francois, A., De Man, P., Loix, N., and Henrioulle, K., "Distributed sensors with piezoelectric films in design of spatial filters for structural control," *Journal of sound and vibration*, vol. 282, no. 3, pp. 701–712, 2005.

[62] Preumont, A., Francois, A., De Man, P., and Piefort, V., "Spatial filters in structural control," *Journal of sound and vibration*, vol. 265, no. 1, pp. 61–79, 2003.

[63] Raghavan, A. and Cesnik, C., "Finite-dimensional piezoelectric transducer modeling for guided wave based structural health monitoring," *Smart materials and structures*, vol. 14, pp. 1448–1461, 2005.

[64] Rees, D., "Numerical study of crack monitoring in patched structures using a piezoelectric sensor," *Smart Materials and Structures*, vol. 1, no. 3, pp. 202–, 1992.

[65] Ribay, G., Catheline, S., Clorennec, D., Kiri Ing, R., Quieffin, N., and Fink, M., "Acoustic impact localization in plates: Properties and stability to temperature variation," *Ultrasonics, Ferroelectrics and Frequency Control, IEEE Transactions on*, vol. 54, no. 2, pp. 378–385, 2007.

[66] Roh, Y., Varadan, V., and Varadan, V., "Characterization of all the elastic, dielectric, and piezoelectric constants of uniaxially oriented poled pvdf films," *Ultrasonics, Ferroelectrics and Frequency Control, IEEE Transactions on*, vol. 49, no. 6, pp. 836–847, 2002.

[67] Romanoni, M., Apetre, N., Ruzzene, M., and Gonella, S., "Two-dimensional periodic actuators for frequency-based beam steering," *Health Monitoring of Structural and Biological Systems 2009, edited by Tribikram Kundu, Proc. of SPIE*, vol. 7295, no. 729526, pp. 1–11.

[68] Rose, J. L., *Ultrasonic Waves in Solid Media*. Cambridge University press, 1999.

[69] Rose, J., "A baseline and vision of ultrasonic guided wave inspection potential," *Journal of Pressure Vessel Technology*, vol. 124, no. 1, pp. 273–282, 2002.

[70] Rose, J., Ditri, J., Pilarski, A., Rajana, K., and Carr, F., "A guided wave inspection technique for nuclear steam generator tubing," *NDT&E International*, vol. 27, no. 6, pp. 307 – 310, 1994.

[71] Rose, J. L., "vision of ultrasonic guided wave inspection potential," *American Society of Mechanical Engineers (Publication) NDE*, vol. 20, pp. 1–22, 2001.

[72] Salas, K. and Cesnik, C., "Guided wave excitation by a clover transducer for structural health monitoring: theory and experiments," *Smart Materials and Structures*, vol. 18,075005 (27pp), 2009.

[73] Shoykhetbrod, A., Nusler, D., and Hommes, A., "Design of a siw meander antenna for 60 ghz applications," in *Microwave Conference (GeMiC), 2012 The 7th German*, pp. 1–3, IEEE, 2012.

[74] Sumanaweera, T., Schwartz, J., and Napolitano, D., "A spiral 2d phased array for 3d imaging," in *Ultrasonics Symposium, 1999. Proceedings. 1999 IEEE*, vol. 2, pp. 1271–1274 vol.2, 1999.

[75] Valdes, S., "Health monitoring of composites using lamb waves generated by piezoelectric devices," *Plastics Rubber and Composites*, vol. 29, no. 9, pp. 475–481, 2000.

[76] Van Trees, H. L., *Optimum Array Processing*. John Wiley & Sons, Inc., 2002.

[77] Wang, C., Rose, J., and Chang, F.-K., "A synthetic time-reversal imaging method for structural health monitoring," *Smart materials and structures*, vol. 13, pp. 415–423, 2004.

[78] Weisstein, E. W., "Archimedean spiral," 2010.

[79] Weyman, A. E., *Principles and Practice of Echocardiography.* Lea & Febiger, 1994.

[80] Wilcox, P., Lowe, M., and Cawley, P., "Omni-directional guided wave transducer arrays for the rapid inspection of large areas of plate structures," *IEEE Transactions on Ultrasonics, Ferroelectrics, and Frequency Control*, vol. 50, no. 6, pp. 699–709, 2003.

[81] Wilcox, P., "Acoustic fields from pvdf interdigital transducers," *IEE Proceedings: Science, Measurement and Technology*, vol. 145, no. 5, pp. 250–259, 1998.

[82] Wilcox, P., "Mode and transducer selection for long range lamb wave inspection," 2001.

[83] Wilcox, P., "A rapid signal processing technique to remove the effect of dispersion from guided wave signals," *Ultrasonics, Ferroelectrics and Frequency Control, IEEE Transactions on*, vol. 50, no. 4, pp. 419–427, 2003.

[84] Wilkie, W., Bryant, R., High, J., Fox, R., Hellbaum, R., Jalink Jr, A., Little, B., and Mirick, P., "Low-cost piezocomposite actuator for structural control applications," in *Proceedings of SPIE*, vol. 3991, p. 323, 2000.

[85] Williams, R., Park, G., Inman, D., and Wilkie, W., "An overview of composite actuators with piezoceramic fibers," *Proceeding of IMAC XX*, pp. 4–7, 2002.

[86] Wooh, S.-C. and Shi, Y., "Influence of phased array element size on beam steering behavior," *Ultrasonics*, vol. 36, no. 6, pp. 737 – 749, 1998.

[87] Worden, K., "Experimental validation of a structural health monitoring methodology," *Journal of Sound & Vibration*, vol. 259, no. 2, pp. 323–343, 2003.

[88] Yatsuda, Y., "Design techniques for saw filters using slanted finger interdigital transducers," *IEEE Transactions On Ultrasonics, Ferroelectrics, And Frequency Control*, vol. 44, no. 2, pp. 453–459, 1997.

[89] Yoo, B., "Piezoelectric-paint-based two-dimensional phased sensor arrays for structural health monitoring of thin panels," *Smart Materials and Structures*, vol. 19, no. 7, p. 075017 (17pp), 2010.

[90] Yu, L. and Giurgiutiu, V., "In-situ optimized pwas phased arrays for lamb wave structural health monitoring," *Health Monitoring of Structural and Biological Systems 2009, edited by Tribikram Kundu, Proc. of SPIE*, vol. 2, no. 3, pp. 459–487, 2007.

[91] Yu, L. and Giurgiutiu, V., "In situ 2-d piezoelectric wafer active sensors arrays for guided wave damage detection," *Ultrasonics, Elsevier Press*, vol. 48, no. 2, pp. 117–134, 2008.

[92] Zhu, W., "Ultrasonic guided wave ndt for hidden corrosion detection," *Research in Nondestructive Evaluation*, vol. 10, no. 4, pp. 205–225, 1998.